

Aus dem Laser-Forschungslabor der Laser-Immunologie-Forschungs-Einrichtung
(LIFE-Zentrum) der Ludwig-Maximilians-Universität München

Bereichsleitung: PD Dr. rer. biol. hum. Ronald Sroka

Geschäftsführung: Prof. Dr. med. Christian Stief



OPTISCHE TUMOR- UND BLUTGEFÄßDETEKTION ZUR
ERHÖHUNG VON PRÄZISION UND SICHERHEIT BEI DER
STEREOTAKTISCHEN BIOPSIE VON HIRNTUMOREN

Dissertation

zum Erwerb des Doktorgrades der Humanbiologie
an der Medizinischen Fakultät der
Ludwig-Maximilians-Universität München

vorgelegt von
Niklas Markwardt
aus München
2018

Mit Genehmigung der Medizinischen Fakultät
der Universität München

Berichterstatter: PD Dr. rer.biol.hum. Ronald Sroka

Mitberichterstatter: Prof. Dr. Olaf Dietrich
Prof. Dr. Friedrich-Wilhelm Kreth

Mitbetreuung durch den
promovierten Mitarbeiter: Dr. rer. biol. hum. Herbert Stepp

Dekan: Prof. Dr. med. dent. Reinhard Hickel

Tag der mündlichen Prüfung: 27.02.2018

für meine Eltern

INHALTSVERZEICHNIS

Publikationsliste	7
Abstract	9
Zusammenfassung	11
1 Einleitung	13
1.1 Medizinisch-biologischer Hintergrund	13
1.1.1 Klinisches Hauptanwendungsgebiet: maligne Gliome	13
1.1.2 Stereotaktische Biopsie	13
1.1.3 Tumormarkierung mittels 5-Aminolävulinsäure-induzierter Protoporphyrin-IX-Fluoreszenz ...	14
1.2 Problemstellung	16
1.2.1 Erhöhung der diagnostischen Aussagekraft des Biopsats	16
1.2.2 Vermeidung von intrakraniellen Blutungen	16
1.3 Opto-mechanische Biopsienadel mit integrierter Tumor- und Blutgefäßerkennung	17
1.3.1 Mechanische Biopsienadel	17
1.3.2 Tumordetektion mittels Protoporphyrin-IX-Fluoreszenz	17
1.3.3 Blutgefäßdetektion mittels Remissionsspektrometrie	19
1.3.4 Blutgefäßdetektion mittels Indocyaningrün-Fluoreszenz	20
1.3.5 Modell einer faserbasierten opto-mechanischen Biopsienadel	22
2 Originalmanuskripte	23
405 nm versus 633 nm for protoporphyrin IX excitation in fluorescence-guided stereotactic biopsy of brain tumors	25
Remission spectrometry for blood vessel detection during stereotactic biopsy of brain tumors	47
Literaturverzeichnis	65
Danksagung	69
Lebenslauf	71
Eidesstattliche Versicherung	72

PUBLIKATIONSLISTE

Veröffentlichungen in begutachteten Fachmagazinen:

- Niklas A. Markwardt, Neda Haj-Hosseini, Bastian Hollnburger, Herbert Stepp, Petr Zelenkov und Adrian Rühm, *405 nm versus 633 nm for protoporphyrin IX excitation in fluorescence-guided stereotactic biopsy of brain tumors*, J. Biophotonics 9(9), 901–912 (2016), JIF (2014): 4,447
- Niklas A. Markwardt, Herbert Stepp, Gerhard Franz, Ronald Sroka, Marcus Goetz, Petr Zelenkov und Adrian Rühm, *Remission spectrometry for blood vessel detection during stereotactic biopsy of brain tumors*, J. Biophotonics 1–15 (2016) / doi: 10.1002/jbio.201600193, JIF (2015): 3,818
- Adrian Rühm, Niklas A. Markwardt, Nikolas Dominik, Christoph Polzer, Ronald Sroka und Herbert Stepp, *Indocyanine green fluorescence detection with a two-fiber probe for blood vessel recognition during stereotactic neurosurgery*, prepared for submission to J. Biophotonics, JIF (2015): 3,818
- Niklas A. Markwardt, Maurice Hermwille, Peter Schaur, Laura Bienert, Frank Strittmatter und Ronald Sroka, *Laser safety aspects in Ho:YAG-laser assisted lithotripsy*, prepared for submission to World Journal of Urology, JIF (2015): 2,397

Veröffentlichungen in Conference Proceedings:

- Markwardt, N. et al., *Optical spectroscopy for stereotactic biopsy of brain tumors*, in Medical Laser Applications and Laser-Tissue Interactions VII, L. Lilge and R. Sroka, eds., Vol. 9542 of SPIE Proceedings (Optical Society of America, 2015), paper 954208
- Markwardt, N. et al., *Detection limits of 405 nm and 633 nm excited PpIX fluorescence for brain tumor detection during stereotactic biopsy*, Proc. SPIE 9887, Biophotonics: Photonic Solutions for Better Health Care V, 98872Z (April 27, 2016), doi:10.1117/12.2225234

weitere Konferenzbeiträge:

- Posterpräsentation *Optical spectroscopy for stereotactic biopsy of brain tumors* auf dem internationalen Symposium ‘Photodynamic Therapy and Photodiagnosis in Clinical Practice’, Brixen/Bressanone, 2014
- mündlicher Vortrag *Optical spectroscopy for stereotactic biopsy of brain tumors* auf der Konferenz ‘Medical Laser Applications and Laser-Tissue Interactions VII’, ECBO, München, 2015
- Posterpräsentation *Detection limits of 405 nm and 633 nm excited PpIX fluorescence for brain tumor detection during stereotactic biopsy* auf der Konferenz ‘Medical Laser Applications and Laser-Tissue Interactions VII’, Photonics Europe, Brüssel, 2016
- Posterpräsentation *Optical spectroscopy for stereotactic biopsy of brain tumors* auf dem internationalen Symposium ‘Photodynamic Therapy and Photodiagnosis update’, Nancy, 2016

Erfindungsmeldungen:

- Markwardt, N. und Stepp, H., *Gerät und Verfahren zur verbesserten fluoreszenzgestützten Darstellung von Gewebestrukturen*, 2015, Aktenzeichen VIII.3/29/15, Erfindung freigegeben
- Markwardt, N., Stepp, H. und Rühm, A., *Gerät und Verfahren zur Erkennung von Blutgefäßen während einer stereotaktischen Hirnbiopsie*, 2016, Aktenzeichen VIII.3/384.3.2.1, Inanspruchnahme der Erfindungsmeldung wird noch geprüft

Gebrauchsmuster:

Markwardt, N., Stepp, H. und Rühm, A., *Vorrichtung zur Erkennung von Blutgefäßen mittels Remissionspektrometrie*, 2016, eingetragen beim Deutschen Patent- und Markenamt

ABSTRACT

Malignant gliomas constitute the largest group of primary malignant brain tumors. They arise from glial cells and infiltrate the surrounding normal brain diffusely, which impedes appropriate treatment to a high extent. Hence, the survival prognosis is extremely poor. In the case of glioblastoma, the most frequent and at the same time most malignant representative of gliomas, it is only about half a year to one and a half years depending on the age of the patient. Especially in non-operable tumors, a stereotactic biopsy is often performed to support and differentiate the diagnosis, which makes individual and thus more promising therapies possible. A system consisting of two cannulae (the so-called biopsy needle) placed one inside the other and rotatable relative to each other is introduced into the brain as deep as the presumed position of the tumor. By sucking tissue into an opened tissue window located on the side of the needle and then twisting the inner versus the outer cannula, a tissue sample is taken which can subsequently be examined by histopathology.

Stereotactic biopsy poses non-negligible risks. One serious problem is a possible mis-positioning of the biopsy needle, which can lead to an unclear or even erroneous diagnosis. Reasons for this may include inaccuracies in preoperative imaging or an undesirable brain shift during the insertion of the biopsy needle. To address this problem, fiber-based fluorescence detection is proposed, aiming at 5-aminolevulinic-acid-induced protoporphyrin IX (PpIX), which selectively accumulates in the tumor cells. The respective advantages and disadvantages of two different PpIX excitation wavelengths were quantitatively investigated using phantom experiments and Monte Carlo simulations [1]. It was shown that excitation in the violet spectral range provides for a 50-fold higher sensitivity than excitation in the red spectral range. However, the sensitivity of the red excitation is sufficient to detect physiological PpIX concentrations of several hundreds of nM to a few μM as found in most malignant gliomas. Blood-covered tumor tissue, in turn, can only be reliably discovered with red excitation since violet light is already completely absorbed by thin blood layers of about 50 μm .

Another potential hazard associated with stereotactic biopsy is the induction of intracranial hemorrhage via injury to a major blood vessel. The associated risk is highest during the actual step of tissue sampling when the two cannulae are twisted against each other. To minimize this risk, a spectrometric diffuse optical tomography method based on the characteristic absorption of the blood dye hemoglobin was developed for the detection of blood vessels within the tissue window that exhibit a diameter above 100 μm [2]. Herein, one side-view fiber illuminates the tissue to be examined with broadband light while a second side-view fiber positioned at a certain distance (about 2 mm) from the first fiber detects the light remitted by the tissue. In order to avoid blood vessel injuries also during the advance of the biopsy needle (with closed tissue window), a method was developed in which blood vessels ahead of the needle are detected by means of two front-view fibers; this method is based on the fluorescence of the intravenously administered fluorophore indocyanine green (ICG) [3]. The method is largely independent of local variations in optical tissue parameters and of the intraluminal ICG concentration. Due to the excitation and emission maxima of ICG, both being in the near-infrared spectral range (around 800 nm), a relatively large detection distance of up to 1.1 mm ahead of the needle can be achieved. Altogether, the two blood vessel recognition methods and the PpIX-assisted tumor detection can be combined by incorporating four glass fibers into the mechanical biopsy needle.

ZUSAMMENFASSUNG

Maligne Gliome stellen die größte Gruppe primärer bösartiger Hirntumoren dar. Sie entstehen aus Zellen des Gliagewebes und infiltrieren umliegendes gesundes Gewebe diffus, was ihre Therapie deutlich erschwert. Daher ist die Überlebensprognose der betroffenen Patienten äußerst schlecht. Sie beträgt beim Glioblastom, dem häufigsten und zugleich bösartigsten Vertreter dieser Art von Tumoren, je nach Alter des Patienten nur etwa ein halbes bis eineinhalb Jahre. Zur Sicherung und Differenzierung der Diagnose, welche eine individuelle und damit erfolgversprechendere Therapie ermöglicht, wird häufig – insbesondere bei nicht operablen Tumoren – eine stereotaktische Biopsie durchgeführt. Dabei wird ein System aus zwei ineinander platzierten und koaxial gegeneinander rotierbaren Kanülen (die sogenannte Biopsienadel) bis zur berechneten Position des Tumors ins Gehirn eingeführt. Durch Ansaugen von Gewebe in ein an der Seite der Nadel befindliches geöffnetes Gewebefenster und darauffolgendes Drehen der inneren gegenüber der äußeren Kanüle wird Gewebe abgeschert und auf diese Weise eine Gewebeprobe entnommen, die anschließend mit histopathologischen Methoden untersucht werden kann.

Die stereotaktische Biopsie birgt nicht zu vernachlässigende Risiken. Ein gravierendes Problem stellt eine mögliche Fehlpositionierung der Biopsienadel dar, die zu einer unklaren oder sogar fehlerhaften Diagnose führen kann. Mögliche Gründe hierfür sind beispielsweise Ungenauigkeiten in der präoperativen Bildgebung oder ein unerwünschter brain shift während des Einführens der Biopsienadel. Um diesem Problem Rechnung zu tragen, wird hier eine faserbasierte Fluoreszenzdetektion von 5-Aminolävulinsäure-induziertem Protoporphyrin IX (PpIX) vorgeschlagen, welches sich selektiv in den Tumorzellen anreichert. Mithilfe von Phantomexperimenten und Monte-Carlo-Simulationen wurden die jeweiligen Vor- und Nachteile zweier hierfür in Frage kommender PpIX-Anregungswellenlängen unter realitätsnahen Bedingungen quantitativ untersucht [1]. Es zeigte sich, dass eine Anregung im violetten Spektralbereich zwar für eine 50-fach höhere Sensitivität sorgt, physiologische PpIX-Konzentrationen von mehreren Hundert nM bis zu einigen μM , wie sie in den meisten malignen Gliomen zu finden sind, jedoch auch mit einer Anregung im roten Spektralbereich gut zu detektieren sind. Blutbedecktes Tumorgewebe wiederum kann nur mit roter Anregung verlässlich erkannt werden, da violettes Licht bereits durch dünne Blutschichten von etwa 50 μm komplett absorbiert wird und dahinterliegendes Gewebe somit nicht zur Fluoreszenz angeregt werden kann.

Ein weiteres Risiko der stereotaktischen Biopsie ist die Auslösung einer intrakraniellen Blutung durch Verletzung eines größeren Blutgefäßes. Die größte Gefahr hierfür besteht im Moment des Gewebeabscherens, wenn die beiden Kanülen gegeneinander verdreht werden. Um das Blutungsrisiko zu verringern, wurde eine spektrometrische Methode zur Erkennung von Blutgefäßen entwickelt, die auf der charakteristischen Absorption des Blutfarbstoffs Hämoglobin beruht [2]. Das Ziel dieser Methode ist die Erkennung von Blutgefäßen innerhalb des Gewebefensters ab einem Durchmesser von 100 μm . Dabei beleuchtet eine Seitblickfaser das zu untersuchende Gewebe mit spektral breitbandigem Licht, während eine zweite Seitblickfaser in einem definierten Abstand von der ersten Faser (etwa 2 mm) das vom Gewebe remittierte Licht detektiert. Um auch eine Blutgefäßverletzung während des Vorschubs der Biopsienadel (bei geschlossenem Gewebefenster) vermeiden zu können, wurde ein Verfahren entwickelt, bei dem Blutgefäße vor der Biopsienadel mithilfe einer Zwei-Faser-Sonde anhand der Fluoreszenz des intravenös verabreichten Fluorophors Indocyaningrün (ICG) erkannt werden [3]. Die beiden Fasern sind dabei in Vorwärtsrichtung, also in Richtung des Vorschubs der Nadel, ausgerichtet. Das Verfahren ist weitgehend unabhängig von lokalen Schwankungen der optischen Gewebeparameter sowie der intraluminalen ICG-Konzentration; aufgrund der im nahinfraroten Spektralbereich (um 800 nm) liegenden Anregungs- und Emissionsmaxima lassen sich relativ große Detektionsreichweiten von bis zu 1,1 mm erreichen. Insgesamt können durch den Einbau von vier Glasfasern in die mechanische Biopsienadel die beiden Blutgefäßerkennungsmethoden sowie die PpIX-gestützte Tumordetektion miteinander kombiniert werden.

1 EINLEITUNG

Bei der vorliegenden Arbeit handelt es sich um eine kumulative Dissertation aus zwei veröffentlichten Originalmanuskripten [1, 2]. Zusätzlich wird explizit auf ein für die Veröffentlichung vorbereitetes Manuskript [3] Bezug genommen. Die drei Manuskripte beinhalten Untersuchungen optischer Methoden zur Erhöhung der Präzision [1] und der Sicherheit [2, 3] der stereotaktischen Hirntumorbiopsie. Die Präzision des Biopsieverfahrens kann durch eine selektive Markierung des Tumorgewebes mithilfe des Fluorophors Protoporphyrin IX (PpIX) und eine anschließende Detektion der zugehörigen Fluoreszenz verbessert werden. In diesem Zusammenhang werden die jeweiligen Vor- und Nachteile zweier verschiedener PpIX-Anregungswellenlängen unter klinisch relevanten Bedingungen erörtert [1]. Zur Erhöhung der Sicherheit bei der Biopsie werden zwei unterschiedliche Verfahren zur Blutgefäßerkennung vorgestellt: eines beruht auf der spektrometrischen Analyse des vom Gewebe zurückgestreuten Lichts [2], das andere auf der Detektion des intravenös verabreichten Fluorophors Indocyaningrün [3].

1.1 Medizinisch-biologischer Hintergrund

1.1.1 Klinisches Hauptanwendungsgebiet: maligne Gliome

Die in dieser Arbeit dargestellten Konzepte wurden speziell für den Fall der stereotaktischen Biopsie von Hirntumoren entwickelt. Die zugrundeliegenden Prinzipien, die auf dem modifizierten Stoffwechsel der Tumorzellen sowie auf der Lichtausbreitung in Gewebe beruhen, lassen sich jedoch bei entsprechender Anpassung der medizinischen Instrumente ohne weiteres auch auf vielfältige andere Raumforderungen wie beispielsweise Prostatakarzinome oder Lebermetastasen übertragen. Im Hinblick auf den Hauptanwendungszweck der in der Entwicklung befindlichen Biopsienadel beschränkt sich dieses Kapitel jedoch auf die Beschreibung der häufigsten primären Hirntumoren.

Mit einer relativen Häufigkeit von 80% stellen Gliome die größte Gruppe innerhalb der primären malignen Hirntumoren dar [4]. Sie haben ihren Ursprung in den Stützzellen des Gehirns (Gliazellen) und werden anhand des jeweils vorherrschenden Zelltyps in Astrozytome, Oligodendrogliome, Ependymome und Mischformen dieser Typen unterteilt. Die Prognose ist bei malignen Gliomen im Allgemeinen schlecht, da sie umliegendes Gewebe diffus infiltrieren und ihre Zellen eine hohe Migrationsfähigkeit besitzen. Diese Eigenschaften sind ursächlich für den begrenzten Erfolg nicht nur der lokalen Therapien wie Resektion und Strahlentherapie, sondern auch der systemischen Chemotherapie, da migrierende Zellen sich seltener in der für zytotoxische Medikamente empfindlichen Teilungsphase befinden [5].

Nach der Klassifikation der World Health Organization (WHO) kommen Gliome in vier Malignitätsgraden vor. Der bösartigste und gleichzeitig mit einem Anteil von 45% an allen Gliomen [6] häufigste Vertreter ist das Glioblastom (fachsprachlich Glioblastoma multiforme, GBM), welchem der Grad IV (WHO) zugeordnet wird. Das Standard-Therapiekonzept beinhaltet eine möglichst weitgehende Tumorresektion mit anschließender Kombination aus Strahlentherapie und Chemotherapie mit Temozolomid [7, 8]. Selbst mit Behandlung beträgt die 5-Jahres-Überlebensrate weniger als 5% [9-11]. Die mediane Überlebensdauer ist altersabhängig, sie reicht von 6 - 9 Monaten für Patienten über 50 Jahren bis zu 18 - 21 Monaten für Patienten zwischen 18 und 30 Jahren [12].

1.1.2 Stereotaktische Biopsie

Für die Sicherung und Differenzierung der Diagnose eines vermuteten Hirntumors, speziell eines GBM, ist die histologische Untersuchung einer Gewebeprobe über konventionelle Bildgebungsverfahren wie Computertomographie (CT) oder Magnetresonanztomographie (MRT)

hinaus von essentieller Bedeutung [5]. Insbesondere ermöglicht eine Gewebeprobe das Aufspüren bestimmter molekularer Marker, die sowohl die Prognose als auch die Therapieplanung maßgeblich beeinflussen und somit zu einer personalisierten Behandlungsstrategie beitragen [13, 14]. Beispiele für genetische Marker, die eine erhöhte Therapieempfindlichkeit und eine längere Überlebensdauer versprechen, sind Mutationen auf den Isozitatdehydrogenase-Genen IDH 1/2 und Allelverluste (loss of heterozygosity = LOH) auf den Chromosomen 1p und 19q [5, 15]. Einen besonders wichtigen Marker stellt die Methylierung des Genpromotors der O⁶-Methylguanin-DNA-Methyltransferase (MGMT) dar. MGMT ist ein zentrales Desoxyribonukleinsäure(DNA)-Reparaturenzym; eine Methylierung seines Genpromotors sorgt für eine reduzierte Synthese dieses Enzyms und somit für eine erhöhte Empfindlichkeit gegenüber DNA-alkylierenden Chemotherapeutika wie Temozolomid [16]. Insbesondere bei nur unter großem Risiko resezierbaren GBM stellt der MGMT-Status einen entscheidenden Marker dar, da bei einem positiven MGMT-Befund eine Chemotherapie mit Temozolomid erfolversprechend ist und eventuell einer chirurgischen Tumorentfernung vorgezogen werden könnte.

Die Entnahme einer Gewebeprobe kann entweder offen-chirurgisch (während einer Operation) oder – vor allem bei inoperablen Hirntumoren – minimal-invasiv in Form einer stereotaktischen Biopsie erfolgen. Bei der traditionellen, rahmenbasierten Biopsie (siehe Abbildung 1) wird eine Biopsienadel (Außendurchmesser 1 - 2 mm) am stereotaktischen Rahmen befestigt, der durch Fixateure am Schädelknochen des Patienten angebracht ist, und entlang einer zuvor anhand von MRT- oder CT-Bildern berechneten Trajektorie ins Gehirn eingeführt, bis sich das distale Nadelende in einem Bereich vitalen Tumorgewebes befindet. Häufig werden pro Biopsie mehrere Gewebeproben entnommen, um eine möglichst hohe diagnostische Aussagekraft zu erreichen [15, 17]. Bei neueren Biopsiesystemen wird auf den Rahmen verzichtet, ohne an Genauigkeit gegenüber der rahmenbasierten Biopsie einzubüßen [18]. Bei dieser rahmenlosen stereotaktischen Biopsie wird die Nadel mittels Neuronavigation geleitet, das bedeutet, der Abgleich der verschiedenen Koordinatensysteme (während der Bildgebung und während der Biopsie) erfolgt über charakteristische Punkte auf der Hautoberfläche oder über Marker, die bereits während der CT- oder MRT-Aufnahme vorhanden waren.

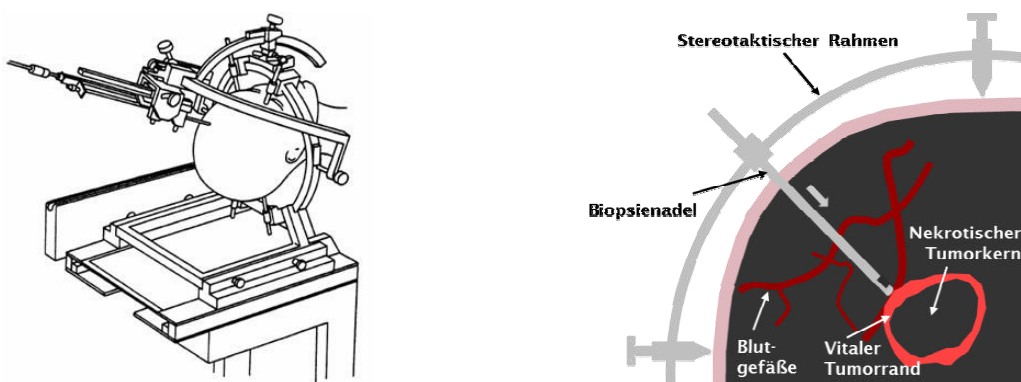


Abbildung 1: Rahmenbasierte stereotaktische Biopsie. **Links:** Außenansicht (Skizze). **Rechts:** Querschnitt durch den Kopf als Schemazeichnung nach [1, 2]. Die Biopsienadel wird am stereotaktischen Rahmen befestigt und entlang einer zuvor berechneten Trajektorie (dicker grauer Pfeil) ins Gehirn eingeführt, bis sich das distale Nadelende in einem Gebiet vitalen Tumorgewebes (hellrot) befindet.

1.1.3 Tumormarkierung mittels 5-Aminolävulinsäure-induzierter Protoporphyrin-IX-Fluoreszenz

Durch das diffuse Wachstum, das Gliomen immanent ist, ist eine exakte Abgrenzung des Tumors gegenüber dem umgebenden gesunden Gewebe äußerst schwierig. Abhilfe kann hier eine selektive Tumormarkierung mittels 5-Aminolävulinsäure(5-ALA)-induzierter PpIX-Fluoreszenz schaffen. Dieses Verfahren nutzt die Häm-Biosynthese (siehe Abbildung 2). Bei diesem Stoffwechselprozess werden je acht Moleküle Glycin und Succinyl-Coenzym A (Succinyl-CoA) über diverse enzymgestützte Zwischenschritte, die teilweise in den Mitochondrien, teilweise im Zytoplasma

stattfinden, zu einem Molekül Häm synthetisiert, welches sowohl für die an der Atmungskette beteiligten Cytochrome P450 als auch für die Synthese des sauerstoffbindenden Hämoglobins in den Erythrozyten benötigt wird [19]. Eine negative Rückkopplung vom Endprodukt Häm zum Enzym 5-ALA-Synthase, welches die Bildung von 5-ALA aus Glycin und Succinyl-CoA katalysiert, regelt die Häm-Synthese. Der direkte Vorläufer von Häm ist der Fluorophor PpIX, welcher aus vier zyklisch angeordneten Pyrrolringen mit einem delokalisierten π -Elektronensystem besteht.

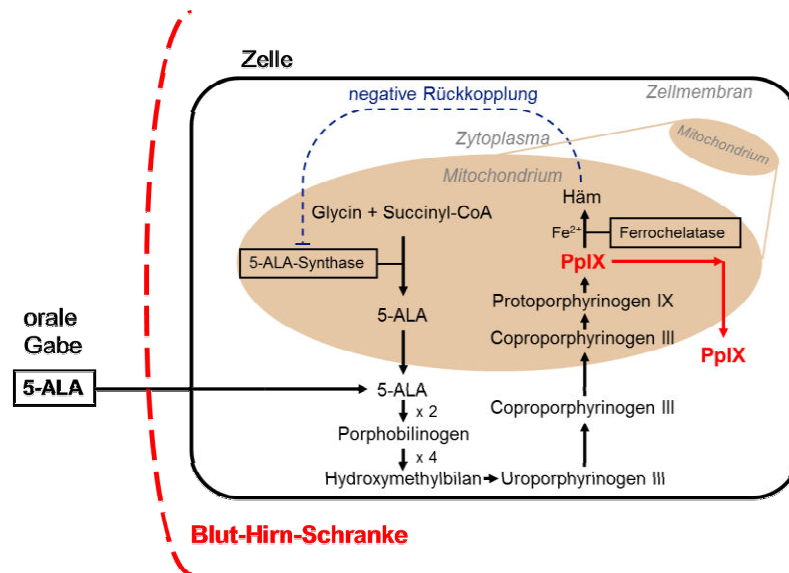


Abbildung 2: Vereinfachtes Schema der Häm-Biosynthese. Durch orale Gabe von 5-Aminolävulinsäure (5-ALA) wird der negative Rückkopplungsmechanismus umgangen, sodass eine Akkumulation des Fluoreszenzfarbstoffs Protoporphyrin IX (PpIX) erreicht werden kann. Die selektive Anreicherung in Tumorzellen kann – unter anderem – auf eine defekte Blut-Hirn-Schranke [20, 21] und eine reduzierte Ferrochelataseaktivität [22] zurückgeführt werden.

Über externe (z.B. orale) Gabe von 5-ALA kann die negative Rückkopplung umgangen und eine Akkumulation des Fluorophors PpIX in den Mitochondrien und im Zytoplasma des vitalen Tumorgewebes erreicht werden. Für die Tumorselektivität dieser Akkumulation, die insbesondere beim GBM stark ausgeprägt ist, gibt es mehrere Gründe: Eine Grundselektivität für Tumorzellen liegt in veränderten Aktivitäten der beteiligten Enzyme begründet. Besonders hervorzuheben ist hierbei die im Tumor reduzierte Aktivität der Ferrochelatase, die den letzten Schritt der Häm-Biosynthese, nämlich den Einbau eines Eisenatoms in das PpIX-Molekül, katalysiert [22]; der PpIX-Abbau wird im Tumor also gebremst. Zusätzlich gibt es, zumindest in bestimmten Tumorentitäten, eine geringere Verfügbarkeit von Eisen [23]. Insgesamt ergibt sich so ein „Rückstau“ des Häm-Vorläufers PpIX. Bei Hirntumoren kommt noch ein weiterer Aspekt hinzu: Im gesunden Hirngewebe verhindert die dichte Anordnung von Endothelzellen in den Blutgefäßen (auch Blut-Hirn-Schranke genannt) den Transport von 5-ALA in das Interstitium weitgehend [20]. Im Bereich des Tumors ist die Blut-Hirn-Schranke jedoch häufig defekt, sodass 5-ALA in deutlich erhöhtem Maße für eine mögliche Aufnahme in die Tumorzellen zur Verfügung steht [20, 21]. Die resultierenden PpIX-Konzentrationen in hochgradig malignen Gliomen reichen von einigen Hundert nM bei Grad-III-Gliomen bis hin zu einigen μ M bei GBM [24].

Die tumorselektive PpIX-Akkumulation wird bei der fluoreszenzgestützten Resektion (FGR) verwendet, um die Grenzen eines Hirntumors mithilfe eines Fluoreszenzmikroskops besser zu erkennen und so eine möglichst weitgehende Entfernung des Tumors (= gross total resection, GTR) über das aus der CT- oder MRT-Bildgebung bekannte kontrastmittelaufnehmende Volumen hinaus zu erreichen. Dem Patienten werden hierfür etwa vier Stunden vor der Operation 20 mg/kg Körpergewicht 5-ALA oral verabreicht. Die Tumormarkierung weist in der Folge laut Metastudien von Eljamel [25], Su et al. [26] und Zhao et al. [27] in hochgradig malignen Gliomen

Sensitivitätswerte zwischen 83% und 87% und Spezifitätswerte zwischen 89% und 91% auf. Der klinische Nutzen der FGR konnte in einer Studie von Stummer et al. an Patienten mit malignen Gliomen gezeigt werden, bei der sich die progressionsfreie Überlebensrate nach sechs Monaten von 21,1% in der Kontrollgruppe (weißlichtgestützte Resektion) auf 41,0% in der durch FGR behandelten Patientengruppe erhöhte [28]. Es bietet sich an, die Tumormarkierung mittels 5-ALA-induzierter PpIX-Fluoreszenz unter Verwendung faserbasierter Optik – wie in Kapitel 1.3.2 beschrieben – auch für die stereotaktische Biopsie maligner Hirntumoren zu nutzen, um die Unterscheidung zwischen Tumor- und Normalgewebe zu erleichtern. Über diese diagnostischen Anwendungen hinaus wird die tumorselektive PpIX-Akkumulation auch für die Photodynamische Therapie (PDT), beispielsweise von malignen Gliomen, genutzt, da PpIX neben seinen Fluoreszenzeigenschaften auch als Photosensibilisator wirkt [29, 30].

1.2 Problemstellung

1.2.1 Erhöhung der diagnostischen Aussagekraft des Biopsats

Für histopathologische Untersuchungen sind Biopsien aus vitalem Tumorgewebe am besten geeignet, nekrotisches Gewebe hingegen ist für die Diagnostik unbrauchbar [15, 31]. Trotz stereotaktischer Planung kommt es vor, dass das distale Biopsienadelende falsch positioniert wird und daher Gewebeprobe gewonnen werden, die keinen verwertbaren Befund liefern. Mögliche Gründe hierfür sind Ungenauigkeiten sowohl in der Bildgebung als auch im stereotaktischen Zielsystem sowie der sogenannte brain shift. Dieser entsteht, wenn die Biopsienadel ins Gehirn eingeführt und dadurch Gewebe verdrängt wird. Unklare oder sogar falsch-negative Befunde, die eventuell eine optimale Therapie verhindern, könnten die Folge sein. Tatsächlich schwankt die diagnostische Ausbeute der stereotaktischen Biopsie, das heißt der Anteil der Biopsieprozeduren, die zu einem verwertbaren Befund führen, je nach Studie zwischen 76% und 99% [17, 32-36]. Das bedeutet, dass in einer nicht unerheblichen Zahl von Fällen keine ausreichend aussagekräftige Gewebeprobe entnommen wird. Eine zusätzliche Unterstützung für den Neurochirurgen während der Biopsie wäre also von Nutzen. Eine Tumorerkennung mittels PpIX, wie in Kapitel 1.1.3 beschrieben, könnte die diagnostische Ausbeute vermutlich verbessern und im Idealfall die Zahl der pro Biopsieprozedur zu entnehmenden Proben auf eins reduzieren. Da mit jeder einzelnen Gewebeentnahme das Risiko einer Komplikation (z.B. einer intrakraniellen Blutung, siehe Kapitel 1.2.2) besteht, würde sich allein durch diese Reduktion auch die Sicherheit des Verfahrens erhöhen. Die Idee, die PpIX-Tumormarkierung mit der stereotaktischen Biopsie zu verknüpfen, wurde bereits in einigen Studien umgesetzt, bei denen die frisch entnommenen Gewebeprobe unter einem FGR-tauglichen Operationsmikroskop auf Fluoreszenz überprüft wurden; die diagnostische Ausbeute der fluoreszierenden Proben war dabei stets 100% [37-39]. Eine Fluoreszenzdetektion in situ, also vor der Gewebeentnahme, wäre allerdings noch vorteilhafter, da man sich auf Bereiche klar erkennbarer Fluoreszenz beschränken und so die Anzahl der zu entnehmenden Proben noch zuverlässiger reduzieren könnte. Denkbar wäre in diesem Zusammenhang ein endoskopisches System wie von Eigenbrod et al. [15] skizziert; eine fest in die mechanische Biopsienadel integrierte faserbasierte Sonde (siehe Kapitel 1.3) hätte zusätzlich den Vorteil, dass sie vor der Gewebeentnahme nicht entfernt werden müsste, sodass eine höhere Kongruenz aus optisch untersuchtem und mechanisch entnommenem Volumen erreicht werden könnte.

1.2.2 Vermeidung von intrakraniellen Blutungen

Eine der größten Gefahren bei der stereotaktischen Biopsie besteht darin, ein größeres Blutgefäß zu verletzen und so eine intrakranielle Blutung auszulösen. Solch eine Blutung innerhalb des Schädelknochens (Cranium) ist aufgrund der mit ihr verbundenen Erhöhung des intrakraniellen

Drucks besonders gefährlich; sie kann schwere neurologische Schäden verursachen und im äußersten Fall zum Tod führen [4]. Die Häufigkeit des Auftretens von Blutungen während stereotaktischer Biopsien liegt bei etwa 0,3% bis 7% [4, 40-43]; Kulkarni et al. [44] fanden sogar eine erstaunlich hohe Rate (54%) an während der Biopsieprozedur unerkannten Blutungen, die erst in postoperativen CT-Bildern sichtbar waren und teilweise zu verzögerten neurologischen Defiziten führten. Intrakranielle Blutungen stellen die bei weitem häufigste Form aller Komplikationen dar, aus denen sich insgesamt biopsiebedingte Morbiditäts- und Mortalitätsraten von bis zu 12% [15, 35, 42, 45, 46] bzw. 3,8% [4, 35, 44, 46] ergeben.

Aus diesen Zahlen lässt sich der klinische Bedarf für ein Verfahren zur Blutgefäßerkennung während der stereotaktischen Biopsie ableiten, das es dem Neurochirurgen erleichtert, eine intrakranielle Blutung zu vermeiden. Bisherige Ansätze zur Lösung dieses Problems verwenden beispielsweise Doppler-Sonographie [47], Laser-Doppler-Flowmetry [48], ICG-Endoskopie [49] oder interstitielle optische Tomographie [50, 51]. Sie benötigen häufig Sonden, die nicht fest in die Nadel integriert werden können und daher vor der Gewebeentnahme wieder entfernt werden müssen, und haben unter anderem deshalb noch keine flächendeckende Anwendung erfahren. In dieser Arbeit werden zwei optische Verfahren zur Blutgefäßerkennung vorgestellt (siehe Kapitel 1.3.3 und 1.3.4), die ohne größeren Aufwand unter Verwendung einer fest in der Nadel installierten Fasersonde implementiert werden können.

1.3 Opto-mechanische Biopsienadel mit integrierter Tumor- und Blutgefäßerkennung

1.3.1 Mechanische Biopsienadel

Als Grundlage der zu entwickelnden opto-mechanischen Biopsienadel dient ein Biopsiekanülensystem aus zwei gegeneinander rotierbaren Kanülen, die an ihren distalen Enden jeweils ein seitliches Fenster zur Gewebeaspiration aufweisen. Abbildung 3 zeigt die innere der Kanülen (innerer/äußerer Durchmesser: 1,1 mm / 1,4 mm). Das angesaugte Gewebe wird durch koaxiales Drehen der inneren gegenüber der äußeren Kanüle (innerer/äußerer Durchmesser: ~ 1,5 mm / 1,8 mm) abgeschert. Dieser Biopsienadeltyp (Nashold biopsy needle) wird häufig für die stereotaktische Biopsie verwendet [18, 37, 38, 51, 52]; für die in dieser Arbeit beschriebenen Experimente kamen Exemplare der Firma Pajunk (PAJUNK® BrainPro biopsy cannula set, Pajunk GmbH, Geisingen, Deutschland) zum Einsatz.

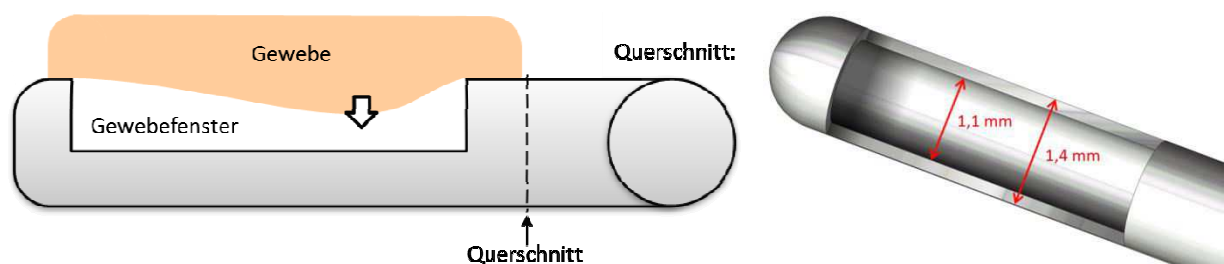


Abbildung 3: Innere Kanüle einer rein mechanischen (unmodifizierten) Biopsienadel mit seitlichem Gewebefenster zur Gewebeaspiration. Die Gewebeprobe wird vom Gehirn abgetrennt, indem die innere Kanüle nach der Aspiration relativ zur äußeren Kanüle (nicht gezeigt) gedreht wird. **Links:** Längsschnitt (Schemazeichnung). **Rechts:** 3D-Modell.

1.3.2 Tumordetektion mittels Protoporphyrin-IX-Fluoreszenz

Wie bereits in Kapitel 1.2.1 erläutert, soll über in die Biopsienadel integrierte Glasfasern vitales Tumorgewebe mittels PpIX-Fluoreszenz in situ, also direkt am Ort der Entnahme, identifiziert werden. Ein gewichtiges Problem stellen dabei mögliche (moderate) Einblutungen in den Biopsiekanal und – sobald geöffnet – in das Gewebefenster dar, die durch die Verletzung kleiner Blutkapillaren ausgelöst und praktisch nicht vollständig vermieden werden können. Auf diese Weise entstehende Blutschichten

zwischen Tumorgewebe und Faseroptik könnten den tumorspezifischen Fluoreszenznachweis verhindern und wären aufgrund der begrenzten Platzverhältnisse im Biopsiekanal auch nur schwer zu entfernen.

Angesichts dieser Problematik erscheint es fraglich, ob der üblicherweise für die FGR verwendete Spektralbereich um 405 - 410 nm zur PpIX-Anregung benutzt werden sollte, da violettes Licht sehr stark von Blut absorbiert wird. Wie das PpIX-Anregungsspektrum in Abbildung 4 (kleines Bild rechts oben) zeigt, gibt es neben diesem Hauptmaximum (Soret-Bande) noch Nebenmaxima (Q-Banden) bei größeren Wellenlängen, welche eine größere Lichteindringtiefe in Blut und umliegendem Gewebe ermöglichen. Das langwelligste Nebenmaximum, das aufgrund der hier bereits deutlich reduzierten Lichtabsorption durch das Molekül Hämoglobin (siehe Abbildung 5 links) die beste Alternative darstellt, liegt im roten Spektralbereich bei etwa 633 - 635 nm und wird gewöhnlich für die PDT verwendet [53]. Um die jeweiligen Vor- und Nachteile der beiden genannten Spektralbereiche quantitativ gegeneinander abzuwägen, wurden Phantomexperimente und Monte-Carlo-gestützte Raytracing-Simulationen für die repräsentativen Wellenlängen 405 nm und 633 nm durchgeführt [1].

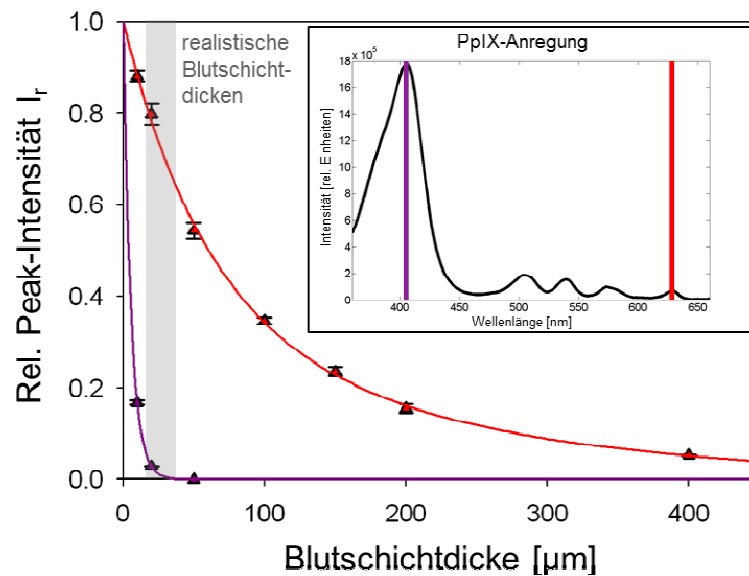


Abbildung 4: Großes Bild: Abschwächung des PpIX-Fluoreszenzsignals durch Blutschichten verschiedener Dicke bei Anregung mit 405 nm (violett) und 633 nm (rot). Klinisch besonders relevant sind Blutschichtdicken von etwa 20 μm bis 40 μm . Gezeigt sind Simulationsergebnisse sowie Fits durch die Mittelwerte aus drei statistisch unabhängigen Simulationen pro Blutschichtdickenwert; die experimentellen Ergebnisse (siehe [1]) wurden hier der Übersichtlichkeit halber weggelassen.

Kleines Bild: PpIX-Anregungsspektrum in biologischem Gewebe. Die beiden Wellenlängen 405 nm und 633 nm sind markiert. Graphik bearbeitet nach [1].

Im Rahmen dieser Arbeit konnte gezeigt werden, dass eine Anregung mit Licht der Wellenlänge 405 nm bei direktem Kontakt zwischen Faser (kombinierte Anregungs- und Detektionsfaser, Kerndurchmesser: 200 μm , numerische Apertur: 0,22) und Gewebe für unendlich große Tumorumfänge, d.h. für Tumorabmessungen, die deutlich größer sind als die optischen Eindringtiefen der beteiligten Wellenlängen (x_{opt} (405 nm) = 0,21 mm, x_{opt} (633 nm) = 1,3 mm, berechnet aus den Daten von [54] und [55]), eine um den Faktor 50 höhere Sensitivität liefert als eine Anregung mit Licht der Wellenlänge 633 nm [1]. Dieses Ergebnis war aufgrund der deutlich höheren Anregungseffizienz der PpIX-Moleküle im violetten im Gegensatz zum roten Spektralbereich zu erwarten (siehe Abbildung 4, kleines Bild). Simulationen zeigen, dass sich der genannte Faktor noch bis auf maximal 100 erhöht, wenn die Tumorgröße klein gegenüber den optischen Eindringtiefen der beteiligten Wellenlängen ist [1]. Da bei einer Biopsie jedoch gewöhnlich Gewebeproben von mindestens 1 mm^3 entnommen werden [15] – ein Volumen, bei dem die Erhöhung des Faktors nur etwa 10% beträgt [1] – spielt dieser Effekt in der Praxis nur eine untergeordnete Rolle.

Ungeachtet des deutlichen Sensitivitätsvorteils der violetten Anregungswellenlänge legen die ermittelten Detektionslimits, definiert als minimal detektierbare PpIX-Konzentrationen bei einer gegebenen Anregungsleistung (405 nm: 4 nM·mW, 633 nm: 200 nM·mW)¹, nahe, dass typische physiologische PpIX-Konzentrationen in GBM von einigen μM [24, 56-59] auch mit der roten Anregungswellenlänge ausreichend stark zur Fluoreszenz angeregt werden können und somit gut erkennbar sein sollten. Hinzu kommt die wesentlich reduzierte Empfindlichkeit gegenüber Blutschichten zwischen Faser und Tumorgewebe. Während bereits bei einer Blutschichtdicke von 50 μm Anregungslicht der Wellenlänge 405 nm (optische Eindringtiefe in Blut: $x_{\text{opt, Blut}} = 5,3 \mu\text{m}$ [60]) vollständig geblockt wird, sodass kein Fluoreszenzsignal mehr detektierbar ist, beträgt die Reduktion des mit 633 nm (optische Eindringtiefe in Blut: $x_{\text{opt, Blut}} = 0,85 \text{ mm}$ [60]) angeregten Signals bei derselben Blutschichtdicke weniger als 50% (siehe Abbildung 4, großes Bild). Selbst durch 400 μm Blut kann bei dieser Anregungswellenlänge eine noch ausreichende Fluoreszenzintensität nachgewiesen werden. In Experimenten an Agarosephantomen, deren mechanische Eigenschaften dem Hirn nachgebildet waren [1, 61-63], wurde gezeigt, dass selbst beim Vorschub eines chirurgischen Instruments durch einen Blutstropfen hindurch mit Blutschichtdicken von etwa 20 μm bis 40 μm gerechnet werden muss [1];² der entsprechende Bereich ist in Abbildung 4 (großes Bild) grau schraffiert. Folglich muss der unterschiedlichen Empfindlichkeit der beiden Wellenlängen gegenüber Blutschichten ein hoher Stellenwert eingeräumt werden. Darüber hinaus entsprechen die Abmessungen des Gewebefensters eher der optischen Eindringtiefe bei 633 nm ($x_{\text{opt}} = 1,3 \text{ mm}$) als bei 405 nm ($x_{\text{opt}} = 0,21 \text{ mm}$), daher wird mit einer Anregung bei 633 nm eine bessere Abdeckung zwischen optisch untersuchtem und mechanisch entnommenem Gewebe erreicht [64].

Insgesamt kann geschlussfolgert werden, dass eine PpIX-Anregung im roten Spektralbereich bei hochgradig malignen Gliomen mit starker PpIX-Akkumulation (wie GBM) wohl zu bevorzugen ist. Gerade für die Detektion von Tumoren mit schwächerer PpIX-Akkumulation könnten jedoch auch Biopsienadelvarianten von Vorteil sein, bei denen beide Wellenlängen mit ihren jeweiligen Vorzügen kombiniert werden.

Der Anteil von Niklas Markwardt an dieser Studie bestand sowohl in der Konzeption als auch in der Durchführung und Auswertung der Experimente und Simulationen sowie im Verfassen des Manuskripts mit Anregungen, Korrekturen und Unterstützung durch die anderen Autoren.

1.3.3 Blutgefäßdetektion mittels Remissionsspektrometrie

Für eine erhöhte Sicherheit der stereotaktischen Biopsie ist die Erkennung von Blutgefäßen im Gewebefenster (siehe Abbildung 3 links) von zentraler Bedeutung, da hier durch den in Kapitel 1.3.1 beschriebenen Abschermechanismus die Gefahr der Gefäßverletzung und folglich auch der Auslösung einer intrakraniellen Blutung am höchsten ist. Wie in Manuskript [2] gezeigt wird, kann zu diesem Zweck ein Verfahren angewandt werden, das sich die charakteristische Absorption des Hämoglobins (siehe Abbildung 5 links), des Hauptabsorbers in Blut, zunutze macht. Dazu werden in die Nadel zwei Seitblickfasern integriert, die durch Abschleifen der distalen Enden unter 45° und anschließende Verspiegelung mittels Aluminium-Beschichtung unter Hochvakuum hergestellt worden sind. Eine der beiden Fasern wird zur Emission von Licht verwendet. Das emittierte Spektrum sollte dabei mindestens zwei Wellenlängen mit deutlich voneinander abweichender Hämoglobinabsorption enthalten, beispielsweise die in Abbildung 5 links markierten Wellenlängen 578 nm und 650 nm, zwischen denen die Absorptionskurven von oxygeniertem (HbO_2) und deoxygeniertem (Hb) Hämoglobin stark abfallen. Der Zweck der zweiten Seitblickfaser ist die Detektion des vom Gewebe remittierten (=zurückgestreuten) Lichts, das anschließend, zum Beispiel mithilfe eines Spektrometers, analysiert wird. Das Verhältnis R der Remissionsintensitäten I bei den beiden Wellenlängen (z.B.

¹ Den Berechnungen wurde die (konservative) Abschätzung zugrunde gelegt, dass eine Signalstärke, die das Dreifache des Hintergrundrauschens beträgt, gerade noch detektiert werden kann.

² Im Gewebefenster können vermutlich noch bedeutend größere Schichtdicken entstehen.

Intensität bei 578 nm / Intensität bei 650 nm: $R = I_{578}/I_{650}$) wird durch das Vorhandensein eines Blutgefäßes im Gewebefenster beeinflusst (in diesem Fall reduziert, Abbildung 5 rechts), sodass der Neurochirurg bei bestehendem Risiko vor der Gewebeentnahme gewarnt werden kann.

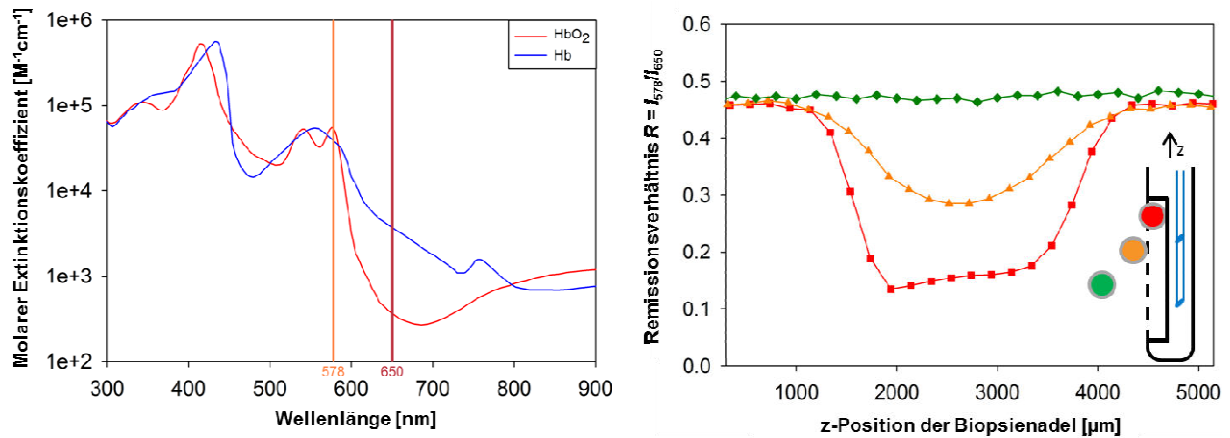


Abbildung 5: Remissionsspektrometrie zur Erkennung von Blutgefäßen im Gewebefenster einer Biopsienadel. Graphik bearbeitet nach [2]. **Links:** Absorptionsspektren von oxygeniertem (HbO₂) und deoxygeniertem (Hb) Hämoglobin. Durch Vergleich der zurückgestreuten Lichtintensitäten I bei den Wellenlängen 578 nm (orange) und 650 nm (dunkelrot) können Blutgefäße detektiert werden. **Rechts:** Messergebnis eines Phantomexperiments. Je nach Entfernung des Blutgefäßes (dargestellt durch verschiedenfarbige Kreise im kleinen Bild) von der Faseronde (blau im kleinen Bild) ist die Blutsignatur im gemessenen Signal, also die Verringerung des Remissionsverhältnisses, unterschiedlich stark ausgeprägt.

Mithilfe von Phantom- und Gewebeexperimenten sowie Raytracing-Simulationen wurde neben der prinzipiellen Anwendbarkeit der Methode die Abhängigkeit des Verhältnisses $R = I_{578}/I_{650}$ von verschiedenen Parametern wie dem Abstand zwischen den distalen Enden der Seitblickfasern (Faser-Faser-Abstand), dem Abstand zwischen dem Blutgefäß und den Seitblickfasern (Faser-Gefäß-Abstand) sowie der Sauerstoffsättigung, der Orientierung und dem Durchmesser des Blutgefäßes untersucht. Es konnte gezeigt werden, dass Blutgefäße ab einem Durchmesser von etwa 100 - 500 µm, unabhängig von ihrer Orientierung, bis zu einem Faser-Gefäß-Abstand von etwa 800 µm deutlich erkannt werden können (siehe Abbildung 5 rechts, rote Kurve). Bis zu diesem Abstand von den Fasern befindet sich ein Blutgefäß gerade noch innerhalb des Gewebefensters, ist also der Gefahr einer Zerstörung ausgesetzt. Blutgefäße, die sich deutlich außerhalb des Gewebefensters befinden, beeinflussen das Remissionsverhältnis dagegen nur sehr geringfügig bis gar nicht (siehe Abbildung 5 rechts, grüne Kurve). Die Positionierung der bearbeiteten Faserenden im Gewebefenster sollte so gewählt werden, dass das optisch untersuchte Volumen den Raum innerhalb des Gewebefensters, in dem ein Blutgefäß erkannt werden soll, möglichst gut abdeckt. Ein Faser-Faser-Abstand von 2 mm erwies sich als praktikabel. Da die Empfindlichkeit gegenüber Blutgefäßen, die sich innerhalb des Gewebefensters, aber außerhalb des Bereichs zwischen den beiden distalen Faserenden befinden, deutlich reduziert ist, sollte die Länge des Gewebefensters nicht größer als etwa 4-5 mm sein.

Der Anteil von Niklas Markwardt an dieser Studie bestand in der Erfindung und Entwicklung der Methode gemeinsam mit Herbert Stepp, in der Konzeption sowie in der Durchführung und Auswertung der Experimente und Simulationen sowie im Verfassen des Manuskripts mit Anregungen, Korrekturen und Unterstützung durch die anderen Autoren.

1.3.4 Blutgefäßdetektion mittels Indocyaningrün-Fluoreszenz

Auch beim Vorschub der Biopsienadel zum geplanten Ort der Gewebeentnahme besteht ein gewisses Risiko, ein Blutgefäß zu verletzen, das jedoch aufgrund des abgerundeten distalen Nadelendes (siehe Abbildung 3) geringer ist als innerhalb des Gewebefensters während der Gewebeentnahme. Zur Vermeidung dieses Restrisikos ließe sich prinzipiell das in Kapitel 1.3.3 beschriebene Remissionsverfahren anwenden, wobei die Seitblickfasern durch plane Fasern ersetzt werden müssten.

Diese sollten bündig mit dem distalen Ende der Biopsienadel abschließen und eine remissionsspektrometrische Untersuchung des Bereichs vor der Nadel ermöglichen. Anders als bei der Blutgefäßdetektion im Gewebefenster kommt es bei der Blutgefäßerkennung in Vorschubrichtung jedoch darauf an, eine möglichst große Detektionsreichweite zu erzielen, damit der Neurochirurg rechtzeitig vor einer möglichen Blutgefäßverletzung gewarnt werden kann. Allerdings ist der Faser-Faser-Abstand in der Vorausblick-Konfiguration durch den Durchmesser der inneren Kanüle begrenzt und kann daher nur höchstens etwa 1 mm betragen, was die Detektionsreichweite gegenüber den in Kapitel 1.3.3 angegebenen 800 μm deutlich reduziert [2].

Eine mögliche Alternative stellt die Blutgefäßerkennung mittels Indocyaningrün(ICG)-Fluoreszenz dar. Der Fluorophor ICG ist als intravenös zu verabreichendes Diagnostikum ICG-PULSION® medizinisch zugelassen. Seine Verwendung ist unter anderem für die Messung der zerebralen Durchblutung indiziert (empfohlene Dosis: 0,1 - 0,3 mg/kg Körpergewicht) [65] und erfolgt beispielsweise im Rahmen von Aneurysmen-Operationen [66, 67]. Ein großer Vorteil von ICG besteht darin, dass seine Anregungs- und Emissionsmaxima im nahinfraroten Spektralbereich um etwa 800 nm liegen [68], bei dem die optische Eindringtiefe in biologischem Gewebe gegenüber dem sichtbaren Wellenlängenbereich um bis zu einer Größenordnung erhöht ist [69]. Ein anderer Vorteil liegt in seiner relativ langen Verweildauer im vaskulären System. Sie kommt durch die Bindung der ICG-Moleküle an Proteine im Blutplasma zustande und ist nur durch die Ausscheidung über die Leber (Zeitkonstante: 0,164/min, [70]) begrenzt.

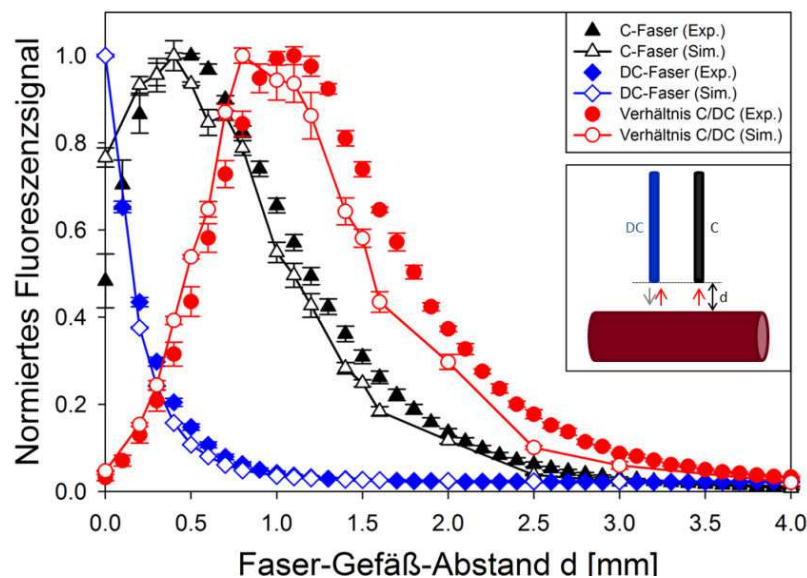


Abbildung 6: Großes Bild: Normierte Fluoreszenzsignale (bei 830 nm) der Einzelfasern (DC, C) sowie das normierte Fluoreszenzverhältnis C/DC in Abhängigkeit des Faser-Gefäß-Abstandes d , jeweils für Experiment (Exp.) und Simulation (Sim.). Der Faser-Faser-Abstand beträgt hier 1 mm. Grafik bearbeitet nach [3]. Kleines Bild: Schemazeichnung der Zwei-Faser-Sonde mit Blutgefäß.

Die in Manuskript [3] beschriebene Methode basiert auf einer Zwei-Faser-Sonde, welche in Abbildung 6, kleines Bild, dargestellt ist: Die erste Faser (DC-Faser, von engl. delivery and collection) dient zur Anregung (grau) und Detektion (rot) des Fluoreszenzlichts, die zweite Faser (C-Faser, von engl. collection) nur zur Fluoreszenzdetektion. Wie mithilfe von Phantomexperimenten und Raytracing-Simulationen gezeigt werden konnte, folgen die separat in den beiden Fasern gemessenen Fluoreszenzintensitätskurven bei Annäherung der Sonde an ein Blutgefäß ($d \rightarrow 0$) unterschiedlichen Verläufen (siehe Abbildung 6, großes Bild): Während das Signal in der DC-Faser monoton ansteigt und im Kontakt mit dem Blutgefäß sein Maximum erreicht, steigt das Signal in der C-Faser erst an, sinkt dann jedoch ab einem gewissen Abstand vom Blutgefäß wieder ab. In einem nicht streuenden Medium würde das über die C-Faser detektierte Signal sogar bis auf null sinken, was mit den

endlichen numerischen Aperturen der Fasern erklärt werden kann: Innerhalb eines gewissen Faser-Gefäß-Abstands-Bereichs können die Fluoreszenzphotonen, die durch die Anregung über die DC-Faser erzeugt werden, nämlich nicht mehr über die C-Faser detektiert werden. Die im biologischen Gewebe vorhandene Streuung schwächt diesen geometrischen Effekt etwas ab, weshalb auch in unmittelbarer Nähe des Blutgefäßes noch ein Fluoreszenzsignal über die C-Faser detektiert wird [3]. Der beschriebene charakteristische Verlauf des C-Faser-Signals kann als Signatur einer Annäherung an ein Blutgefäß aufgefasst und das Auftreten des beschriebenen Maximums als Warnsignal interpretiert werden. Durch Verhältnisbildung der beiden Signale (C/DC) entsteht eine Kurve, deren Maximum gegenüber dem C-Faser-Signal zu einem größeren Faser-Gefäß-Abstand verschoben ist. So lässt sich eine noch größere Detektionsreichweite erreichen, die vom gegenseitigen Abstand der Fasern innerhalb der Sonde abhängt. Sie beträgt bei einem Faser-Faser-Abstand von 1 mm in grauer Hirnsubstanz etwa 1,1 mm, in weißer Hirnsubstanz aufgrund der stärkeren Streuung nur etwa 0,4 mm. Die unterschiedlichen Faser-Gefäß-Abstands-Abhängigkeiten der beiden Signale ermöglichen ein reproduzierbares Verfahren zur Blutgefäßdetektion. Es ist weitestgehend unabhängig von der Blutgefäßgröße, der intravaskulären ICG-Konzentration und von lokalen Schwankungen der optischen Eigenschaften (Streuung, Absorption) des Hirngewebes.

Der Anteil von Niklas Markwardt an dieser Studie bestand in der Betreuung der Experimente, in der Konzeption sowie in der Durchführung und Auswertung der Simulationen sowie zum Teil (etwa hälftig) im Verfassen des Manuskripts.

1.3.5 Modell einer faserbasierten opto-mechanischen Biopsienadel

Eine mögliche Kombination der in den Kapiteln 1.3.2 bis 1.3.4 dargestellten Methoden ist in Abbildung 7 dargestellt. Dabei dienen zwei – bis auf eine geringfügige Anpassung an die Rundung des distalen Nadelendes – plane Glasfasern (1, 2) zur Untersuchung des Gewebes vor der Biopsienadel. Nach Verabreichung von 5-ALA kann Tumorgewebe über jede Faser einzeln mittels PpIX-Fluoreszenz nachgewiesen werden; dadurch ist es möglich, für die Biopsie geeignetes Gewebe während des Nadelvorschubs bereits grob zu lokalisieren. Im Wechsel mit dieser Tumordetektion können die beiden Fasern auch für die ICG-Blutgefäßerkennung (siehe Kapitel 1.3.4) benutzt werden, um eine Perforation eines größeren Gefäßes zu vermeiden. Zwei zusätzlich in die innere Kanüle der Biopsienadel integrierte Seitblickfasern (3, 4) dienen zur Untersuchung des aspirierten Gewebes nach Öffnen des Gewebefensters. Mithilfe des PpIX-Fluoreszenznachweises kann hier an zwei Positionen überprüft werden, ob sich tatsächlich Tumorgewebe im Fenster befindet. Darüber hinaus sind die beiden Seitblickfasern – ebenfalls alternierend mit der Tumordetektion – für die Blutgefäßerkennung mittels Remissionsspektrometrie (siehe Kapitel 1.3.3) vorgesehen. So kann unmittelbar vor Abscheren des Gewebes geprüft werden, ob eine Gewebeentnahme an dieser Stelle sinnvoll und sicher ist.

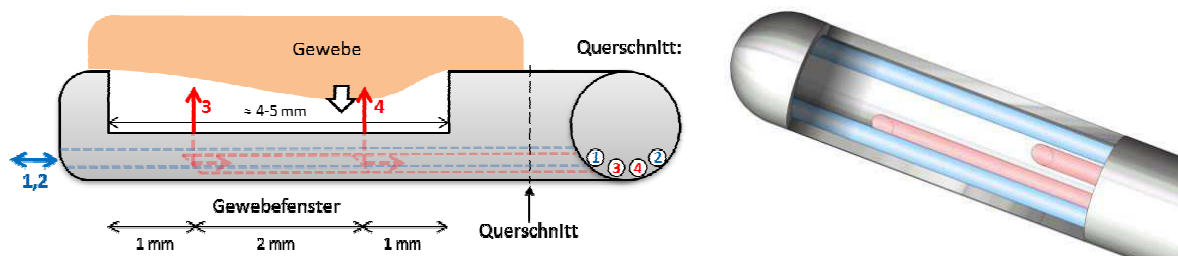


Abbildung 7 Innere Kanüle einer opto-mechanischen (mit Glasfasern versehenen) Biopsienadel. Die bis auf die Rundung des distalen Kanülenendes planen Fasern 1 und 2 dienen zur Erkennung von Tumorgewebe (PpIX-Fluoreszenz) und Blutgefäßen (ICG-Fluoreszenz) im Bereich vor der Nadel; die Seitblickfasern 3 und 4 sind für die optische Untersuchung des Gewebes innerhalb des Gewebefensters hinsichtlich Tumorgewebe (PpIX-Fluoreszenz) und Blutgefäßen (Remissionsspektrometrie) vorgesehen. **Links:** Längsschnitt (Schemazeichnung). **Rechts:** 3D-Modell.

2 ORIGINALMANUSKRIPTE

**405 NM VERSUS 633 NM FOR PROTOPORPHYRIN IX
EXCITATION IN FLUORESCENCE-GUIDED STEREOTACTIC
BIOPSY OF BRAIN TUMORS**

**Niklas A. Markwardt, Neda Haj-Hosseini, Bastian Hollnburger, Herbert Stepp,
Petr Zelenkov und Adrian Rühm**

Journal of Biophotonics 9(9), 901–912 (2016)

Copyright Wiley-VCH Verlag GmbH & Co. KGaA. Nachdruck mit Genehmigung.

Journal of

[www. biophotonics-journal.org](http://www.biophotonics-journal.org)

BIOPHOTONICS

WILEY-VCH

REPRINT

FULL ARTICLE

405 nm versus 633 nm for protoporphyrin IX excitation in fluorescence-guided stereotactic biopsy of brain tumors

Niklas A. Markwardt^{*,1}, Neda Haj-Hosseini², Bastian Hollnburger¹, Herbert Stepp¹, Petr Zelenkov³, and Adrian Rühm¹

¹ Laser-Forschungslabor, LIFE-Zentrum, Klinikum der Universität München, Munich, Germany

² Department of Biomedical Engineering, Linköping University, Linköping, Sweden

³ Burdenko Neurosurgery Institute, Moscow, Russia

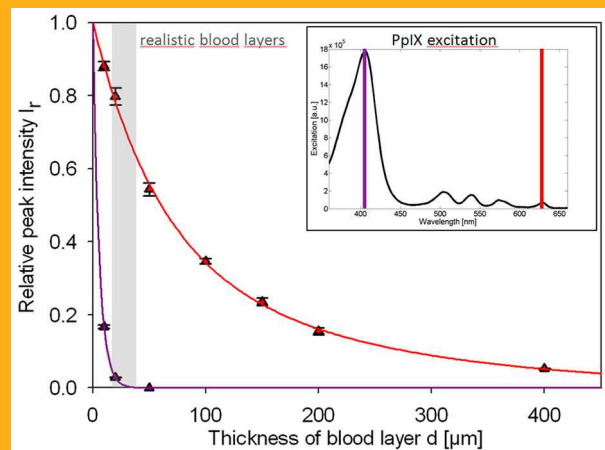
Received 16 July 2015, revised 29 October 2015, accepted 29 October 2015

Published online 14 November 2015

Key words: 5-aminolevulinic acid, protoporphyrin IX, stereotactic biopsy, fluorescence spectroscopy, glioblastoma multiforme

Fluorescence diagnosis may be used to improve the safety and reliability of stereotactic brain tumor biopsies using biopsy needles with integrated fiber optics. Based on 5-aminolevulinic-acid-induced protoporphyrin IX (PpIX) fluorescence, vital tumor tissue can be localized *in vivo* during the excision procedure to reduce the number of necessary samples for a reliable diagnosis.

In this study, the practical suitability of two different PpIX excitation wavelengths (405 nm, 633 nm) was investigated on optical phantoms. Violet excitation at 405 nm provides a 50-fold higher sensitivity for the bulk tumor; this factor increases up to 100 with decreasing fluorescent volume as shown by ray tracing simulations. Red excitation at 633 nm, however, is noticeably superior with regard to blood layers obscuring the fluorescence. Experimental results on the signal attenuation through blood layers of well-defined thicknesses could be confirmed by ray tracing simulations. Typical interstitial fiber probe measurements were mimicked on agarose-gel phantoms. Even in direct contact, blood layers of 20–40 μm between probe and tissue must be expected, obscuring 405-nm-excited PpIX fluorescence almost completely, but reducing the 633-nm-excited signal only by 25.5%. Thus, 633 nm seems to be the wavelength of choice for PpIX-assisted detection of high-grade gliomas in stereotactic biopsy.



PpIX signal attenuation through clinically relevant blood layers for 405 nm (violet) and 633 nm (red) excitation.

* Corresponding author: e-mail: Niklas.Markwardt@med.uni-muenchen.de, Phone: +49 89 4400 74880, Fax: +49 89 4400 74864

This manuscript is part of the inaugural thesis of Niklas Markwardt to be submitted at the Medical Faculty of the Ludwig-Maximilians-Universität, Munich.

1. Introduction

Gliomas account for about 80% of all primary malignant brain tumors [1]. Among these, glioblastoma multiforme (GBM) constitutes the most frequent and malignant histologic type with a very poor prognosis. It is classified as WHO grade IV and has a 5-year survival rate of less than 3% [2]. The median survival ranges from 6–9 months for patients older than 50 years to 18–21 months for patients aged between 18 and 30 [3]. Gliomas generally tend to infiltrate adjacent normal brain in a diffuse way, which prevents a clear demarcation of the tumor and represents a major factor in therapeutic failure [4, 5].

For patients with a methylated O⁶-methylguanine-DNA methyltransferase (MGMT) gene promoter, a chemotherapy based on temozolomide is promising and recommended as part of the therapeutic concept [6]. MGMT is a key enzyme for DNA repair and the methylation of its gene promoter indicates an increased sensitivity of the tumor to alkylating agents such as temozolomide. To assess the patient's MGMT status, biopsies with an approximate volume of 1 mm³ are taken [7]. The clinical benefit of this intervention is based on its potential to support personalized medicine concepts where the MGMT status is one of a panel of biomarkers [8, 9]: In specific cases of MGMT-positive patients where a resection is supposed to involve a significant risk, for instance, alkylating agents could replace surgery as first-line treatment. Other biomarkers that can be extracted from biopsies and may help to substantiate the diagnosis comprise the proliferative index Ki-67, mutations on the isocitrate dehydrogenase genes IDH1/2 and LOH (loss of heterozygosity) on chromosomes 1p and 19q [7]. Stereotactic biopsy, illustrated in Figure 1, is a standard procedure for obtaining a tissue sample of the brain tumor.

While the complication rate of this neurosurgical procedure is rather low, which becomes manifest in mortality and significant morbidity below 1% and 5%, respectively [10], incidents usually involve severe consequences. With occurrence rates ranging up to 5% [11], the most prominent complications are hemorrhages, which can lead to severe functional deficits or even the patient's death. Sampling of a non-diagnostic tissue specimen represents another risk. Due to deficits of conventional imaging techniques like CT or MRI and the inherent diffuse growth of gliomas, the distal tip of the biopsy needle may be wrongly positioned outside the region of vital tumor. False negative findings could be the consequence, potentially leading to inappropriate further treatment [12]. Actually, the reported diagnostic yield (percentage of biopsy procedures leading to conclusive histopathological diagnosis) of stereotactic biopsy ranges from 76% to 99% [13–20]. These numbers indicate that in many cases addi-

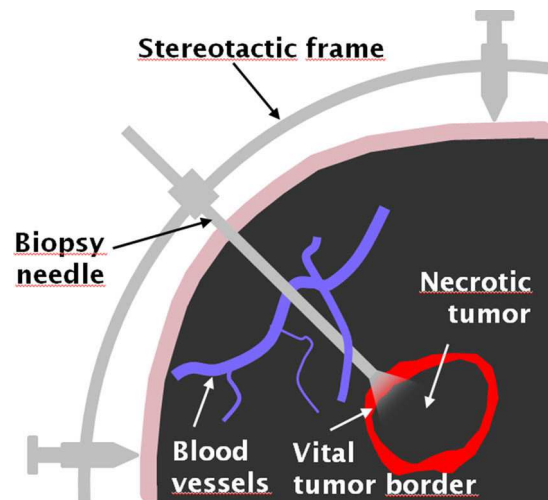


Figure 1 Stereotactic biopsy of brain tumors. A biopsy needle is attached to the stereotactic frame and inserted into the brain along a predefined trajectory until the distal needle tip is positioned in an area of vital tumor tissue.

tional support for the neurosurgeon beyond the conventional imaging techniques would be desirable. This is all the more true as usually several biopsy samples are taken to permit a diagnosis with acceptable reliability [7, 13]. Especially for deep-seated tumors, however, a minimum of biopsy samples should be aspirated to prevent neurological deficits [21].

Currently, a mechano-optical instrument for stereotactic biopsy is developed, which consists of a standard biopsy needle with integrated fiber optics. It is capable of overcoming the aforementioned problems by means of fluorescence spectroscopy. As already shown by various groups, the administration of 5-aminolevulinic acid (5-ALA) leads to a highly selective accumulation of protoporphyrin IX (PpIX) in high-grade malignant gliomas [22–24]. A tumor-related deficient blood brain barrier and an altered activity level of several enzymes including ferrochelatase, which catalyzes the conversion of PpIX to heme, are central reasons for this phenomenon [25]. Tumor recognition with 5-ALA-induced PpIX is already effectively used for fluorescence-guided resection of malignant gliomas using surgical microscopes [22, 23, 26] or fiber optical probes [27, 28]. It leads to a significantly increased complete resection rate of these diffusely growing tumors and to a significantly enhanced progression-free survival rate after 6 months, translating into a progression-free survival prolongation of 1.5 months as compared to conventional white light resection [23]. The method has also been tested on excised tissue samples during stereotactic biopsy using surgical microscopes [21, 29–31]. In the latter case, the diagnostic yield of the fluorescent samples was always 100% (total $n = 98$). Regarding the specificity to malignant tissue and the

sensitivity to GBM of 5-ALA-induced PpIX fluorescence in stereotactic biopsy, Widhalm et al. [29] report values of 100% and 98% ($n = 150$ and $n = 53$), respectively. Nevertheless, for the stereotactic biopsy procedure, the technique is even more beneficial if the detection is performed in situ before the tissue excision as already tested with an endoscopic system by Eigenbrod et al. [7] to further reduce the number of samples that have to be taken and thus minimize the risk of complications.

PpIX fluorescence can be excited in different spectral regions (see Figure 2), each offering advantages and disadvantages especially in terms of fluorescence efficiency and tissue optical properties. Commonly, violet light is used for PpIX excitation in fluorescence-guided resection. Light in this spectral range, however, is highly absorbed by blood, hence blood-covered tumor tissue may easily be missed. During open brain surgery, the blood often but not always can be removed by rinsing the probe or the surgical site; yet, even small amounts of blood will affect proper interpretation of the signals [32–34]. During stereotactic biopsy, however, rinsing appears to be even more challenging because the (diluted) blood cannot drain off and suctioning through the needle would draw even more blood towards the probe tip, at least for conventional needle designs. Even if no blood vessel disruption occurs, the microvessels in the tissue right next to the probe do sometimes obstruct the fluorescence signals. Using red light, which is already applied for fluorescence monitoring of PpIX concentrations during photodynamic therapy [35], seems to be a promising alternative as it is considerably less attenuated by blood. In this study, the potentials of the excitation wavelengths $\lambda_{\text{exc}} = 405$ nm and $\lambda_{\text{exc}} = 633$ nm are comparatively investigated with regard to their clinical applicability in stereotactic biopsy.

2. Materials and methods

2.1 Production of PpIX phantoms

Both liquid and agarose-gel phantoms were mixed to model the optical properties of brain tumors, using Lipovenös® (Fresenius Kabi GmbH, Bad Homburg, Germany) and ink (“brilliant black 4001”, Pelikan GmbH, Hannover, Germany) for scattering

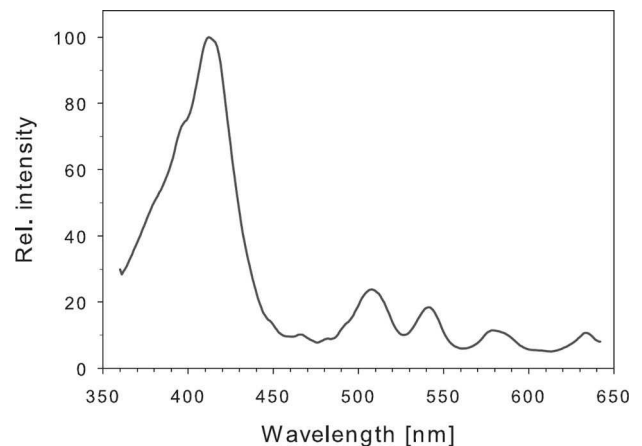


Figure 2 Excitation spectrum of PpIX in tissue (emission intensity measured at 710 nm). PpIX can be excited in different spectral regions, ranging from violet (around 405 nm) to red (around 633 nm) light.

and absorption, respectively. Separate phantoms were produced for the excitation wavelengths $\lambda_{\text{exc}} = 405$ nm and $\lambda_{\text{exc}} = 633$ nm. For this purpose, values referring to brain tumor tissue given by Gebhart et al. (determined *ex vivo* on $n = 39$ samples) [36] were taken as reference, which are in good accordance with the astrocytoma data published by Yaroslavsky et al. (*ex vivo*, $n = 4$) [37]. More recent publications from Pitzschke et al. concerning the optical properties of human (*ex vivo*, $n = 1$) [38] and rabbit (*in vivo*, $n = 7$) [39] brain tissue were additionally consulted for the red excitation. A comparison with the values of Gebhart et al. showed a reasonable accordance for the absorption coefficient and indicated that the reduced scattering coefficient of brain tumor tissue lies between those of human gray and white matter, a fact that had already been reported by Gebhart et al. The required concentrations of the phantom ingredients have been determined via literature data [40] (Lipovenös®) and integrating sphere measurements (ink), assuming a linear behavior and non-interacting particles. In Table 1, the used concentrations and simulated optical properties of the liquid phantoms are listed. In the following, μ_a denotes the absorption coefficient and $\mu'_s = \mu_s(1 - g)$ the reduced scattering coefficient where μ_s and g are the scattering coefficient and anisotropy factor, respectively.

Agarose-gel phantoms were made following the protocol of Cubeddu et al. [41]. To simulate the me-

Table 1 Liquid phantoms: Lipovenös® and ink concentrations as well as simulated μ_a and μ'_s .

Phantom (exc. wavelength)	ink concentration (vol/vol) [%]	μ_a [mm ⁻¹]	Lipovenös® concentration (mass/vol soybean oil) [%]	μ'_s [mm ⁻¹]
$\lambda_{\text{exc}} = 405$ nm	0.9	1.4	2.3	3.9
$\lambda_{\text{exc}} = 633$ nm	0.1	0.09	2.0	2.2

Table 2 Agar phantoms: Lipovenös® and ink concentrations as well as simulated μ_a and μ'_s .

Phantom (exc. wavelength)	ink concentration (vol/vol) [%]	μ_a [mm ⁻¹]	Lipovenös® concentration (mass/vol soybean oil) [%]	μ'_s [mm ⁻¹]
$\lambda_{\text{exc}} = 405$ nm	0.9	1.4	2.9	3.9
$\lambda_{\text{exc}} = 633$ nm	0.1	0.09	2.5	2.2

chanical properties of brain tissue, 0.6% (m/v) agarose powder (Sigma-Aldrich Chemie GmbH, Munich, Germany) was used [42–44]. As the addition of agarose decreases the reduced scattering coefficient of Lipovenös® (reduction by 20% at 0.6% agar) [41], slightly different Lipovenös® concentrations were used for the agar phantoms (see Table 2).

PpIX powder (Sigma-Aldrich Chemie GmbH, Munich, Germany) was dissolved in dimethyl sulfoxide (DMSO, Sigma-Aldrich Chemie GmbH, Munich, Germany) and added as fluorescence agent to both liquid and agar phantoms at varying concentrations.

2.2 Measurement setup

As shown in Figure 3, a dual-mode experimental setup was designed for two different excitation wavelengths (mode 1: $\lambda_{\text{exc}} = 405$ nm, mode 2: $\lambda_{\text{exc}} = 633$ nm). Light of both wavelengths was coupled into a single bare fiber with a numerical aperture (NA) of 0.22 and a core diameter of 200 μm (UM22-200, Thorlabs GmbH, Dachau, Germany) and directed onto a PpIX containing liquid or agar phantom. The respective excitation light power at the distal end of the fiber (next to the irradiated medium) was determined as 0.9 mW ($\lambda_{\text{exc}} = 405$ nm) and 5.5 mW ($\lambda_{\text{exc}} = 633$ nm) using a standard power meter (PM100D, sensing head: S130C, Thorlabs GmbH, Dachau, Germany). The fluorescence light was collected with the same fiber and transmitted to a detection spectrometer (USB2000+, Ocean Optics GmbH, Ostfildern, Germany), which was recorded using OOIBase32 (Ocean Optics GmbH, Ostfildern, Germany). The integration time ranged between 15 ms and 500 ms. Data processing was performed with MATLAB (The MathWorks, Inc., Natick, MA, USA) and SigmaPlot (Systat Software GmbH, Erkrath, Germany); for data smoothing, the MATLAB function *filter* was used (calculating a moving average over 10 data points, corresponding to $\Delta\lambda \approx 4$ nm).

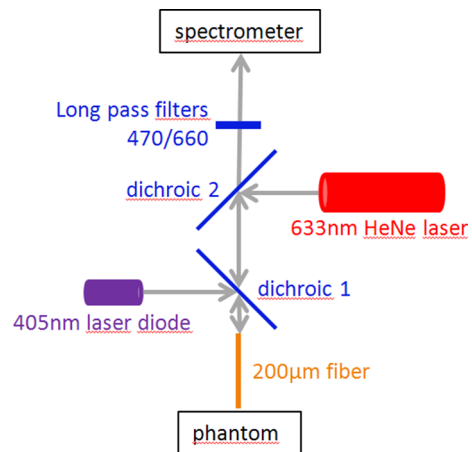


Figure 3 Dual-mode experimental setup for comparing PpIX excitation wavelengths 405 nm and 633 nm. In mode 1, only a 405 nm laser diode is switched on, the long pass filter 470 (cut-on wavelength: 470 nm) is selected and dichroic mirror 2 is hinged aside. In mode 2, only a 633 nm HeNe laser is switched on, the long pass filter 660 (cut-on wavelength: 660 nm) is selected and both dichroic mirrors are in the light path.

In mode 1, violet light from a 405 nm laser diode was reflected towards the fiber by dichroic mirror 1 (cut-off at 440 nm). Dichroic mirror 2 (cut-off at 665 nm) was removed to let fluorescence light between 600 nm and 750 nm pass to the spectrometer. In mode 2, dichroic mirror 2 was required to couple the beam of a 633 nm HeNe laser into the light path. Fluorescence light around 700 nm was guided through both dichroic mirrors towards the spectrometer. Switching between the two modes was enabled by removing (mode 1) or adding (mode 2) dichroic mirror 2 and by introducing the corresponding long pass filter. Cut-on wavelengths of 470 nm and 660 nm were used for $\lambda_{\text{exc}} = 405$ nm and $\lambda_{\text{exc}} = 633$ nm, respectively.

Three different types of measurements were performed with this setup, pertaining to the determination of PpIX detection limits (Section 2.3.1), the attenuation of PpIX signals through blood layers of

Table 3 PpIX concentrations used for the determination of PpIX detection limits.

$\lambda_{\text{exc}} = 405$ nm	50 nM	25 nM	12.5 nM	6.25 nM	0 nM (reference)
$\lambda_{\text{exc}} = 633$ nm	500 nM	250 nM	125 nM	62.5 nM	0 nM (reference)

well-defined thicknesses (Section 2.4.1) and the effectively expectable blood layer thickness in the clinical measurement situation (Section 2.5).

2.3 Determination of PpIX detection limits

2.3.1 Measurements on semi-infinite phantoms

PpIX detection limits for the above-mentioned detection fiber were determined on agar phantoms. For stereotactic biopsies, especially the sensitivity to the bulk tumor is interesting, thus the phantoms were made virtually infinitely large (cylindrical shape, diameter: 8.5 cm, height: 1.5 cm) as compared to the optical penetration depth (0.21 mm for $\lambda_{\text{exc}} = 405$ nm and 1.3 mm for $\lambda_{\text{exc}} = 633$ nm, respectively) and the fiber core diameter (200 μm) to simulate the detection of large tumor volumes. To analyze the sensitivity to smaller tumor parts, ray tracing simulations were performed (see Section 2.3.2). For both excitation wavelengths, four agar phantoms with varying PpIX concentrations and one reference phantom (without PpIX) were mixed. The concentration values, given in nM (nanomoles per liter), can be found in Table 3. Due to the expected difference in sensitivity between the two excitation wavelengths, ten times higher concentration values were used for 633 nm as compared to 405 nm.

Bringing the distal fiber end in contact with the agar phantom, the fluorescence of each phantom was measured four times at different sites to minimize the effect of photobleaching. To correct for background fluorescence, the signal of the reference phantoms was measured under the same conditions, normalized to the signal of the PpIX phantoms at 560 nm ($\lambda_{\text{exc}} = 405$ nm) and 750 nm ($\lambda_{\text{exc}} = 633$ nm), respectively, and subtracted from the raw spectra of the PpIX phantoms. Afterwards, the four single spectra of each concentration were averaged and divided by the integration time. The detection threshold was set to the threefold of the background noise level. To examine the proportionality between PpIX concentration and fluorescence signal, a linear regression of the peak intensities (averaged between 632 nm and 634 nm for $\lambda_{\text{exc}} = 405$ nm and between 701 nm and 703 nm for $\lambda_{\text{exc}} = 633$ nm) as a function of the concentration was performed. The detection limits were determined by equating the measured fluorescence intensity per concentration with the detection threshold.

2.3.2 Ray tracing simulations with variable tumor size

To investigate the sensitivity to smaller tumor parts (e.g. isolated tumor cell nests in the infiltration zone of the lesion), ray tracing simulations were performed using the Monte Carlo-based software TracePro (Lambda Research Corporation, Littleton, MA, USA). A tumor cube (fluorescent cube with optical properties of brain tumor taken from [36] and a constant PpIX concentration of 2 μM) with variable edge length between 0.04 mm and 15 mm (the latter one considered infinitely large as compared to fiber diameter and light penetration depth) was embedded in a brain cube (non-fluorescent cube with optical properties of gray matter compiled from [36, 37, 45]) with an edge length of 30 mm. As the simulation was intended to mimic the experimental setup, one surface of the tumor cube was in contact with the excitation/detection fiber (core diameter 200 μm , NA = 0.22). For both excitation wavelengths, the detected fluorescence signals for each tumor size were normalized to the signal of the biggest tumor cube (15 mm edge length). More detailed information on model and parameters used for the simulations is provided in the Supporting Information (Part 1).

2.4 Attenuation through blood layers of well-defined thicknesses

2.4.1 Measurements

In Figure 4, the experimental setting of the blood layer measurements is illustrated, outlining the phantom-part of Figure 3, in this case to determine the attenuation of PpIX fluorescence signals caused by particular blood layers between fiber and fluorescence phantom. The 200 μm fiber was directed onto a 2 μM liquid PpIX phantom, which was filled into one well of a 96-well plate. Blood and water layer systems were alternatively placed on top of the phantom, leaving a small gap of about 2 mm in between. This gap was experimentally necessary to avoid contaminating the layer system with phantom liquid and thus enable unimpaired measurements on reference phantoms (see below) with the identical blood or water layer systems. Additionally, a small gap of about 1 mm was left between the layer system and the distal fiber end to prevent fiber damage. The layer systems were prepared by attaching distance pieces of defined thicknesses on an object slide (1.0 mm thickness), leaving free space in between. A droplet of blood or water (for reference) was then

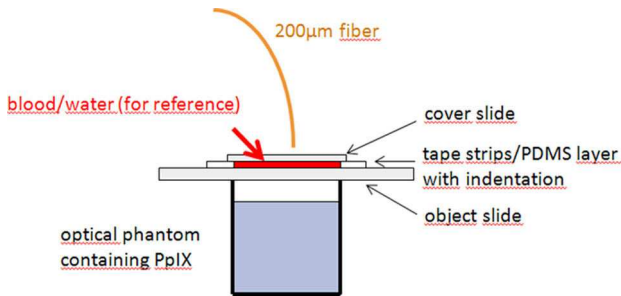


Figure 4 Illustration of blood layer measurements. The 200 μm fiber (NA = 0.22) of the measurement setup (see Figure 3) is used to excite and detect fluorescence in a 2 μM liquid PpIX phantom, which is filled into one well of a 96-well plate. Layer systems consisting of an object slide, spacers (tape strips or PDMS layers with indentation), a liquid droplet (blood or water) and a cover slide are placed on top of the liquid phantom.

dripped into this space and spread by putting a cover slide (0.17 mm thickness) on top of it.

For $\lambda_{\text{exc}} = 405 \text{ nm}$, layers of 10 μm , 20 μm and 50 μm were applied, for $\lambda_{\text{exc}} = 633 \text{ nm}$ 10 μm , 20 μm , 50 μm , 100 μm , 150 μm , 200 μm and 400 μm . Several layers of normal (thickness: 50 $\mu\text{m} \pm 5 \mu\text{m}$) and double adhesive (thickness: 200 $\mu\text{m} \pm 20 \mu\text{m}$) tape strips were used to create distances of 50 μm and more between the object slide and the cover slide. The tape strip thicknesses were measured with a Vernier caliper, putting at least five layers on top of each other to improve precision. To provide smaller distances, transparent polydimethylsiloxane (PDMS) layers were fabricated using SU-8 negative photoresist coated on silicon wafers. The thicknesses of the PDMS layers were 10.0 $\mu\text{m} \pm 0.1 \mu\text{m}$ and 18.7 $\mu\text{m} \pm 0.1 \mu\text{m}$ as was measured on the silicon wafers with a stylus profilometer (Veeco Dektak 6M, Veeco Instruments Inc., Plainview, NY, USA). Since the preparation of the final blood and water layer systems could not be performed with equivalent precision, layer thicknesses with larger uncertainties, i.e. 10 $\mu\text{m} \pm 5 \mu\text{m}$ and 20 $\mu\text{m} \pm 5 \mu\text{m}$, were assumed.

The fluorescence signals were obtained letting both excitation and emission light pass through the blood layers. These signals, corrected for background fluorescence by using reference phantoms as described in Section 2.3.1, were then divided by the likewise corrected signals obtained when replacing the blood layers with water layers of the same thickness. These water signals were acquired under identical conditions, especially the distance between fiber end and phantom surface was kept constant. The hereby obtained relative intensities were finally evaluated at the peak wavelengths of the emission spectra as described in Section 2.3.1. This measurement and evaluation procedure was repeated three times for each layer and excitation wavelength. For

each thickness and excitation wavelength, three sets of blood/water layers were prepared and measured.

It has to be stated that the details of the excitation and fluorescence capture geometry realized here have an effect on the absolute fluorescence signals. The excitation beam, for instance, is expanded due to the presence of object and cover slides as well as the mentioned air gaps. In these experiments, however, only the ratio of the fluorescence signals measured through blood versus through water was of interest and for each single measurement pair (including blood and water layers of the same thickness), a constant excitation and fluorescence capture geometry could be assured. Thus, the effect of the experimental geometry on the results can be neglected.

2.4.2 Ray tracing simulations

To affirm the results of these blood layer measurements, ray tracing simulations reproducing the experimental settings described in Section 2.4.1 were performed using the Monte Carlo-based software TracePro (Lambda Research Corporation, Littleton, MA, USA). More detailed information on model and parameters used for the simulations is provided in the Supporting Information (Part 2).

2.5 Contact measurements on agar phantoms

With these experiments, minor bleedings during stereotactic biopsy should be mimicked. The blood layer thickness expectable when driving the needle

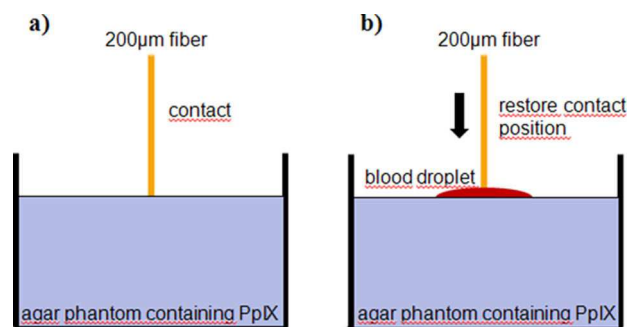


Figure 5 Illustration of contact measurements on agar phantoms. (a) A 200 μm fiber (NA = 0.22) with SMA connector at the distal end is in contact with the agar phantom (reference measurement). (b) After putting a blood droplet on the phantom, the contact position of the fiber is restored and the signal reduction as compared to the reference measurement is recorded.

forward through the blood until getting in touch with the tissue was determined with contact measurements on agar phantoms (PpIX concentration: 5 μM) as depicted in Figure 5.

A 200 μm fiber (NA = 0.22) with SMA connector at the distal end, installed at the measurement setup described in Section 2.2, was used to simulate the blood extrusion of a biopsy needle with one integrated excitation and detection fiber when getting in contact with brain tissue. For this purpose, the distal fiber tip was attached to a LabVIEW-controlled stepping motor. Exact contact positions could be identified exploiting the jump in the remission or fluorescence signal that arose when the fiber tip touched the phantom and refraction index mismatches (glass – air and air – phantom) disappeared. By means of the stepping motor, these positions could be reproduced with micrometer precision.

After identifying the vertical contact position, the fiber was driven upwards and a blood droplet (about 50 μl) was dripped onto the phantom surface. Then the contact position of the fiber was restored. The detectable signal through blood (corrected for background fluorescence as described in Section 2.3.1) was divided by the corrected signal without blood and evaluated at the peak emission wavelength as described in Section 2.3.1. This measurement scheme was performed five times for each excitation wavelength with moving the phantom a few millimeters horizontally after each measurement to account for photobleaching.

3. Results and discussion

3.1 PpIX detection limits

3.1.1 Measurements on semi-infinite phantoms

Exemplary PpIX fluorescence spectra for both excitation wavelengths are displayed in Figure 6a. Note that even for the lowest of the used PpIX concentrations, spectra with reasonable signal quality could be recorded. In Figure 6b, the peak intensities of all PpIX spectra divided by the excitation power are plotted against the concentration.

The results of the linear regression (R^2 values of 1.000 and 0.994 for $\lambda_{\text{exc}} = 405 \text{ nm}$ and $\lambda_{\text{exc}} = 633 \text{ nm}$, respectively) show that the assumed proportionality between fluorophore concentration and fluorescence signal is valid in the investigated concentration range. Consequently, a signal intensity per concentration and excitation power can be calculated. Defining the lowest detectable signal as the threefold of the background noise level, which is about one count per millisecond, this leads to detection limits of 4.4 nM ($\lambda_{\text{exc}} = 405 \text{ nm}$, 0.9 mW excitation power) and 38 nM ($\lambda_{\text{exc}} = 633 \text{ nm}$, 5.5 mW excitation power). Considering the respective excitation power, these numbers may be converted to detection limits in terms of fluorophore concentration times the excitation power, which indicate the lowest detectable con-

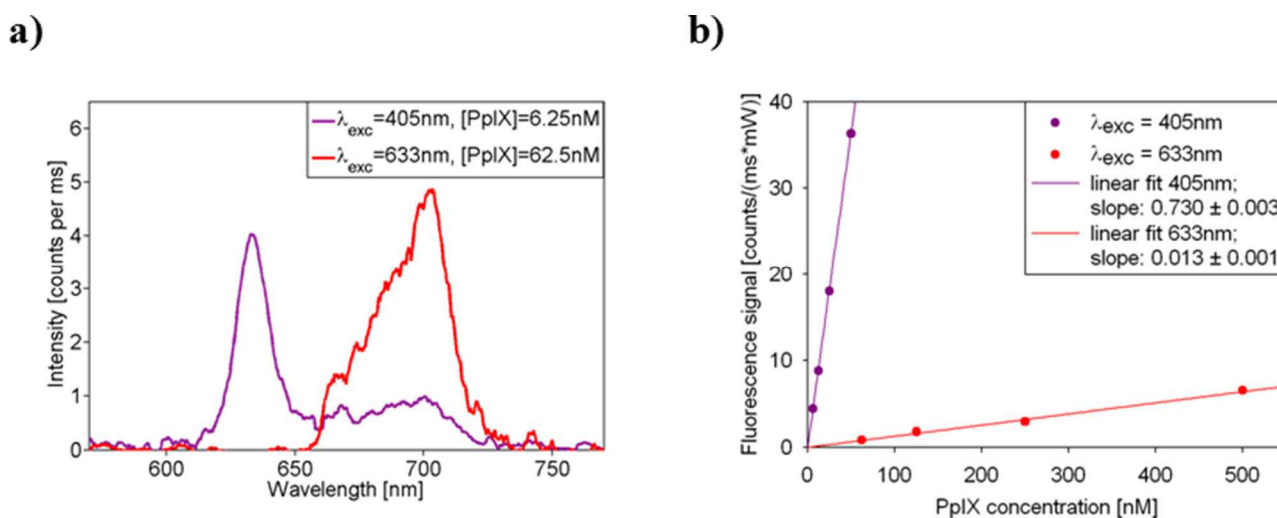


Figure 6 (a) Exemplary averaged and smoothed PpIX fluorescence spectra ($n = 4$) for 405 nm (0.9 mW excitation power) and 633 nm (5.5 mW excitation power) excitation. For both excitation wavelengths, the spectra with lowest PpIX concentration are shown. (b) Fluorescence intensity per excitation power as a function of the PpIX concentration. For both excitation wavelengths, a linear relation was observed. The slopes are given in counts/(ms \times mW \times nM).

centrations at a given laser power. These detection limits were determined as $4.0 \text{ nM} \cdot \text{mW}$ for $\lambda_{\text{exc}} = 405 \text{ nm}$ and $200 \text{ nM} \cdot \text{mW}$ for $\lambda_{\text{exc}} = 633 \text{ nm}$.

Considering only the fluorescence properties of pure PpIX, which were extracted from measurements in a clear PpIX/DMSO solution (see Supplementary Table S2), the fluorescence signal excited at $\lambda_{\text{exc}} = 633 \text{ nm}$ and detected at $\lambda_{\text{em}} = 702 \text{ nm}$ should be about 100 times weaker than for $\lambda_{\text{exc}} = 405 \text{ nm}$ and $\lambda_{\text{em}} = 633 \text{ nm}$. Due to the different optical properties of brain tumor tissue for these wavelengths, however, this factor reduces to 50 in case of the brain tissue equivalent optical phantoms investigated here.

The potential impact of photobleaching had been tested in two ways. First it was verified that the total signal loss due to photobleaching during the selected integration times (between 15 ms and 500 ms) was in any case below 10%. Repeated measurements were performed on different sites of the phantom. To estimate the effect of photobleaching in the clinical situation, photobleaching measurements on excised GBM tissue after 5-ALA administration were conducted with the experimental setup used in this study. The induced photobleaching lifetimes τ (time periods after which the fluorescence signal has decreased to $1/e$) were determined as $\tau_{405} = (9 \pm 2) \text{ s}$ and $\tau_{633} = (21 \pm 2) \text{ s}$ for $\lambda_{\text{exc}} = 405 \text{ nm}$ and $\lambda_{\text{exc}} = 633 \text{ nm}$, respectively. Assuming that the actual measurement period (when the fiber is in contact with the tumor tissue) does not have to be longer than 1 s to get a sufficient signal, photobleaching should not be a limiting factor, even if needle approach and repeated light exposure are considered as well.

3.1.2 Ray tracing simulations with variable tumor size

In Figure 7a, the dependency of the detected PpIX signal on the tumor size is shown. For both excitation wavelengths, the fluorescence intensity increases with rising tumor size up to a saturation level, thereby following a sigmoidal curve in a semi-logarithmic plot. In the investigated tumor size range, the relative intensity (as compared to infinitely large tumors) is always higher for $\lambda_{\text{exc}} = 405 \text{ nm}$ than for $\lambda_{\text{exc}} = 633 \text{ nm}$ with a maximum ratio of about 2 for infinitesimally small tumors (see Figure 7b). The edge lengths of the tumor cube at which the intensity has reached 95% of the maximum (referred to as critical length scales) are 0.55 mm and 1.8 mm for $\lambda_{\text{exc}} = 405 \text{ nm}$ and $\lambda_{\text{exc}} = 633 \text{ nm}$, respectively.

Above these thresholds, the detected PpIX signal does not depend on the tumor size and the detection limits presented in Section 3.1.1 are valid. However, for smaller tumor parts below the critical length scales, the detected intensity per PpIX concentration diminishes, leading to higher detection limits than determined above. This intensity loss is stronger for $\lambda_{\text{exc}} = 633 \text{ nm}$ than for $\lambda_{\text{exc}} = 405 \text{ nm}$, which can be explained by the higher penetration depth of red as compared to violet light. According to the presented simulations, the sensitivity ratio rises from 50 to 100 for infinitesimally small tumors where the mean free path length of the excitation or fluorescence light is large compared to the tumor size. This increase is in accordance with the determined fluorescence properties of pure PpIX (see Section 3.1.1 and Supplementary Table S2).

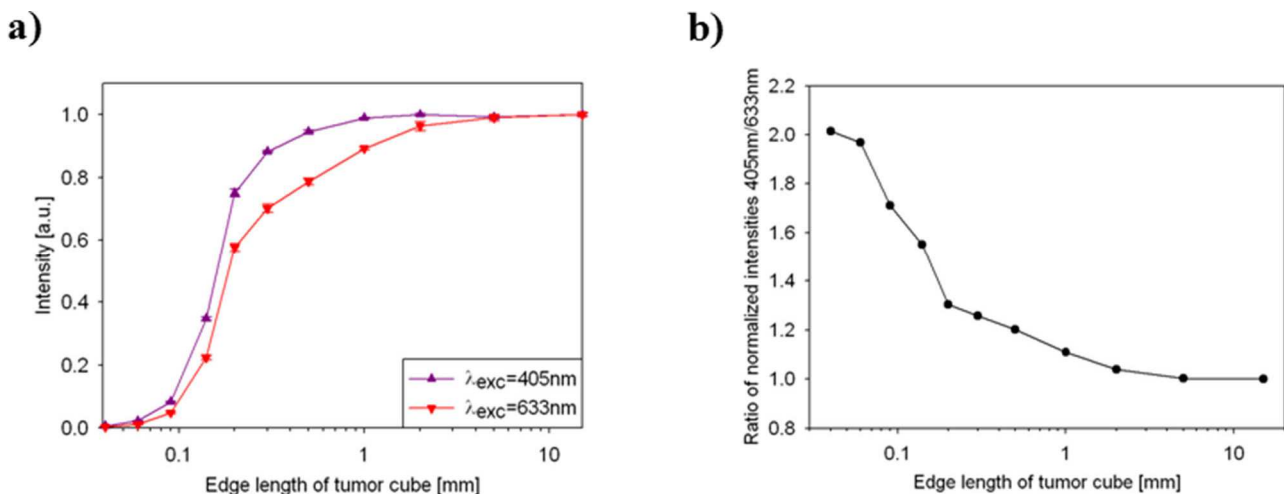


Figure 7 (a) Simulated fluorescence intensity as a function of tumor cube edge length. For each excitation wavelength, the intensities were normalized to the signal of the tumor cube with the largest edge length (15 mm). Error bars indicate standard errors of the means obtained via three simulations with different random number seeds. (b) Ratio of normalized intensities 405 nm/633 nm.

Considering only tumor parts larger than 1 mm^3 , which is the biopsy volume usually required for molecular diagnosis, detection limits stay constant for $\lambda_{\text{exc}} = 405 \text{ nm}$ and are only weakly increased for $\lambda_{\text{exc}} = 633 \text{ nm}$: Given a tumor size of 1 mm^3 where the relative fluorescence intensities are 0.99 and 0.89, the limits are $4.0 \text{ nM} \cdot \text{mW}$ and $220 \text{ nM} \cdot \text{mW}$ for $\lambda_{\text{exc}} = 405 \text{ nm}$ and $\lambda_{\text{exc}} = 633 \text{ nm}$, respectively. Sampling of smaller tumor parts would be subject to a declined sensitivity, but is not desirable because the specimen would necessarily contain both tumor and healthy tissue. Apart from stereotactic biopsies where the planned target is usually the vital margin of the bulk tumor, these results are also particularly relevant for open brain surgery – fluorescence-guided resection and surgical biopsies – where it is fundamental to achieve a total resection and to gain histopathological information on different tumor parts.

3.2 Attenuation through blood layers of well-defined thicknesses

The attenuation of PpIX signals caused by blood layers between fiber and phantom is extremely different for the two excitation wavelengths. This is illustrated in Figure 8a where the spectra recorded through $10 \mu\text{m}$ layers of blood and water are shown exemplarily. In Figure 8b, all measured relative in-

tensities, plotted against the blood layer thickness, are compared with the results obtained from ray tracing simulations.

While for $\lambda_{\text{exc}} = 405 \text{ nm}$, the fluorescence is already blocked by a $50 \mu\text{m}$ blood layer, even layers of $400 \mu\text{m}$ still allow relative signal amplitudes (blood versus water) of about 5% for $\lambda_{\text{exc}} = 633 \text{ nm}$. The intensities detected through thinner blood layers drop exponentially with the layer thickness. It can be seen that experimental and simulated results are in good accordance. Considering the uncertainties given by standard errors of the mean ($n = 3$), only two outliers can be identified, one of which (at $10 \mu\text{m}$ for $\lambda_{\text{exc}} = 405 \text{ nm}$) is located in a range of very steep decrease. The simulation results for $\lambda_{\text{exc}} = 633 \text{ nm}$ could be best described with a double-exponential fit

$$I_r = a \cdot \exp(-b \cdot d) + (1 - a) \cdot \exp(-c \cdot d) \quad (1)$$

where I_r and d denote the relative peak intensity and the blood layer thickness, respectively, and $a = 0.59 \pm 0.20$, $b = (17.8 \pm 5.1) \text{ mm}^{-1}$ and $c = (5.2 \pm 1.8) \text{ mm}^{-1}$ are the fit parameters. The indicated uncertainties denote standard errors. A single-exponential fit

$$I_r = \exp(-b \cdot d) \quad (2)$$

with $b = (10.5 \pm 0.7) \text{ mm}^{-1}$ was also acceptable for thinner layers ($d < 200 \mu\text{m}$), but overestimated the sig-

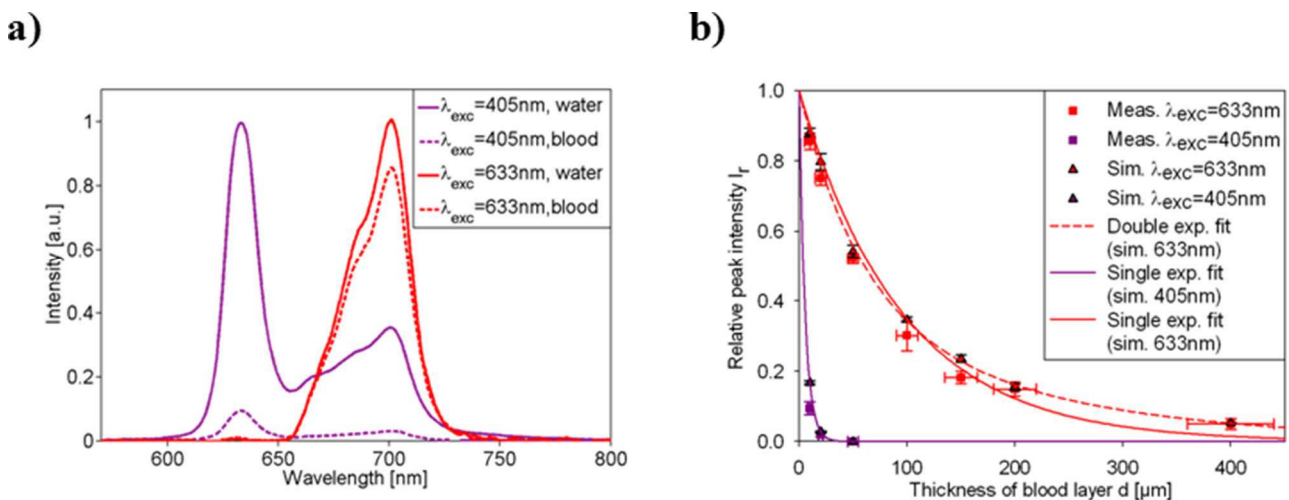


Figure 8 (a) Averaged and smoothed PpIX fluorescence spectra ($n = 3$) detected through $10 \mu\text{m}$ layers of water and blood, respectively. For each excitation wavelength, the spectra were normalized to the peak intensity of the spectrum recorded through water. The layer systems were freshly assembled for each measurement. (b) Relative peak intensity as a function of the blood layer thickness. Measurement (meas.) and simulation (sim.) results are shown for both excitation wavelengths. Vertical error bars indicate standard errors of the means obtained via three independent measurements with freshly assembled layer systems or three simulations with different random number seeds, respectively. Horizontal error bars reflect the thickness uncertainties of the layer systems. Single and double ($\lambda_{\text{exc}} = 633 \text{ nm}$) or only single ($\lambda_{\text{exc}} = 405 \text{ nm}$) exponential functions were fit to the simulation results.

nal attenuation through thicker layers ($d > 200 \mu\text{m}$). For $\lambda_{\text{exc}} = 405 \text{ nm}$, only three sampling points were given so that only a single-exponential fit as in Eq. (2) was possible, yielding $b = (179 \pm 3) \text{ mm}^{-1}$. A theoretical interpretation of the single-exponential fit parameter b can be found in the Supporting Information (Part 3).

3.3 Contact measurements on agar phantoms

The relative PpIX peak intensities detected after immersing the distal fiber end in the blood droplet until getting in contact with the agar phantom surface were quite reproducible: Averaging of five single measurements for each excitation wavelength performed at different positions of the phantom yielded values of $(0.3 \pm 0.3)\%$ for $\lambda_{\text{exc}} = 405 \text{ nm}$ and $(74.5 \pm 1.5)\%$ for $\lambda_{\text{exc}} = 633 \text{ nm}$, the indicated uncertainties denoting standard errors of the mean. The respective averaged spectra are shown in Figure 9. When driving the fiber even further into the phantom, no signal recovery was visible until 1 mm below the phantom surface.

By means of Eq. (1) ($\lambda_{\text{exc}} = 633 \text{ nm}$) and (2) ($\lambda_{\text{exc}} = 405 \text{ nm}$) and the corresponding fit results, the ratio of the peak intensities with and without blood layer can be converted to thicknesses of $32 \mu\text{m}$ ($\lambda_{\text{exc}} = 405 \text{ nm}$, $\lambda_{\text{em}} = 633 \text{ nm}$) and $24 \mu\text{m}$ ($\lambda_{\text{exc}} = 633 \text{ nm}$, $\lambda_{\text{em}} = 702 \text{ nm}$). Hence, in case of minor bleedings during stereotactic biopsy, fluorescence obscuring blood layers of about $20 \mu\text{m}$ to $40 \mu\text{m}$ should be reckoned with when advancing the biopsy needle until getting in contact with the investigated brain tissue.

4. Conclusion

With regard to their suitability for fiber-based PpIX detection in brain tumor tissue, both examined excitation wavelengths feature notable advantages and drawbacks:

On the one hand, violet excitation at the Soret peak (around 405 nm), which represents the maximum of the PpIX excitation spectrum, allows for a considerably higher sensitivity: Realistic PpIX detection measurements in contact with bulk tumor mimicking phantoms showed an enhancement by a factor of 50 for equal excitation powers as compared to the red excitation at 633 nm (see Figure 6b). For smaller tumor parts, this factor is elevated up to a maximum of 100. This yields not only better signal to noise ratios, but also enables the detection of tumor entities with a fainter fluorescence as for example grade III glioma or peripheral regions of the tumor. Additionally, a broad and characteristic emission spectrum is induced, allowing the extraction of valuable spectral information [46, 47]. Moreover, the use of a 405 nm light source also leads to the excitation of tissue autofluorescence, which could be used as an additional parameter for tissue discrimination [48–50] or serve as reference for the normalization of PpIX signals [27].

On the other hand, red excitation at 633 nm offers an increased tissue penetration, which extenuates the effect of the comparably low fluorescence excitation efficiency of this wavelength, at least for tumors that are thick enough to cover the whole penetration depth. Based on the bulk-tumor detection limit of $200 \text{ nM} \cdot \text{mW}$ for $\lambda_{\text{exc}} = 633 \text{ nm}$ (see Section 3.1.1), vital GBM tissue, which typically exhibits PpIX concentrations of a few μM after 5-ALA administra-

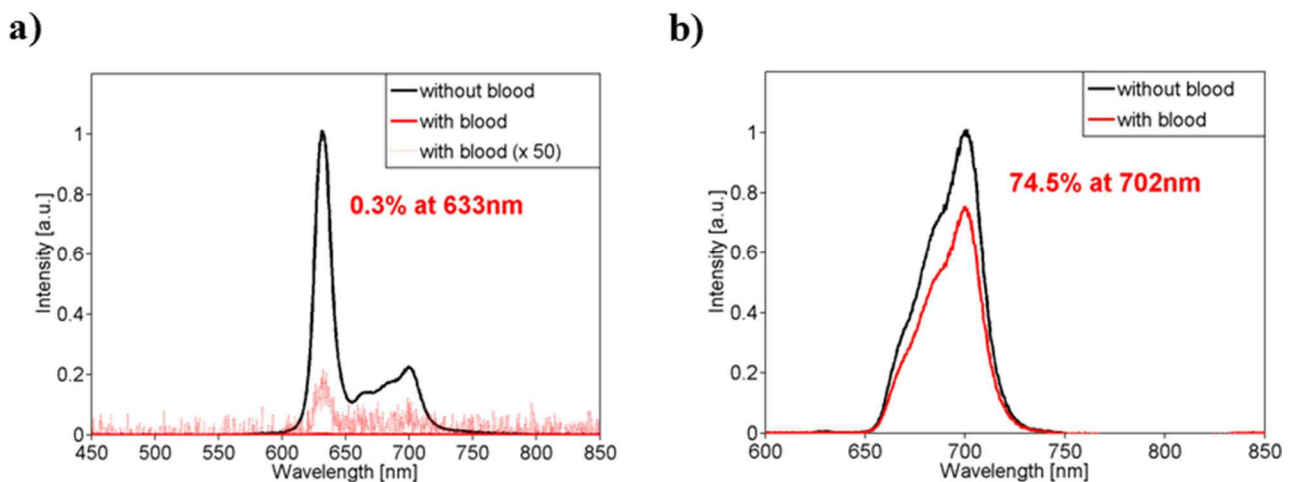


Figure 9 Averaged and smoothed PpIX fluorescence spectra ($n = 5$) detected in contact with the agar surface before and after dripping a blood droplet onto the phantom. (a) Excitation at 405 nm . (b) Excitation at 633 nm .

tion at 20 mg per kg body weight [24, 33, 51], should well be detectable with a 200 μm diameter fiber (NA = 0.22) in contact with the tissue. As shown in Section 3.1.2, the detection limit for smaller tumor parts that are still big enough to be sampled during stereotactic biopsy is only slightly increased. As a consequence, the currently approved and conventionally applied 5-ALA dose (20 mg per kg body weight) is assumed to be sufficient also for 633-nm-excited PpIX fluorescence; higher doses with a higher risk of producing side effects such as skin photosensitivity or nausea and vomiting [52] are not necessary.

Another advantage of the increased penetration depth of 633 nm (1.3 mm instead of 0.21 mm for 405 nm) is that for conventional biopsy needles, a better congruence between mechanical (usually a few mm^3) and optically probed volume can be achieved. For example, a small layer containing PpIX, which is on top of normal brain tissue, would deliver a strong signal using 405 nm excitation. Thus, a biopsy would possibly be taken at this site, which would largely consist of normal tissue, though. In contrast, the risk that tumor tissue which is located outside the needle's coverage and excited with 633 nm delivers a signal amplitude that induces the surgeon to take a biopsy is rather low.

Finally, the results of Sections 3.2 and 3.3 clearly show that 633 nm excitation is unambiguously superior in case of blood-covered tumor tissue. Even though the actual numbers depend on the exact excitation and detection geometry, the qualitative result is generally valid and entails important consequences as when inserting a needle into human brain, minor blood vessel ruptures followed by blood moistening of the analyzed tissue can never be completely prevented. The presented contact measurements on agar phantoms demonstrate that one has to reckon with remaining blood layers between 20 μm and 40 μm even when the biopsy needle is driven through the blood until the distal fiber end is in contact with the tissue. This refers to the range where the difference in relative signal magnitudes between $\lambda_{\text{exc}} = 405$ nm and $\lambda_{\text{exc}} = 633$ nm is particularly large (see Figure 8b) and the risk of not detecting blood-covered tumor tissue is considerably high for $\lambda_{\text{exc}} = 405$ nm. Beyond stereotactic biopsies, these results on the practical implications of blood interference are also very relevant for fluorescence guidance in open brain surgery, e.g. when examining the resection cavity with a fiber optical probe as described in [27, 28].

The results of this preclinical experimental evaluation indicate that $\lambda_{\text{exc}} = 633$ nm seems to be the wavelength of choice for PpIX detection during stereotactic biopsies of high-grade gliomas. Despite the reduced sensitivity as compared to $\lambda_{\text{exc}} = 405$ nm, at least grade IV glioma (GBM) should well be de-

tectable with single-fiber probes, and in case of unavoidable bleeding, $\lambda_{\text{exc}} = 633$ nm seems to be significantly better suited. Nevertheless, devices where both excitation wavelengths are used simultaneously might be of even greater benefit because the advantages of both excitation modes could be combined. Finally, it has to be emphasized that the presented results, especially the potentials of the red excitation in case of blood interference, are not only interesting for the stereotactic biopsy procedure, but also for other applications such as photodynamic therapy or fluorescence-guided resection.

Acknowledgements Funding support by the German Ministry of Education and Research (BMBF) under grant number 01DJ14012B, "Gliotax", is gratefully acknowledged.

References

- [1] M. L. Goodenberger and R. B. Jenkins, *Cancer Genet* **205**(12), 613–621 (2012).
- [2] H. Ohgaki, *Methods Mol Biol* **472**, 323–342 (2009).
- [3] M. L. Siker, M. Wang, K. Porter, D. F. Nelson, W. J. Curran, J. M. Michalski, L. Souhami, A. Chakravarti, W. K. Yung, J. Delrowe, C. T. Coughlin, and M. P. Mehta, *J Neurooncol* **104**(1), 351–356 (2011).
- [4] A. Claes, A. J. Idema, and P. Wesseling, *Acta Neuro-pathol* **114**(5), 443–458 (2007).
- [5] J. Drappatz, A. D. Norden, and P. Y. Wen, *Expert Rev Neurother* **9**(4), 519–534 (2009).
- [6] M. Weller, R. Stupp, G. Reifenberger, A. A. Brandes, M. J. van den Bent, W. Wick, and M. E. Hegi, *Nat Rev Neurol* **6**(1), 39–51 (2010).
- [7] S. Eigenbrod, R. Trabold, D. Brucker, C. Erös, R. Egensperger, C. La Fougere, W. Göbel, A. Rühm, H. A. Kretzschmar, J. C. Tonn, J. Herms, A. Giese, and F. W. Kreth, *Acta Neurochir (Wien)* **156**(8), 1427–1440 (2014).
- [8] Y. T. Oh, H. J. Cho, J. Kim, J. H. Lee, K. Rho, Y. J. Seo, Y. S. Choi, H. J. Jung, H. S. Song, D. S. Kong, H. J. Seol, J. I. Lee, Y. Yoon, S. Kim, D. H. Nam, and K. M. Joo, *PLoS One* **9**(8), e103327 (2014).
- [9] J. H. Chiang, W. S. Cheng, L. Hood, and Q. Tian, *OMICS* **18**(5), 310–323 (2014).
- [10] A. A. Shakal and E. A. Mokbel, *J Neurol Surg A Cent Eur Neurosurg* **75**(3), 177–182 (2014).
- [11] D. Kondziolka, A. D. Firlik, and L. D. Lunsford, *Neurol Clin* **16**(1), 35–54 (1998).
- [12] W. Göbel, D. Brucker, Y. Kienast, A. Johansson, G. Kniebühler, A. Rühm, S. Eigenbrod, S. Fischer, M. Goetz, F. W. Kreth, A. Ehrhardt, H. Stepp, K. M. Irion, and J. Herms, *Opt Express* **20**(24), 26117–26126 (2012).
- [13] D. Jain, M. C. Sharma, C. Sarkar, P. Deb, D. Gupta, and A. K. Mahapatra, *Brain Tumor Pathol* **23**(2), 71–75 (2006).

- [14] D. Jain, M. C. Sharma, C. Sarkar, D. Gupta, M. Singh, and A. K. Mahapatra, *Neurol India* **54**(4), 394–398 (2006).
- [15] A. O. Heper, E. Erden, A. Savas, K. Ceyhan, I. Erden, S. Akyar, and Y. Kanpolat, *Surg Neurol* **64**(2), S82–S88 (2005).
- [16] C. M. Owen and M. E. Linskey, *J Neurooncol* **93**(1), 139–149 (2009).
- [17] G. Tsermoulas, N. Mukerji, A. J. Borah, P. Mitchell, and N. Ross, *Br J Neurosurg* **27**(2), 207–211 (2013).
- [18] G. F. Woodworth, M. J. McGirt, A. Samdani, I. Garonzik, A. Olivi, and J. D. Weingart, *J Neurosurg* **104**(2), 233–237 (2006).
- [19] R. Dammers, I. K. Haitzma, J. W. Schouten, J. M. Kros, C. J. Avezaat, and A. J. Vincent, *Acta Neurochir (Wien)* **150**(1), 23–29 (2008).
- [20] G. K. Zoeller, R. J. Benveniste, H. Landy, J. J. Morcos, and J. Jagid, *Stereotact Funct Neurosurg* **87**(3), 174–181 (2009).
- [21] S. Moriuchi, K. Yamada, M. Dehara, Y. Teramoto, T. Soda, M. Imakita, and M. Taneda, *J Neurosurg* **115**(2), 278–280 (2011).
- [22] W. Stummer, A. Novotny, H. Stepp, C. Goetz, K. Bise, and H. J. Reulen, *J Neurosurg* **93**(6), 1003–1013 (2000).
- [23] W. Stummer, U. Pichlmeier, T. Meinel, O. D. Wiesler, F. Zanella, and H. J. Reulen, *Lancet Oncol* **7**(5), 392–401 (2006).
- [24] A. Johansson, G. Palte, O. Schnell, J. C. Tonn, J. Herms, and H. Stepp, *Photochem Photobiol* **86**(6), 1373–1378 (2010).
- [25] H. Stepp and W. Stummer, in: S. J. Madsen (ed.), *Optical Methods and Instrumentation in Brain Imaging and Therapy*, (Springer Science+Business Media, New York, 2013), pp. 173–205.
- [26] S. Zhao, J. Wu, C. Wang, H. Liu, X. Dong, C. Shi, Y. Liu, L. Teng, D. Han, X. Chen, G. Yang, L. Wang, C. Shen, and H. Li, *PLoS One* **8**(5), e63682 (2013).
- [27] N. Haj-Hosseini, J. Richter, S. Andersson-Engels, and K. Wardell, *Lasers Surg Med* **42**(1), 9–14 (2010).
- [28] P. A. Valdes, F. Leblond, A. Kim, B. T. Harris, B. C. Wilson, X. Fan, T. D. Tosteson, A. Hartov, S. Ji, K. Erkmén, N. E. Simmons, K. D. Paulsen, and D. W. Roberts, *J Neurosurg* **115**(1), 11–17 (2011).
- [29] G. Widhalm, G. Minchev, A. Woehrer, M. Preusser, B. Kiesel, J. Furtner, A. Mert, A. Di Ieva, B. Tomaček, D. Prayer, C. Marosi, J. A. Hainfellner, E. Knosp, and S. Wolfsberger, *Neurosurg Rev* **35**(3), 381–391 (2012).
- [30] G. von Campe, M. Moschopoulos, and M. Hefti, *Acta Neurochir (Wien)* **154**(4), 585–588 (2012).
- [31] S. Marbacher, E. Klinger, L. Schwyzer, I. Fischer, E. Nevzati, M. Diepers, U. Roelcke, A. R. Fathi, D. Coluccia, and J. Fandino, *Neurosurg Focus* **36**(2), E10 (2014).
- [32] D. W. Roberts, P. A. Valdes, B. T. Harris, K. M. Fontaine, A. Hartov, X. Fan, S. Ji, S. S. Lollis, B. W. Pogue, F. Leblond, T. D. Tosteson, B. C. Wilson, and K. D. Paulsen, *J Neurosurg* **114**(3), 595–603 (2011).
- [33] M. Loshchenov, P. Zelenkov, A. Potapov, S. Goryajnov, and A. Borodkin, *Photonics and Lasers in Medicine* **3**(2), 159–170 (2013).
- [34] N. Haj-Hosseini, S. Lowndes, G. Salerud, and K. Wardell, in: *Proc. SPIE, Photonic Therapeutics and Diagnostics VII*, 2011, 78833R.
- [35] A. Johansson, F. Faber, G. Kniebühler, H. Stepp, R. Sroka, R. Egensperger, W. Beyer, and F. W. Kreth, *Lasers Surg Med* **45**(4), 225–234 (2013).
- [36] S. C. Gebhart, W. C. Lin, and A. Mahadevan-Jansen, *Phys Med Biol* **51**(8), 2011–2027 (2006).
- [37] A. N. Yaroslavsky, P. C. Schulze, I. V. Yaroslavsky, R. Schober, F. Ulrich, and H. J. Schwarzmaier, *Phys Med Biol* **47**(12), 2059–2073 (2002).
- [38] A. Pitzschke, B. Lovisa, O. Seydoux, M. Zellweger, M. Pfeleiderer, Y. Tardy, and G. Wagnières, *Phys Med Biol* **60**(7), 2921–2937 (2015).
- [39] A. Pitzschke, B. Lovisa, O. Seydoux, M. Haenggi, M. F. Oertel, M. Zellweger, Y. Tardy, and G. Wagnières, *J Biomed Opt* **20**(2), 25006 (2015).
- [40] R. Michels, F. Foschum, and A. Kienle, *Opt Express* **16**(8), 5907–5925 (2008).
- [41] R. Cubeddu, A. Pifferi, P. Taroni, A. Torricelli, and G. Valentini, *Phys Med Biol* **42**(10), 1971–1979 (1997).
- [42] Z. J. Chen, G. T. Gillies, W. C. Broaddus, S. S. Prabh, H. Fillmore, R. M. Mitchell, F. D. Corwin, and P. P. Fatouros, *J Neurosurg* **101**(2), 314–322 (2004).
- [43] H. H. Ginary, K. Wong, and K. Lai, *Cornell University* (2007).
- [44] N. Haj-Hosseini, B. Kistler, and K. Wårdell, in: *Proc. SPIE, Design and Performance Validation of Phantoms Used in Conjunction with Optical Measurement of Tissue VI*, 2014, 894505.
- [45] V. Tuchin, *Tissue Optics – Light Scattering Methods and Instruments for Medical Diagnosis* (SPIE, Bellingham, Washington, USA, 2015), pp. 247–294.
- [46] B. Montcel, L. Mahieu-Williams, X. Armoiry, D. Meyronet, and J. Guyotat, *Biomed Opt Express* **4**(4), 548–558 (2013).
- [47] T. Ando, E. Kobayashi, H. Liao, T. Maruyama, Y. Muragaki, H. Iseki, O. Kubo, and I. Sakuma, *Brain Tumor Pathol* **28**(1), 43–51 (2011).
- [48] Y. G. Chung, J. A. Schwartz, C. M. Gardner, R. E. Sawaya, and S. L. Jacques, *J Korean Med Sci* **12**(2), 135–142 (1997).
- [49] W. H. Yong, P. V. Butte, B. K. Pikul, J. A. Jo, Q. Fang, T. Papaioannou, K. Black, and L. Marcu, *Front Biosci* **11**, 1255–1263 (2006).
- [50] A. C. Croce, S. Fiorani, D. Locatelli, R. Nano, M. Ceroni, F. Tancioni, E. Giombelli, E. Benericetti, and G. Bottiroli, *Photochem Photobiol* **77**(3), 309–318 (2003).
- [51] H. Stepp, W. Beyer, D. Brucker, A. Ehrhardt, S. Fischer, W. Göbel, M. Goetz, B. Günther, G. Hennig, J. Herms, K.-M. Irion, A. Johansson, Y. Kienast, G. Kniebühler, P. Li, A. Rühm, and S. Sandner, in: *Proc. SPIE, Photonic Therapeutics and Diagnostics VIII*, 2012, 82074H.
- [52] R. Ackroyd, N. Brown, D. Vernon, D. Roberts, T. Stephenson, S. Marcus, C. Stoddard, and M. Reed, *Photochem Photobiol* **70**(4), 656–662 (1999).

SUPPORTING INFORMATION FOR

405 nm versus 633 nm for protoporphyrin IX excitation in fluorescence-guided stereotactic biopsy of brain tumors

Niklas A. Markwardt^a, Neda Haj-Hosseini^b, Bastian Hollnburger^a, Herbert Stepp^a, Petr Zelenkov^c,
Adrian Rühm^a

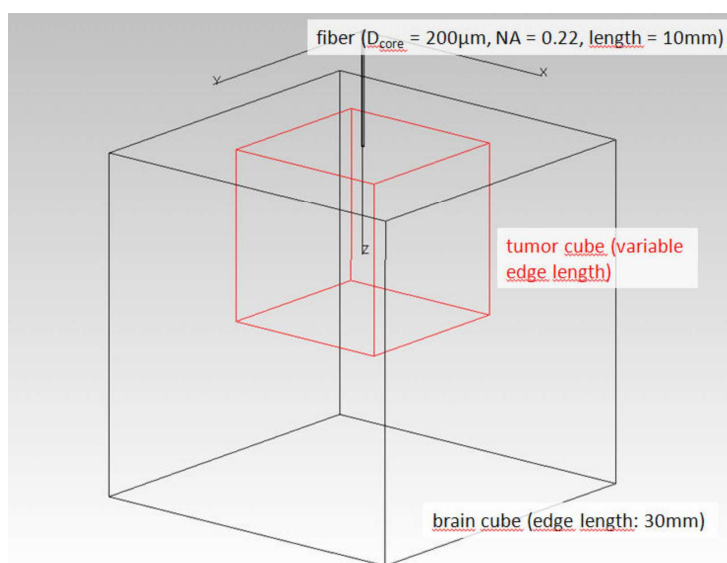
^aLaser-Forschungslabor, LIFE-Zentrum, Klinikum der Universität München, Munich, Germany

^bDepartment of Biomedical Engineering, Linköping University, Linköping, Sweden

^cBurdenko Neurosurgery Institute, Moscow, Russia

Part 1: Ray tracing simulations of PpIX detection for varying tumor size

To analyze the effect of the tumor size on the detected PpIX signal – and thus on the detection limits –, ray tracing simulations for the three wavelengths 405 nm (excitation), 633 nm (excitation and emission) and 702 nm (emission) were performed using the Monte Carlo-based software TracePro (Lambda Research Corporation, Littleton, MA, USA). The applied model is illustrated in Supplementary Figure S1.



Supplementary Figure S1 Simulation model used to analyze the effect of the tumor size on the detected PpIX signal. A fluorescent tumor cube with varying edge length between 0.04 mm and (as shown here) 15 mm is embedded in a non-fluorescent brain cube. The tumor cube is in contact with the lower end of the excitation and detection fiber.

The model basically consisted of three parts: a non-fluorescent brain cube with an edge length of 30 mm, a fluorescent tumor cube with variable edge length, which was embedded into the brain cube, and a fiber. In the x-y-plane, the tumor cube was centrally arranged within the brain cube; in z-direction, the tumor cube was bound to the upper surface of the brain cube (at $z = 10$ mm). The fiber, composed of core, cladding and coating, enclosed the z-axis and its lower end was in contact with the tumor cube. A circular light source with 10^5 emitted rays restricted to a cone with a half-angle of 12.7° (corresponding to a numerical aperture of 0.22) was positioned in the fiber core at $z = 0.5$ mm. The upper surface of the fiber core ($z = 0$) served as detector.

For each tumor cube edge length and excitation wavelength, three simulations with different random number seeds were performed. To realize tumor cubes with different edge lengths, a macro was written that inserted the tumor cube with the required edge length into the predefined model containing only fiber and brain cube. Edge lengths between 0.04 mm and 15 mm were used. As this maximum value was much larger than the fiber core diameter (200 μm) and the penetration depths of all considered wavelengths (0.21 mm, 1.3 mm and 1.6 mm for 405 nm, 633 nm and 702 nm, respectively), it could be regarded as infinitely large. The same applied to the brain cube exhibiting an edge length of 30 mm. Hence, the excitation and detection geometry for the largest tumor cube could be identified with the measurements on semi-infinite phantoms described in the main article, Section 2.3.1. For both excitation wavelengths, the detected fluorescence signal for each tumor size was thus normalized to the signal of the tumor cube with 15 mm edge length.

Supplementary Table S1 Optical parameters used for the tumor size simulations.

Parameter	n	μ_a [mm^{-1}]			μ_s' [mm^{-1}]		
		405	633	702	405	633	702
Wavelength [nm]	500	405	633	702	405	633	702
Core	1.46	-	-	-	-	-	-
Cladding	1.44	-	-	-	-	-	-
Coating	1.66	-	-	-	-	-	-
Tumor cube	1.37	1.4	0.09	0.07	3.9	2.2	1.8
Brain cube	1.37	0.6	0.05	0.04	2.0	1.0	0.9

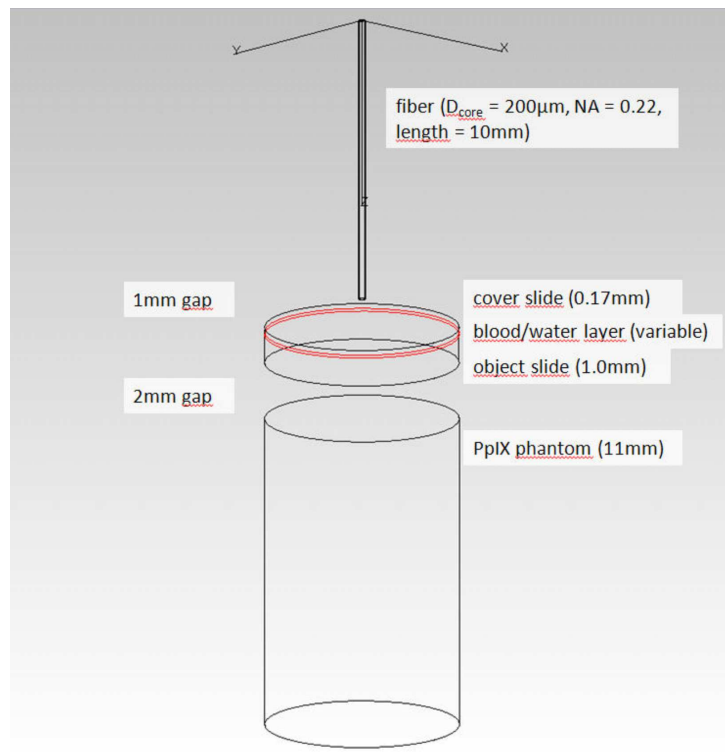
In Supplementary Table S1, the refraction indices (n) and optical properties of the simulation objects are listed. The optical properties of the tumor cube (simulating brain tumor tissue) were taken from Gebhart et al. [1]; the optical properties of the brain cube (simulating gray matter) were compiled from Gebhart et al. [1], Yaroslavsky et al [2] and Tuchin [3]. Fluorescence properties, listed in Supplementary Table S2, were extracted from PpIX measurements in dimethyl sulfoxide (DMSO) performed with commercial fluorescence (FluoroMax-2®, Horiba Jobin Yvon GmbH, Unterhaching, Germany) and absorption (Lambda 40, Perkin Elmer GmbH, Überlingen, Germany) spectrometers.

Supplementary Table S2 Fluorescence properties of PpIX applied to the tumor cube.

Wavelength [nm]	rel. absorption	rel. excitation	rel. emission
405	0.99	0.99	-
633	0.03	0.03	1
702	-	-	0.31
Peak Molar Extinction [$\text{l}/(\text{mole}\cdot\text{cm})$]		1.77e5	
Concentration [μM]		2.0	

Part 2: Ray tracing simulations of light attenuation through blood layers

To affirm the results of the blood layer measurements described in Section 2.4.1, ray tracing simulations for the three wavelengths 405 nm (excitation), 633 nm (excitation and emission) and 702 nm (emission) were performed using the Monte Carlo-based software TracePro (Lambda Research Corporation, Littleton, MA, USA). The applied model, which reflected the geometrical dimensions of the measurements, is illustrated in Supplementary Figure S2.



Supplementary Figure S2 Simulation model used to affirm the results of the blood layer measurements. The object lengths in z direction are indicated. Except the fiber, exhibiting the dimensions of the type UM22-200 (Thorlabs GmbH, Dachau, Germany), all cylindrical objects have a diameter of 6.8 mm corresponding to the wells of a 96-well plate.

The fiber (including core, cladding and coating) was adopted from the model used for the simulations with varying tumor size (see Supporting Information (Part 1)). A circular light source with 10^6 emitted rays restricted to a cone with a half-angle of 12.7° (corresponding to a numerical aperture of 0.22) was positioned in the fiber core at $z = 0.5$ mm. The upper surface of the fiber core ($z = 0$) served as detector. In Supplementary Table S3, the refraction indices (n) and optical properties of the objects are listed.

Supplementary Table S3 Optical parameters used for the blood layer simulations.

Parameter	n	μ_a [mm^{-1}]				μ_s [mm^{-1}]			g		
Wavelength [nm]	500	405	633	702	405	633	702	405	633	702	

Core	1.46	-	-	-	-	-	-	-	-	-
Cladding	1.44	-	-	-	-	-	-	-	-	-
Coating	1.66	-	-	-	-	-	-	-	-	-
Cover slide	1.52	-	-	-	-	-	-	-	-	-
Blood	1.39	140.7	0.275	0.15	41.4	89.0	86.3	0.747	0.979	0.980
Water	1.33	2e-5	3e-4	6e-4	-	-	-	-	-	-
Object slide	1.52	-	-	-	-	-	-	-	-	-
Phantom (exc. 405 nm)	1.33	1.4	0.9	-	26	8.1	-	0.85	0.69	-
Phantom (exc. 633 nm)	1.33	-	0.09	0.015	-	7.1	5.6	-	0.69	0.64

The optical parameters of the phantoms were calculated from the Lipovenös® and ink concentrations used for the liquid phantoms (see main article, Table 1). The absorption coefficients of water were given in the database of the software, scattering in water was neglected; the optical properties of blood are averages of Bosschaart et al. [4] and Prahl [5] for μ_a and of Bosschaart et al. [4] and Tuchin [3] for μ_s and g , respectively. The given data were interpolated to obtain the values at the required wavelengths where necessary. The used fluorescence properties are given in Supplementary Table S2. To simulate all measurement points, a macro was written that inserted water or blood layers of the required thicknesses at the correct position and displaced all objects below correspondingly (see Supplementary Figure S2). For each thickness and excitation wavelength, three simulations with different random number seeds were performed both for water and blood and the average ratio blood/water was calculated.

Part 3: Theoretical interpretation of the single-exponential fit parameter b

Both simulated and experimental results of the light attenuation through blood layers of well-defined thicknesses could be approximately described with a single-exponential fit

$$I_r = \exp(-b \cdot d) \quad (1)$$

where I_r , d and b denote the relative peak intensity (blood versus water), the blood layer thickness and a free fit parameter, respectively. The fit yielded $b = (179 \pm 3) \text{ mm}^{-1}$ for $\lambda_{\text{exc}} = 405 \text{ nm}$ and $b = (10.5 \pm 0.7) \text{ mm}^{-1}$ for $\lambda_{\text{exc}} = 633 \text{ nm}$.

These fit results may be interpreted using a simplified model: If an infinitesimally thin fiber is assumed, which emits a pencil beam with zero divergence, and if multiple scattering is neglected for each transit through the blood layer (excitation and emission), the relative fluorescence intensity (blood versus water) detected with the fiber is determined by the excess absorption (μ_a) and scattering (μ_s) coefficients of blood with respect to water at the considered excitation (exc) and emission (em) wavelengths:

$$I_r = \exp\left[-\left(\mu_{a,\text{exc}} + \mu_{s,\text{exc}} + \mu_{a,\text{em}} + \mu_{s,\text{em}}\right) \cdot d\right] \quad (2)$$

In this model, the light attenuation through blood is systematically overestimated as photons that are scattered away from the initial direction do not contribute to the detected signal anymore. In reality, however, due to the finite thickness and acceptance angle of the fiber, slightly deflected excitation and fluorescence photon paths may still lead to fluorescence

photons which reach the fiber end face within the acceptance angle. Since most scattering events occur into directions near the forward direction ($0.75 < g < 1$), this fact is of special importance. By replacing the scattering coefficients μ_s in Equation (2) with the corresponding reduced scattering coefficients μ_s' , the strong forward scattering in blood is taken into account:

$$I_r = \exp\left[-\left(\mu_{a,\text{exc}} + \mu'_{s,\text{exc}} + \mu_{a,\text{em}} + \mu'_{s,\text{em}}\right) \cdot d\right] \quad (3)$$

With the transition from μ_s to μ_s' , the scattered photons are virtually replaced by two groups of photons: exactly forward scattered (relative strength: $\mu_s \cdot g$) and isotropically scattered (relative strength: $\mu_s' = \mu_s \cdot (1-g)$) photons. Thus, in Equation (3), all forward components of the scattered photons are assumed to contribute to the measured fluorescence signal. This assumption is only correct when considering the forward-directed photon flux, but in the experimental situation discussed here, it actually underestimates the number of photons which are lost due to scattering, to an extent depending on the fiber diameter, its numerical aperture and the geometry of the experimental setup. The actual experimental results may therefore be expected to lie in between those derived from Equations (2) and (3).

Comparing Equations (1) and (2), the fit parameter b can be identified with the sum

$$\mu_{a,\text{exc}} + \mu_{s,\text{exc}} + \mu_{a,\text{em}} + \mu_{s,\text{em}}. \quad (4)$$

Comparing Equations (1) and (3), the fit parameter b can be identified with the sum

$$\mu_{a,\text{exc}} + \mu'_{s,\text{exc}} + \mu_{a,\text{em}} + \mu'_{s,\text{em}}. \quad (5)$$

When inserting the optical properties of blood used for the simulations (see Supplementary Table S3), the sum defined in Equation (4) amounts to 176 mm^{-1} for $\lambda_{\text{exc}} = 633 \text{ nm}$ and to 271 mm^{-1} for $\lambda_{\text{exc}} = 405 \text{ nm}$, the sum defined in Equation (5) to 4.02 mm^{-1} for $\lambda_{\text{exc}} = 633 \text{ nm}$ and to 153 mm^{-1} for $\lambda_{\text{exc}} = 405 \text{ nm}$. A comparison with the single-exponential fitting results for b , i.e. 10.5 mm^{-1} ($\lambda_{\text{exc}} = 633 \text{ nm}$) and 179 mm^{-1} ($\lambda_{\text{exc}} = 405 \text{ nm}$), shows that Equation (2) overestimates the light attenuation through blood by far. Equation (3) provides a much better approximation, even though it slightly underestimates the light attenuation. This is not surprising as even this modified model does still not reflect the experimental excitation and detection geometry correctly. Amongst others, light paths through blood that are longer than the layer thickness d are not considered. However, this model already yields b values of the right order of magnitude and allows interpreting this fit parameter as a sum of absorption and effective scattering coefficients at the considered excitation and emission wavelengths, in which the effective scattering coefficient can be approximated by μ_s' .

SUPPLEMENTARY REFERENCES

- [1] S. C. Gebhart, W. C. Lin, and A. Mahadevan-Jansen, *Phys Med Biol* 51(8), 2011-2027 (2006).
- [2] A. N. Yaroslavsky, P. C. Schulze, I. V. Yaroslavsky, R. Schober, F. Ulrich, and H. J. Schwarzmaier, *Phys Med Biol* 47(12), 2059-2073 (2002).
- [3] V. Tuchin, *Tissue Optics - Light Scattering Methods and Instruments for Medical Diagnosis* (SPIE, Bellingham, Washington, USA, 2015), pp. 247-294.

- [4] N. Bosschaart, G. J. Edelman, M. C. Aalders, T. G. van Leeuwen, and D. J. Faber, *Lasers Med Sci* 29(2), 453-479 (2014).
- [5] S. A. Prahl, *Optical Absorption of Hemoglobin*, tabulated data compiled from various sources (1999), <http://omlc.ogi.edu/spectra/hemoglobin>.

**REMISSION SPECTROMETRY FOR BLOOD VESSEL
DETECTION DURING STEREOTACTIC BIOPSY OF BRAIN
TUMORS**

**Niklas A. Markwardt, Herbert Stepp, Gerhard Franz, Ronald Sroka, Marcus
Goetz, Petr Zelenkov und Adrian Rühm**

J. Biophotonics 1–15 (2016) / doi: 10.1002/jbio.201600193

Copyright Wiley-VCH Verlag GmbH & Co. KGaA. Nachdruck mit Genehmigung.

FULL ARTICLE

Remission spectrometry for blood vessel detection during stereotactic biopsy of brain tumors

Niklas A. Markwardt*, **,1,2, Herbert Stepp^{1,2}, Gerhard Franz³, Ronald Sroka^{1,2}, Marcus Goetz⁴, Petr Zelenkov⁵, and Adrian Rühm^{1,2}

¹ Laser-Forschungslabor, LIFE Center, University Hospital of Munich, Munich, Germany

² Department of Urology, University Hospital of Munich, Munich, Germany

³ Department of Applied Sciences and Mechatronics, Munich University of Applied Sciences, Munich, Germany

⁴ MRC Systems GmbH, Heidelberg, Germany

⁵ Burdenko Neurosurgery Institute, Moscow, Russia

Received 5 July 2016, revised 14 September 2016, accepted 15 September 2016

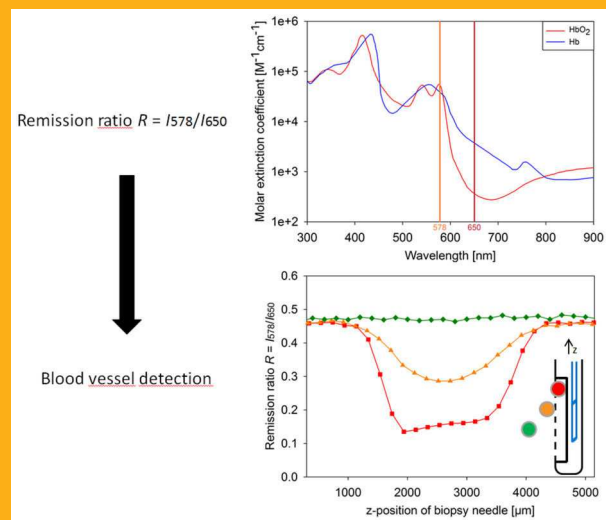
Published online 10 October 2016

Key words: stereotactic biopsy, glioblastoma multiforme, hemorrhage, blood vessel detection, optical phantoms, ray tracing simulations

Stereotactic biopsy is used to enable diagnostic confirmation of brain tumors and treatment planning. Despite being a well-established technique, it is related to significant morbidity and mortality rates mostly caused by hemorrhages due to blood vessel ruptures.

This paper presents a method of vessel detection during stereotactic biopsy that can be easily implemented by integrating two side-view fibers into a conventional side-cutting biopsy needle. Tissue within the needle window is illuminated through the first fiber; the second fiber detects the remitted light. By taking the ratio of the intensities at two wavelengths with strongly differing hemoglobin absorption, blood vessels can be recognized immediately before biopsy sampling.

Via ray tracing simulations and phantom experiments, the dependency of the remission ratio $R = I_{578}/I_{650}$ on various parameters (blood oxygenation, fiber-to-vessel and inter-fiber distance, vessel diameter and orientation) was investigated for a bare-fiber probe. Up to 800–1200 μm away from the probe, a vessel can be recognized by a considerable reduction of the remission ratio from the background level. The technique was also successfully tested with a real biopsy needle probe on both optical phantoms and *ex-vivo* porcine brain tissue, thus showing potential to improve the safety of stereotactic biopsy.



Dual-wavelength remission measurement for the detection of blood vessels during stereotactic biopsy.

* Corresponding author: e-mail: Niklas.Markwardt@med.uni-muenchen.de, Phone: +49 89 4400 74880, Fax: +49 89 4400 74864

** This manuscript is part of the inaugural thesis of Niklas Markwardt to be submitted at the Medical Faculty of the Ludwig-Maximilians-Universität, Munich.

1. Introduction

Stereotactic biopsy is a well-established method in neurosurgery. It is applied for the diagnosis of cerebral neoplasms if radiographic information is insufficient or for diagnostic confirmation and treatment planning in case open resection is not possible [1].

Among the group of gliomas, which account for about 80% of all primary malignant brain tumors, glioblastoma multiforme represents the most prevalent and malignant tumor type [2, 3]. With a 5-year survival rate of less than ~5% [3, 4], its prognosis is very poor. Chemotherapy based on alkylating agents such as temozolomide is a promising therapeutic option for patients with a methylated O⁶-methylguanine-DNA methyltransferase (MGMT) gene promoter [5]. Stereotactic biopsy may be used to assess this MGMT status as well as further biomarkers that influence prognosis and enable personalized treatment such as the proliferative index Ki-67, mutations on the isocitrate dehydrogenase genes IDH1/2, and alterations of chromosome arms 1p and 19q [6–8].

The principle of stereotactic biopsy is illustrated in Figure 1a. To obtain a tissue sample, a biopsy needle is attached to the stereotactic frame and inserted into the brain along a predefined trajectory until the distal needle end is positioned in an area of vital tumor. Despite its broad application, stereotactic biopsy is associated with significant risks. Mortality [1, 11–13] and serious morbidity [12–15] rates of up to 3.8% and 12%, respectively, have been reported. Most complications are caused by hemorrhages, which can lead to severe neurological deficits or death. Malone et al. report on a biopsy-related mortality of 13% in case a hemorrhage was observed during biopsy, which was six-fold higher than for all other patients [1]. In most studies, moderate occurrence rates of hemorrhages ranging from 0.3% to

7% are indicated [1, 15–17], but Kulkarni et al. [11] found an alarmingly high rate of silent hemorrhages (54%), which occasionally lead to delayed neurological deficits. Given these numbers, a stereotactic device would be desirable that is capable of detecting larger blood vessels during intervention to avoid rupture by the biopsy needle.

There have already been several approaches to detect blood vessels during stereotactic biopsy or similar neurosurgical interventions, including Doppler sonography [18], laser Doppler flowmetry (LDF) [19], Indocyanine Green (ICG) fluorescence [20], and interstitial optical tomography (iOT) [21, 22]. Especially LDF, which seems to be the method with the highest clinical potential, has already been tested in surgical interventions [23, 24]. So far, however, none of these attempts has been routinely implemented in stereotactic biopsy, for some of these methods probably due to the required sophisticated probe.

In this paper, a comparatively simple technique is presented that may be permanently integrated into a side-cutting biopsy needle (cf. Figure 2c). It is conceived for blood vessel detection within the tissue volume contained inside the suction window where the risk of vessel rupture is maximal, namely during the step of tissue sampling. Due to the rounded distal end of the biopsy needle, blood vessels in front of the needle that might get hit during needle insertion are at considerably lower risk as they would most probably be pushed aside and not be ruptured. The method is based on the characteristic spectral dependence of the absorption of hemoglobin (Figure 1b). The probed tissue is illuminated (e.g. with a broadband light source) and the remitted light intensity is recorded at two wavelengths with highly differing hemoglobin absorption (e.g. 578 nm and 650 nm). 578 nm was selected as first wavelength be-

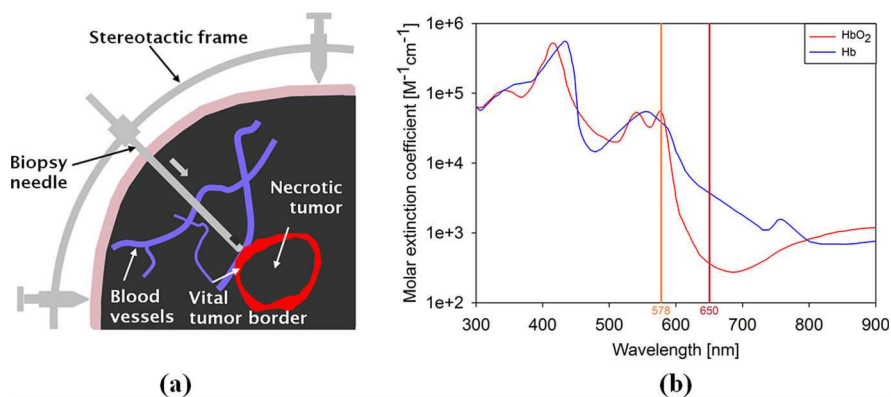


Figure 1 (a) Stereotactic biopsy of brain tumors. A biopsy needle is attached to the stereotactic frame and inserted into the brain along a predefined trajectory (indicated by the arrow) until the distal needle end is positioned in an area of vital tumor tissue. (Adapted with permission from Markwardt et al. [9].) (b) Molar extinction coefficients of oxygenated (HbO₂) and deoxygenated (Hb) hemoglobin. The wavelengths 578 nm and 650 nm are indicated by orange and dark red lines, respectively. (Data taken from Prahl [10].)

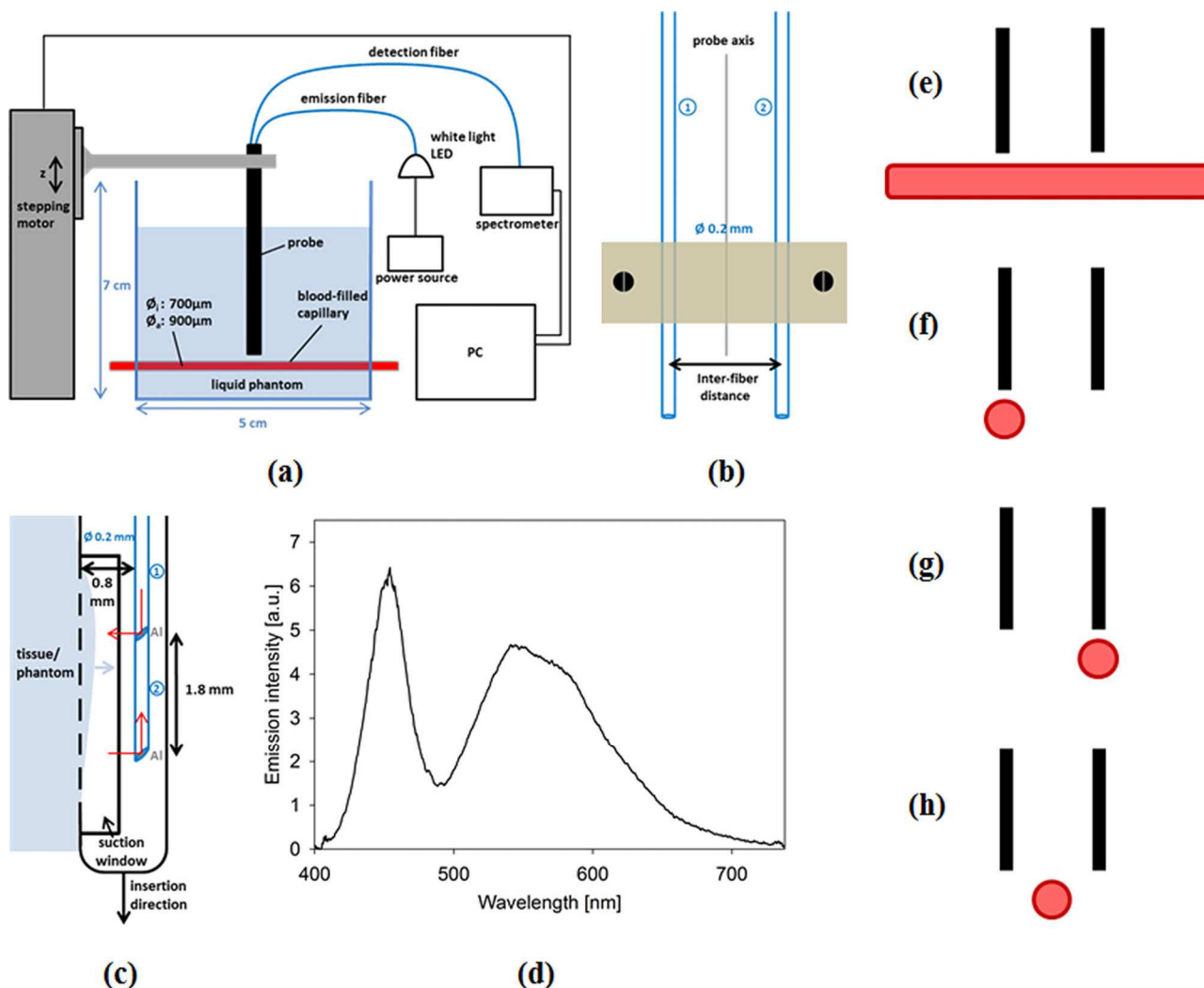


Figure 2 (a) Sketch of the setup used for phantom experiments. The liquid phantom was filled into a cylindrical container (drawn in blue), which incorporated a blood-filled glass capillary simulating a blood vessel. For the tissue experiments, the phantom container was replaced by a beaker containing the investigated tissue. The probe could be moved with a computer-controlled stepping motor. Light of a broadband LED was coupled into the emission fiber; the remission light was collected with the detection fiber and guided to a spectrometer. (b) Bare-fiber probe consisting of polished crosscut fibers (core diameter: 0.2 mm) fixed between two screwable plastic blocks (1: emission fiber, 2: detection fiber). (c) Needle probe consisting of a biopsy needle with integrated aluminum-coated (Al) side-view fibers (1: emission fiber, 2: detection fiber, core diameter: 0.2 mm). (d) LED emission spectrum acquired with the bare-fiber probe via reflection from a white remission standard, normalized to 1 at 650 nm. Blood vessel orientations used for experiments and simulations: (e) coplanar, (f) perpendicular, ahead of emission fiber, (g) perpendicular, ahead of detection fiber, (h) perpendicular, between fibers.

cause it is associated with a local absorption maximum of oxygenated hemoglobin (the global maximum slightly above 400 nm would have provided even higher hemoglobin absorption, but also a tissue penetration depth that would have been too low for a reasonable blood vessel detection range resulting from the combination of both wavelengths). The choice of 650 nm as second wavelength was the result of a trade-off between the highest possible difference in hemoglobin absorption and technical

practicability (evaluation around 700 nm would have provided even lower hemoglobin absorption, but also very low remission intensity values due to the emission characteristics of typical white light LEDs, cf. e.g. Figure 2d). Phantom and tissue experiments as well as ray tracing simulations were used to demonstrate the functionality of this technique.

2. Materials and methods

2.1 Experimental setup

2.1.1 Overview

The experiments conducted on optical phantoms are described in detail in Section 2.2.1, the experiments on biological tissue (taken from the slaughterhouse) in Section 2.2.2. The setup for the phantom experiments is shown in Figure 2a. A liquid phantom, mimicking tissue optical properties, was poured into a plastic container whose inner walls were coated with black paint to avoid reflections. To simulate a blood vessel, a cylindrical glass capillary (inner diameter: 700 μm , wall thickness: 100 μm) was filled with fresh heparinized blood, sealed with modeling clay, and inserted into the container through two diametrically opposed holes. In the following, the term *fiber-to-capillary distance* always refers to the distance of the fiber tips from the inner surface of the capillary wall.

Remission measurements were performed with a two-fiber probe (Section 2.1.2). Light from a broadband light emitting diode (LED) (APG2C3-NW, Roithner Lasertechnik GmbH, Vienna, Austria) with a total output power of 500 mW, measured with a powermeter (thermal head LM-10, Coherent, Inc., Santa Clara, CA, USA), was coupled into the emission fiber. The light power that was coupled out of the distal end of the emission fiber was 70 μW , yielding a maximum irradiance (directly at the distal fiber end) of about 2.2 kW/m^2 , which approximately corresponds to the maximum permissible exposure (MPE) for the skin in the employed wavelength range (2 kW/m^2) [25]. A normalized emission spectrum of the LED is shown in Figure 2d; it was acquired with the bare-fiber probe via reflection from a white reflectance standard with a reflectivity of $99 \pm 0.5\%$ in the employed wavelength range (SG 3054/26, LOT-Oriel GmbH, Darmstadt, Germany) and the same spectrometer as in the following experiments. The remitted light was collected with the detection fiber and guided to a spectrometer (AVS-USB2000, Avantes, Inc., Broomfield, CO, USA), which – in combination with the 200 μm detection fiber (see Section 2.1.2) – provided a spectral resolution of 5 nm at both exploited wavelengths (578 nm and 650 nm) and which was readout via OOIBase32 (Ocean Optics GmbH, Ostfildern, Germany). The integration time was set to 75 ms, 300 ms and 900 ms for investigating inter-fiber distances of 1 mm, 2 mm and 3 mm, respectively. The use of a spectrometer instead of, for instance, two detection channels with narrowband filters and less expensive photodiodes provided the possibility to obtain additional evidence for the presence of blood in front of the fiber probe beyond the ratio of the remitted intensities at

578 nm and 650 nm, i.e. the identification of the characteristic absorption maxima of oxygenated hemoglobin at around 540 nm and 580 nm in the remission spectra. A LabVIEW-controlled stepping motor with 2.5 μm precision enabled accurate probe displacements in z -direction. For the tissue experiments, the same setup was employed; only the phantom container with embedded glass capillary was replaced with a beaker containing porcine brain tissue with naturally incorporated blood vessels.

2.1.2 Optical probes

Two different optical probes were used to deliver light to or from the phantom or tissue sample: a *bare-fiber probe* consisting of two crosscut optical fibers (Figure 2b) and a *needle probe* consisting of a biopsy needle with two integrated side-view fibers (Figure 2c). In a first step (Section 3.1.1), the bare-fiber probe was used for experimental simplicity and accuracy to investigate in phantom experiments the dependencies of the remission signal on different parameters like inter-fiber distance, fiber-to-vessel distance and relative vessel orientation. In a second step, the functionality of the needle probe, as it is intended to be applied clinically, was checked in phantom (Section 3.2.1) and tissue (Section 3.2.2) experiments. Both probes were based on polyimide-coated silica fibers (UM22-200, Thorlabs GmbH, Dachau, Germany) with a core diameter of 200 μm , an outer diameter of 240 μm , and a numerical aperture (NA) of 0.22.

For the bare-fiber probe, two polished crosscut fibers were fixed, parallel to each other, to a special fiber holder consisting of two screwable plastic blocks. Grooves of 0.5 mm thickness and 1 mm separation (center-to-center) were milled into one of the blocks to guarantee a well-defined inter-fiber distance, which was varied between 1 mm and 3 mm (axis-to-axis). After fastening the fibers to the holder, the actual distance between the distal fiber ends was controlled with a high-precision ruler (uncertainty: ± 0.2 mm); their separation from the fiber holder along the fiber axis was several centimeters to exclude signal falsification by light reflections.

The needle probe was constructed by gluing two side-view fibers into the inner cannula (inner/outer diameter: 1.1/1.4 mm, respectively) of a PAJUNK® BrainPro biopsy cannula set (Pajunk GmbH, Geisingen, Germany). This inner cannula can be turned relative to an outer cannula (1.4/1.8 mm, not shown in Figure 2c) to shear off tissue extending into the suction window. Side-view fibers were produced by grinding the distal fiber ends at an inclination angle of 45° and subsequently coating the ground surfaces with aluminum in a high-vacuum vapor coating sys-

Table 1 Optical properties of the liquid phantom: aspired literature data for brain tumor tissue [26–28] and experimentally achieved data measured with an integrating sphere (mean values \pm one standard deviation).

Wavelength [nm]	μ_a [mm ⁻¹]		μ'_s [mm ⁻¹]	
	aspired	achieved	aspired	achieved
578	0.21 \pm 0.09	0.22 \pm 0.02	1.8 \pm 1.0	1.9 \pm 0.2
650	0.068 \pm 0.038	0.074 \pm 0.007	1.6 \pm 0.9	1.7 \pm 0.2

tem. The distal ends of the fibers were placed within the suction window adjacent to each other, with a positional offset of (1.8 \pm 0.2) mm parallel to the fiber axes. The viewing directions of the side-view fibers were aligned into the direction of the needle opening with an estimated accuracy of $\pm 10^\circ$.

2.1.3 Liquid phantom

The liquid phantom was designed to mimic brain tumor optical properties at the wavelengths 578 nm and 650 nm. Lipovenös® (Fresenius Kabi GmbH, Bad Homburg, Germany) as well as a mixture of ink (“brilliant black 4001”) and India ink (“Tusche A”, black, both from Pelikan GmbH, Hannover, Germany) were used to reproduce reduced scattering ($\mu'_s = \mu_s \cdot (1 - g)$, where μ_s and g denote scattering coefficient and anisotropy) and absorption (μ_a) coefficients, respectively. For this purpose, data published by Gebhart et al. (glioma, determined *in vitro* on $n = 39$ samples) [26], Yaroslavsky et al. (astrocytoma, *in vitro*, $n = 4$) [27] and Beck et al. (glioma, *in vivo*, $n = 12$, only applied to 650 nm) [28] were compiled (see aspired literature data in Table 1). Two different types of absorbers were required to tune μ_a simultaneously for both wavelengths because the spectral absorption characteristics of tissue and ink diverge. However, a single scatterer, namely Lipovenös®, was sufficient to model μ'_s at both wavelengths. Phantom ingredient concentrations (Table 2) have been determined from literature data [29] (Lipovenös®) and by absorption spectroscopy (Lambda 40, Perkin Elmer GmbH, Überlingen, Germany) (ink, India ink) and confirmed via integrating sphere measurements (see experimentally achieved data in Table 1).

Table 2 Concentrations of the phantom ingredients.

Phantom ingredient	Concentration [%]
Lipovenös®	1.1 (mass of soybean oil/vol)
ink (“brilliant black 4001”)	0.046 (vol/vol)
India ink (“Tusche A”)	0.003 (vol/vol)

2.2 Experiments

2.2.1 Phantom experiments

2.2.1.1 Bare-fiber probe

In the empty phantom container, the horizontally mounted capillary was first positioned within the plane spanned by the axes of the two vertically oriented fibers, in the following referred to as *fiber plane*. Then the probe was moved downward until the distal fiber ends were in contact with the capillary surface (uncertainty: $\pm 10 \mu\text{m}$) and thus 100 μm away from the capillary lumen. Parts of the experiments were conducted in this coplanar configuration (Figure 2e); alternatively, after defining the vertical probe position, the capillary was turned perpendicular to the fiber plane, then crossing the virtual extension of either the emission fiber (Figure 2f), the detection fiber (Figure 2g), or the probe axis (Figure 2h), i.e. the center line between the two fiber axes representing the main rotation axis of the probe as shown in Figure 2b. The focus of experiments and simulations was on the coplanar configuration, which – due to geometry and functioning of the biopsy needle – bears a higher risk of blood vessel rupture than the perpendicular configurations. After alignment, the phantom liquid was carefully poured into the container and the probe was moved upward by 1800 μm in increments of 100 μm . For each vertical position, a spectrum was recorded. This alignment and measurement procedure was conducted three times for each configuration and inter-fiber distance.

2.2.1.2 Needle probe

In the phantom experiments performed with the needle probe, the capillary was always positioned perpendicular to the probe axis (cf. Figure 8a). The capillary was initially placed about one millimeter above the upper fiber end, at a varying fiber-to-capillary distance between 0.3 mm and 1.9 mm. After adding the phantom liquid, the needle probe was moved upward (in z -direction) by about 5 mm in steps of 0.2 mm. For each z -position, one spectrum was recorded.

2.2.2 Experiments on ex-vivo tissue

Ex-vivo measurements were performed with the needle probe on fresh porcine brain tissue about 1–2 h after slaughtering. The needle was inserted at ten different locations that were obviously not or very poorly perfused (“without blood vessel”) and at further ten different locations that were obviously well supplied with blood (“with blood vessel”). For each needle position, one spectrum was recorded.

2.3 Ray tracing simulations

To support and extend the experimental results, Monte Carlo-based ray tracing simulations were performed for the wavelengths 578 nm and 650 nm using TracePro (Version 4.1.7, Lambda Research Corporation, Littleton, MA, USA). The geometric model is illustrated in Figure 3. The used optical parameter sets are listed in Table 3; absorption and scattering coefficients are specified for 578 nm and 650 nm, the refractive index (n) is valid for both wavelengths.

Two different versions of the simulation model were used: either a homogeneous blood-tumor phantom without blood vessel, to which different blood volume fractions (BVF) were applied (Section 2.3.1), or a tumor phantom with blood vessel where diameter, position and orientation (within (coplanar) or perpendicular to the fiber plane) of the blood vessel were varied (Section 2.3.2). For each BVF or fiber-vessel configuration, respectively, three independent simulations with different random number seeds were performed.

2.3.1 Homogeneous blood-tumor phantom

The first version of the simulation model consisted of identical emission and detection fibers, both embedded into a cylindrical phantom that was infinitely large as compared to the local light penetration depth (≤ 1.7 mm). Depending on the applied BVF, the optical properties of the phantom were calculated as a linear superposition of tumor [26–28] and blood [30] properties, assuming a BVF of 5% to be already included in the optical properties of pure tumor due to its capillary perfusion [31]. Venous

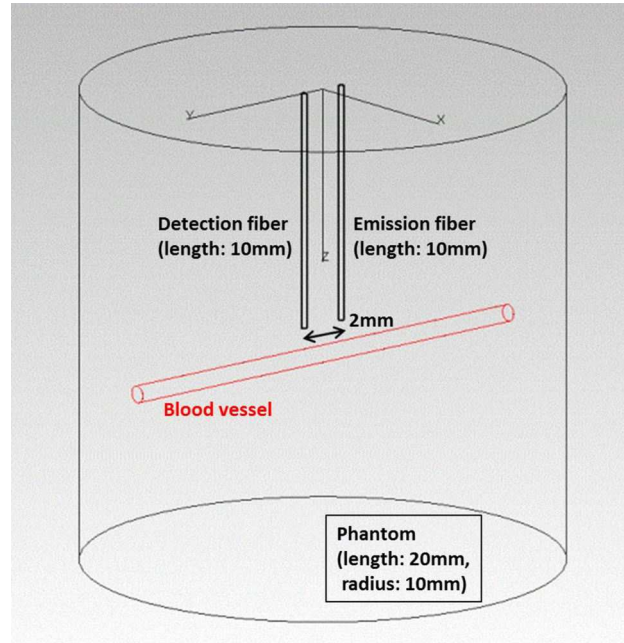


Figure 3 Geometric model used for simulations in a tumor phantom with blood vessel where diameter, position and orientation (within (coplanar) or perpendicular to the fiber plane) of the blood vessel were varied. For simulations in a homogeneous blood-tumor phantom, the blood vessel was removed and different blood volume fractions were attributed to the phantom.

and arterial blood with oxygen saturations of 75% and $\geq 98\%$, respectively, were examined separately [30]. The fibers, composed of non-absorbing and non-scattering core ($n = 1.46$) and cladding ($n = 1.44$) and of a perfectly absorbing and non-scattering coating ($n = 1.66$), were positioned parallel and symmetrical to the z -axis with an axis-to-axis spacing of 2 mm. A circular light source (diameter: 0.2 mm), which was positioned in the core of the emission fiber 0.5 mm below the proximal fiber end face ($z = 0.5$ mm), emitted 10^7 rays. The proximal end face of the detection fiber core ($z = 0$) served as detector.

2.3.2 Tumor phantom with blood vessel

In the second version of the simulation model, a blood-vessel mimicking cylinder was additionally in-

Table 3 Refractive index (n), absorption (μ_a) and reduced scattering (μ'_s) coefficients of the simulation objects (BVF: blood volume fraction).

Object/Entity	n	μ_a [mm^{-1}]		μ'_s [mm^{-1}]		
		578 nm/650 nm	578 nm	650 nm	578 nm	650 nm
pure tumor (5.0% BVF)	1.4	0.21	0.068	1.8	1.6	
blood vessel (100% BVF)	vein	1.3	25.1	0.57	2.1	1.5
	artery	1.3	26.9	0.16	2.3	1.5

serted into the phantom at different orientations and distances from the fibers. The cylinder diameter was varied between 100 μm and 1500 μm . Pure tumor properties (5% BVF [26–28]) were assigned to the phantom, pure blood properties (100% BVF, either venous or arterial [30]) to the vessel-mimicking cylinder. To corroborate the direct comparability with the experimental results, some simulations were performed with a non-absorbing and non-scattering glass wall (thickness: 100 μm , glass type: pure silica, $n = 1.46$) around the vessel-mimicking cylinder. All indicated fiber-to-vessel distances refer to the distance from the blood cylinder inside the glass.

2.4 Data analysis

Data analysis including statistical evaluations was performed with MATLAB (Version R2014b (8.4.0.150421), The MathWorks, Inc., Natick, MA, USA) and SigmaPlot (Version 11.0, Systat Software GmbH, Erkrath, Germany). The experimental raw spectra $I_{\text{raw}}(\lambda)$ with intensity values given in counts per ms integration time were corrected by the dark spectra $I_{\text{dark}}(\lambda)$ and subsequently divided by the corrected LED emission spectrum $I_{\text{LED}}(\lambda) - I_{\text{dark}}(\lambda)$ shown in Figure 2d (normalization). Thereafter, the normalized intensity values I_{578}^{norm} (averaged over 6 pixels between 577 nm and 579 nm) and I_{650}^{norm} (averaged between 649 nm and 651 nm) were used to calculate the remission ratio R :

$$R = \frac{I_{578}^{\text{norm}}}{I_{650}^{\text{norm}}} = \frac{\left\langle \frac{I_{\text{raw}}(\lambda) - I_{\text{dark}}(\lambda)}{I_{\text{LED}}(\lambda) - I_{\text{dark}}(\lambda)} \right\rangle_{577-579}}{\left\langle \frac{I_{\text{raw}}(\lambda) - I_{\text{dark}}(\lambda)}{I_{\text{LED}}(\lambda) - I_{\text{dark}}(\lambda)} \right\rangle_{649-651}} \quad (1)$$

In case of the simulations, the ratio of the detected fluxes at 578 nm and 650 nm was analogously

calculated via Eq. (1), however without dark correction, normalization and averaging. Gaussian error propagation was used to calculate the uncertainty of the remission ratio R . Exponential curve fitting (Levenberg–Marquardt algorithm), statistical significance (unpaired two-tailed t -test, normality (Shapiro–Wilk test) and equal variance of the two groups had been tested beforehand) and correlation (Pearson product-moment correlation) testing were performed via SigmaPlot.

3. Results

3.1 Experiments and simulations with bare fibers

3.1.1 Experiments with blood-filled glass capillary: Dependency on fiber-to-capillary distance, capillary orientation, and inter-fiber distance

The dependency of the experimentally determined remission ratio R on the fiber-to-capillary distance is displayed in Figure 4a for different fiber-probe orientations (bare-fiber probe, inner capillary diameter: 700 μm , inter-fiber distance: 2 mm). In the coplanar configuration, the remission ratio is zero when the fibers are in direct contact with the capillary wall (fiber-to-capillary distance: 100 μm). With increasing fiber-to-capillary distance, the ratio rises up to a saturation level of 0.44. In the perpendicular configurations, the signal depends on the location of the capillary relative to the probe axis: When the capillary crosses the probe axis (“perpendicular, between fibers”), almost identical remission ratios as in the coplanar configuration are obtained for fiber-to-

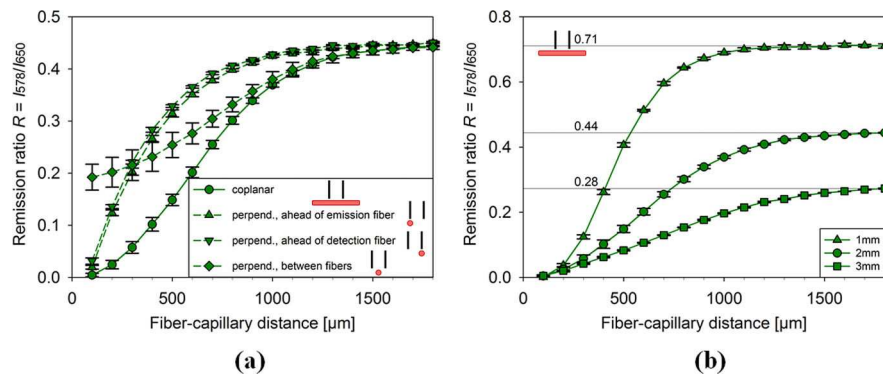


Figure 4 Experimental remission ratio R with the bare-fiber probe and a 700 μm capillary in dependency on the fiber-to-capillary distance for (a) different capillary orientations at an inter-fiber distance of 2 mm and (b) different inter-fiber distances in the coplanar configuration. Error bars denote standard errors of the means obtained from three measurements after renewed adjustment of the relative probe-capillary orientation.

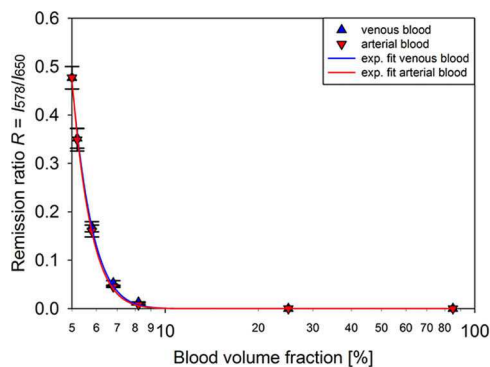
capillary distances above 1000 μm . Towards smaller distances, the ratio decreases more slowly and reaches a minimum value slightly below 0.2 at the smallest possible fiber-to-capillary distance of 100 μm . When the capillary is positioned directly ahead of the emission or detection fiber, however, the ratio diminishes only slightly for distances down to about 700 μm . Below this distance value, the ratio is subject to a steep decrease and vanishes in the immediate vicinity of the probe.

For the coplanar configuration, the dependency on the fiber-to-capillary distance was additionally investigated by using inter-fiber distances of 1 mm and 3 mm (Figure 4b). In each case, the remission ratio reaches zero for fiber-to-capillary distances of 100 μm . The smaller the inter-fiber distance, the faster the ratio increases with rising fiber-to-capillary distance and the faster the respective saturation level (0.71, 0.44, and 0.28 for 1 mm, 2 mm, and 3 mm inter-fiber distance, respectively) is reached.

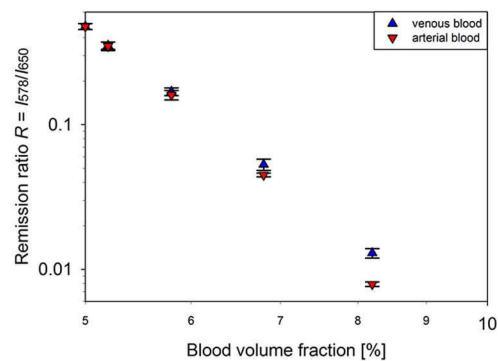
3.1.2 Simulations in homogeneous tumor phantom: Dependency on blood volume fraction

The remission ratio R derived from simulations in a homogeneous blood-tumor phantom strongly depends on the BVF (Figure 5a). In a pure tumor phantom (5% BVF), the ratio is 0.48, as determined in six independent simulations. In the following, this result for a tumor without BVF enhancement will be referred to as *background level*. With increasing BVF, the ratio decreases and practically equals zero for BVF values higher than about 10%. In good approximation, the obtained curves can be described by an exponential fit

$$R = a \cdot \exp(-b \cdot \text{BVF}[\%]) \quad (2)$$



(a)



(b)

Figure 5 Simulated remission ratio R for the bare-fiber probe (2 mm inter-fiber distance) in dependency on the BVF in the homogeneous blood-tumor phantom. (a) Semi-logarithmic plot. (b) Double-logarithmic plot. Error bars denote standard errors of the means obtained from three simulations with different random number seeds.

The resulting fit parameters are $a = 289 \pm 69$ and $b = 1.28 \pm 0.05$ for venous and $a = 437 \pm 89$ and $b = 1.37 \pm 0.04$ for arterial blood, respectively. In Figure 5b, a double-logarithmic plot of the same data reveals that venous blood leads to higher R values than arterial blood; this difference increases with rising BVF.

3.1.3 Simulations in tumor phantom with blood vessel: Dependency on fiber-to-vessel distance, vessel diameter and oxygen saturation

In Figure 6, the results of the simulations in the tumor phantom with blood vessel (coplanar configuration, without surrounding glass wall, inter-fiber distance: 2 mm) are shown. While the simulated remission ratios R for arteries with a diameter of 700 μm (Figure 6a) match the experimental results in the coplanar configuration (comparison shown in Figure 7a), the simulated remission ratios for veins are systematically higher. The indicated background level of 0.48 was taken from Section 3.1.2. As shown in Figure 6b for three exemplary fiber-to-vessel distances, the remission ratio is considerably higher for a blood vessel diameter of 100 μm than for larger diameters (500–1500 μm) where it remains approximately constant. Again, veins lead to a higher remission ratio than arteries.

3.1.4 Consistency of experimental and simulation results

Excellent accordance of the results obtained in experiments and simulations with arteries was obtained

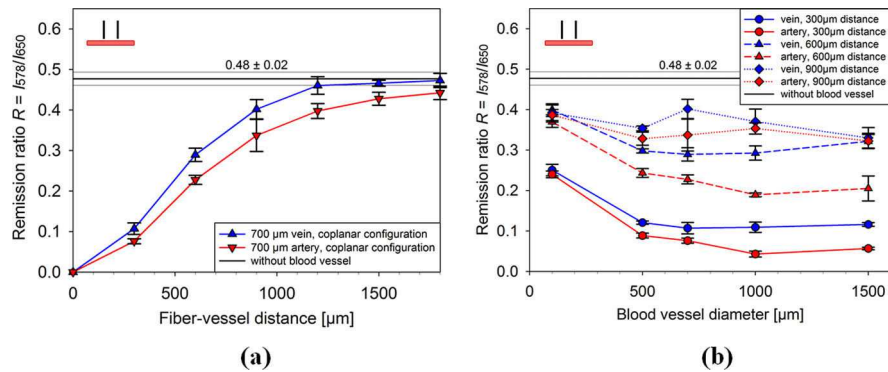


Figure 6 Simulated remission ratio R for the bare-fiber probe (2 mm inter-fiber distance) in dependency on (a) the fiber-to-vessel distance for a blood vessel of 700 μm diameter and (b) the blood vessel diameter for three fiber-to-vessel distances. Veins and arteries were considered separately. The blood vessel axis was always positioned within the fiber plane (coplanar configuration) and the vessel was not surrounded by a glass wall. Error bars denote standard errors of the means obtained from three simulations with different random number seeds.

for all orientations of the capillary or vessel, respectively, with regard to the bare-fiber probe (Figure 7); no systematic difference was found between the two versions of the simulation model (with/without glass). The correlation coefficients (Pearson's r) of all possible method pairs (experiment vs. simulation with glass, experiment vs. simulation without glass, simulation with glass vs. simulation without glass) for the respective orientations varied between 0.981 and 0.999.

3.2 Experiments with the needle probe

3.2.1 Experiments on tumor phantom with blood-filled glass capillary: Dependency on fiber-to-capillary distance and z-position of the needle probe

In Figure 8b, remission ratio profiles obtained by moving the needle probe along the z-direction are

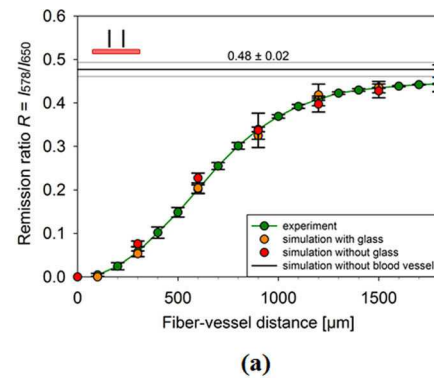
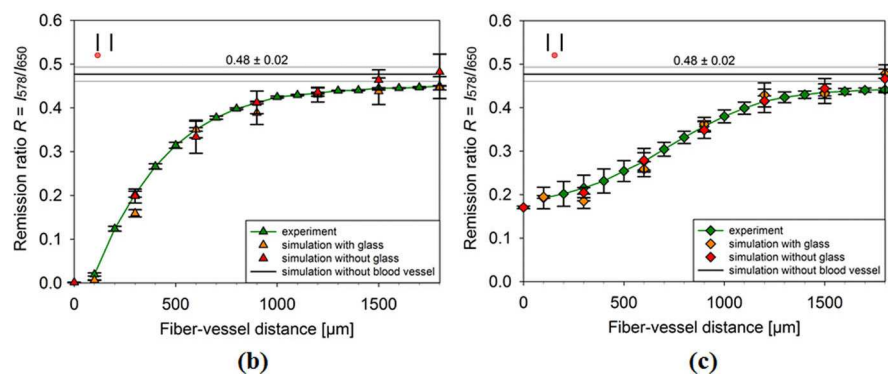


Figure 7 Comparison of experiment and simulation (with and without glass wall around the blood cylinder, in each case filled with arterial blood) based on results for the remission ratio R obtained with the bare-fiber probe (inter-fiber distance: 2 mm) and a capillary/blood vessel of 700 μm diameter (a) within the fiber plane (coplanar), (b) perpendicular to the fiber plane ahead of the emission fiber and (c) perpendicular to the fiber plane between the fibers.



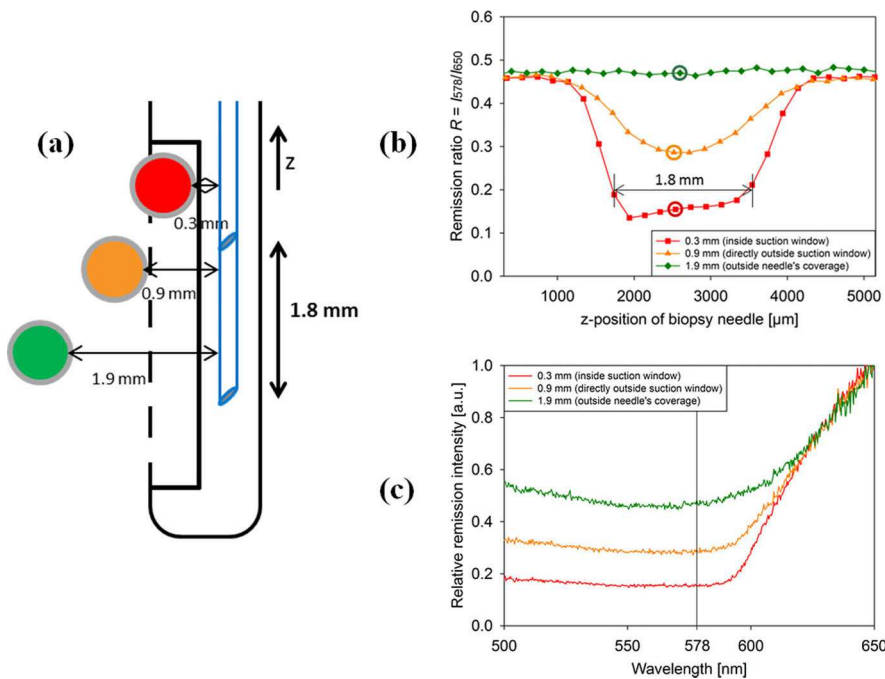


Figure 8 (a) Illustration of the experiments with the needle probe on the tumor phantom for three different fiber-to-capillary distances. After adjusting the fiber-to-capillary distance, the needle was moved in z -direction. The capillary orientation was perpendicular to the drawing plane. (b) Experimental results. The three fiber-to-capillary distances are indicated by the colors red, orange and green (cf. Figure 8a). (c) Three representative normalized remission spectra (intensity at 650 nm was set to 1), representing the three fiber-to-capillary distances indicated by the colors red, orange and green (cf. Figure 8a). The corresponding z -positions of the biopsy needle are marked in Figure 8b. The ordinate values at 578 nm (indicated by the vertical line) are equal to the remission ratios R .

shown for three fiber-to-capillary distances (Figure 8a) representing the model cases “vessel inside suction window (high risk)” (red), “vessel directly outside suction window (borderline case)” (orange) and “vessel outside needle’s coverage (no risk)” (green). Representative normalized remission spectra (one for each of these cases) are shown in Figure 8c. In the first case, the following blood-vessel indicating signature is clearly visible: The remission ratio R abruptly decreases from the background level 0.48 (representing homogeneous pure brain tumor tissue) to about 0.15 when passing the capillary with the end of the emission fiber (upper fiber in

Figure 8a) at $z \approx 1800 \mu\text{m}$. Afterwards, the ratio stays almost constant as long as the capillary is located between the two fiber ends (plateau), i.e. up to $z \approx 3600 \mu\text{m}$, and then re-increases to the background level after passing the capillary with the end of the detection fiber. The occurrence of the plateau with a length slightly below 1.8 mm (distance between fiber ends) is due to the selected fiber-to-capillary distance of 0.3 mm – a value that is close to the intersection point of the three curves in Figure 4a that represent the perpendicular configurations. For direct fiber-capillary contact, one would have expected two minima with a spacing of

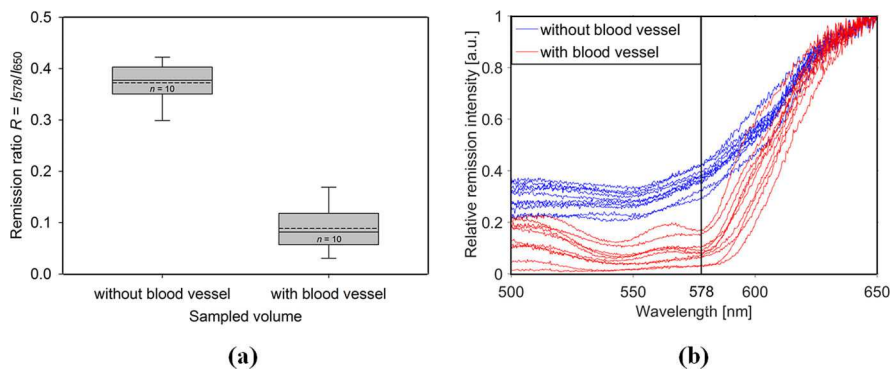


Figure 9 (a) Remission ratio R acquired with the needle probe on *ex-vivo* porcine brain tissue. The box plots display the median (solid line) and the average (dashed line) as well as the 5th, the 25th, the 75th and the 95th percentiles of the R values obtained at ten different locations within the tissue. The signal difference between biopsy volumes with and without blood vessel is statistically significant ($p \leq 0.001$). (b) Normalized remission spectra (intensity at 650 nm was set to 1), whose ordinate values at 578 nm (indicated by the vertical line) are equal to the remission ratios R .

1.8 mm. In the second case, the ratio only decreases from 0.48 to 0.3 with a minimum between the two fiber ends. Still, a blood vessel would be detectable in this borderline case. In the third case, the ratio does not deviate from the background level at any z -position, i.e. a blood vessel at this distance, which could not be sheared off during biopsy sampling, would not show up in the optical signal and thus not impair the biopsy procedure. All these findings are in reasonable accordance with the bare-fiber results (Figure 4a).

3.2.2 Experiments on ex-vivo porcine brain tissue: Dependency on needle position with respect to tissue vasculature

In porcine brain tissue, regions with and without blood vessel could well be distinguished with the needle probe (Figure 9a). The remission ratio R was significantly ($p \leq 0.001$) lower when the probed tissue volume contained one (or more) blood vessel(s) (average values: 0.09 vs. 0.37). The normalized remission spectra (Figure 9b) could also be clearly discriminated with regard to the presence of blood vessels; in most spectra obtained on tissue volumes with blood vessel, the characteristic absorption maxima of oxygenated hemoglobin at around 540 nm and 580 nm were visible. The remission ratio in tissue regions without blood vessel was subject to a moderate absolute standard deviation ($n = 10$) of 0.04 (relative standard deviation with respect to the average: 11%) and its average value 0.37 deviated by about 20% from the background level obtained in phantom experiments and simulations, which ranged from 0.44 to 0.48. This accuracy is compatible with the general accuracy limits of tissue optical properties. The absolute standard deviation of the remission ratio in tissue regions with blood vessel(s) was 0.05 ($n = 10$), the relative standard deviation was 52%.

4. Discussion

4.1 Validity of experiments and simulations

A priori, the experimental setting is best represented by the simulations with glass wall around the blood cylinder. Real blood vessels, however, are in principle better represented by the simulations without glass wall, provided that distances are measured from the inner surfaces of the vessel walls as it was the case in all presented experiments and simulations. This is due to the optical properties of vascular walls, which differ significantly from those of glass,

but only moderately (20–60%) from those of brain tissue [32] (aorta values taken as reference for vascular walls, determined *in vitro*, $n = 9$). But as a consequence of the displayed accordance of the results from all three methods (Figure 7), experiments and simulations with glass can be regarded as representing real blood vessels in tumor tissue equally well as the simulations without glass.

4.2 Dependency of the remission ratio on the investigated parameters

4.2.1 Impact of fiber-to-vessel distance for different blood vessel orientations

The dependencies of the remission ratio R on blood vessel orientation and fiber-to-vessel distance (Figure 4a) can be explained by the spatial distribution of paths associated with photons that emanate from the emission fiber and arrive at the detection fiber as sketched in Figure 10. This distribution, which is well-known in diffuse reflectance spectroscopy as *photon banana*, can be derived from Monte Carlo simulations [33, 34]. The flux line density, encoding the density of the above-mentioned photon paths in case no blood vessel is present, is a measure for the sensitivity of the recorded remission spectra, and thus the remission ratio R , to the local absorption. To determine the impact of a blood vessel on the detected remission ratio R , the local absorption, weighted with the local line density, has to be integrated over the entire vessel volume. In other words: the higher the line density in a certain region, the stronger the reduction of the detected remission ratio if a blood vessel with given diameter is located in that region.

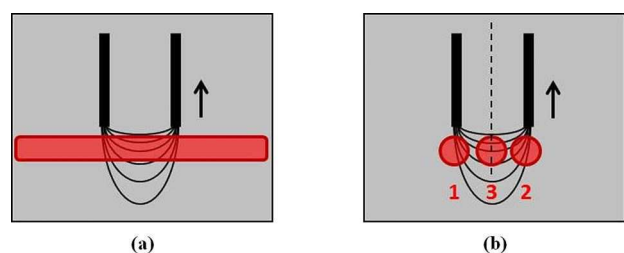


Figure 10 Flux line plot representing the stochastic spatial distribution of paths associated with photons that were emitted from one and detected with the other fiber (*photon banana*). The line density encodes the density of photon paths. Superimposed is a blood vessel (red) (a) within (coplanar) or (b) perpendicular to the fiber plane (positioned either directly ahead of the emission (1) or detection (2) fiber or between the two fibers (3); dashed line: probe axis). The arrow indicates the direction in which the fiber-probe is moved to adjust the fiber-to-vessel distance.

From Figure 10a, it can be discerned for the coplanar configuration that with increasing distance from the fiber tips, the line density decreases, so the presence of a blood vessel has a weaker influence on the recorded remission signal, which leads to an increase of the remission ratio (cf. Figure 4a). In the perpendicular configurations (Figure 10b), the symmetry with respect to the probe axis leads to an identical influence on the remission signal, whether the blood vessel is placed ahead of the emission (position 1) or detection (position 2) fiber: Starting at almost zero when the probe is in contact with the blood vessel, the remission ratio R undergoes a steep increase with rising fiber-to-vessel distance, followed by a convergence to the background level (cf. Figure 4a). When placed between the fibers (position 3), however, the blood vessel has a lower impact in the vicinity of the probe (lower line density than for positions 1 or 2), leading to a remission ratio of about 0.2, which is followed by a relatively shallow increase with rising fiber-to-vessel distance as compared to positions 1 or 2 (weaker decrease of line density than for positions 1 or 2). As a consequence, the coplanar orientation of a blood vessel leads to the best traceability. Up to a fiber-to-vessel distance of about 300 μm , a perpendicularly orientated blood vessel is better detectable directly ahead of either the emission or the detection fiber than between the fibers; for fiber-to-vessel distances larger than 300 μm , this relation is inverted.

4.2.2 Impact of blood vessel diameter

With increasing blood vessel diameter (and constant fiber-to-vessel distance), a larger volume in front of the fibers is covered with blood (Figure 10a). Consequently, thicker vessels are better detectable. This effect considerably decreases for blood vessel diameters larger than 500 μm (cf. Figure 6b) when regions with lower line densities are additionally covered by the vessel. Up to a fiber-to-vessel distance of 900 μm (dotted curve, Figure 6b), which approximately corresponds to the depth of the needle window (cf. Figure 2c), blood vessels in the coplanar configuration with a diameter down to at least 500 μm , possibly also 100 μm , should be discernible.

4.2.3 Impact of inter-fiber distance

With increasing inter-fiber distance, the background level of the remission ratio R recorded at large fiber-to-capillary distances decreases (Figure 4b). This is due to the absorption in the phantom, which is much

higher at 578 nm than at 650 nm (cf. Table 1) so that the shorter wavelength is more strongly suppressed with rising inter-fiber distance. The phenomenon that for a larger inter-fiber distance, the respective background level of R is reached at larger fiber-to-capillary distances (cf. Figure 4b) can also be explained with Figure 10a as an increasing inter-fiber distance leads to a lower line density gradient in the vicinity of the probe axis. As a consequence, probes with larger inter-fiber distances exhibit a higher sensitivity to distant blood vessels, albeit at the cost of lower intensities since more absorption events occur between the two fibers. With regard to the development and optimization of a biopsy-needle device, the suction window should not be considerably longer than the selected inter-fiber distance because the vessel detectability to the respective outer sides of both fiber tips rapidly decreases as shown in Figure 8b where the inter-fiber distance was 1.8 mm.

4.2.4 Impact of oxygen saturation

The simulations with blood vessel demonstrate that an artery in the vicinity of the probe reduces the remission ratio R more strongly than a vein (Figure 6). Thereby, the relative deviation of the arterial R from the venous R increases with decreasing fiber-to-vessel distance, i.e. with rising impact of the blood vessel on the detected remission spectra, from 6.4% at a distance of 1800 μm to 29% at a distance of 300 μm . This result is not surprising as arterial blood exhibits a higher absorption coefficient at 578 nm and a lower absorption coefficient at 650 nm than venous blood (cf. Table 3). Due to the definition of the remission ratio R according to Eq. (1), both effects add up to a reduced R for arteries as compared to veins, especially when the blood vessel is close to the fiber probe. Thus, using this method, arteries can be detected more easily than veins as they induce a remission ratio R that deviates more strongly from the background level of about 0.48. This might even improve the safety of the technique as artery ruptures are presumably more critical than vein ruptures.

In the homogeneous blood-tumor phantom, arterial blood leads to a lower remission ratio R than venous blood, too (Figure 5). In the semi-logarithmic plot of Figure 5a, the different blood types can hardly be discriminated because the remission ratios already converge to zero for relatively small BVF values around 10%. However, an increasing relative deviation of R with rising BVF can be discerned in the corresponding double-logarithmic plot (Figure 5b).

4.3 Reliability and limitations of the technique

4.3.1 Variations of tissue optical properties and decision threshold

By means of the presented technique, a blood vessel is recognized by the reduction of the remission ratio R from the far-distance background level that it induces. This suggests determining a ratio threshold above which biopsy sampling is deemed to be allowed and below which the surgeon would be well advised to better take the biopsy at a different site because a blood vessel could otherwise be injured. For safety purposes, this threshold should be chosen as high as possible. On the other hand, it should be sufficiently well below the background level to maintain the practicability of the technique. Furthermore, the threshold has to be specifically calibrated for each device as the background level depends on the exact inter-fiber distance (Figure 4b).

The definition of a reasonable threshold for a given probe requires assessing intra- and inter-individual variations of tissue optical properties (comprising the three tissue types tumor and – depending on the measurement position – also white and gray matter) as shown by the following rough estimation of the detected background level (and its uncertainty), which refers to the situation where no blood vessel is close enough to influence the remission ratio R :

For a time-independent point source, the solution of the diffusion equation for the photon flux is proportional to

$$\frac{1}{D(\lambda) \cdot r} \cdot \exp[-\mu_{\text{eff}}(\lambda) \cdot r] \quad (3)$$

where r is the source-detector distance and $D(\lambda) = 1/(3 \cdot (\mu_a(\lambda) + \mu'_s(\lambda)))$ and $\mu_{\text{eff}}(\lambda) = \sqrt{\mu_a(\lambda)/D(\lambda)}$ represent diffusion and effective attenuation coefficients at a given wavelength λ , respectively [35]. Substitution into Eq. (1) leads to a remission ratio of

$$R = \frac{D(650 \text{ nm})}{D(578 \text{ nm})} \cdot \exp(-\Delta\mu_{\text{eff}} r) \quad (4)$$

with $\Delta\mu_{\text{eff}} = \mu_{\text{eff}}(578 \text{ nm}) - \mu_{\text{eff}}(650 \text{ nm})$. Since $\mu'_s \gg \mu_a$ (as assumed in the diffusion approximation), the ratio of the diffusion coefficients can be approximated by the reciprocal ratio of the respective reduced scattering coefficients, which is almost constant for all three tissue types, taking values between 1.1 and 1.2 [26, 27]. This can be explained by the constant spectral scattering characteristics of cell and organelle membranes, which are presumed to be re-

sponsible for light scattering in tissue [36]. Consequently, the remission ratio R mainly depends on the difference $\Delta\mu_{\text{eff}}$:

$$R \propto \exp(-\Delta\mu_{\text{eff}} r) \quad (5)$$

Based on the data reported for all three tissue types (tumor, white and gray matter) [26, 27], the standard deviation of $\Delta\mu_{\text{eff}}$ amounts to about 50% of its mean value. Assuming a background level of 0.48 for R as determined for an inter-fiber distance of 2 mm via simulation (Figure 6), a $\Delta\mu_{\text{eff}}$ variation of 50% would yield remission ratios of $0.48^{(1-0.5)} = 0.69$ and $0.48^{(1+0.5)} = 0.33$, respectively. Hence, a threshold around 0.3, which corresponds to a fiber-to-vessel distance of about 800 μm in the coplanar configuration (cf. Figure 4a) and thus to the depth of the needle window (cf. Figure 2c), seems to be a reasonable choice for a probe with 2 mm inter-fiber distance.

4.3.2 Discrimination between blood vessel and blood in the interstitium

The differentiation between blood vessels and blood in the interstitium leaking from an injured minor blood vessel in the vicinity of the biopsy site remains an issue of the technique in the presented form. This could be problematic as even a small increase of the BVF has a significant effect on the remission ratio (Figure 5). Blood withdrawing by suction before tissue excision or a time-dependent signal acquisition might be possible solutions. The first measure could be implemented with a suction tube integrated into the biopsy needle; in the second case, one could identify blood vessels by means of time-dependent oscillations in the remission ratio due to the pulsed blood flow and the thereby induced change in vessel diameter. The principle of this photoplethysmographic measurement is already widely used in pulse oximeters [37–39] and is potentially also applicable to cerebral veins [37, 40, 41].

4.4 Clinical applicability

The presented remission spectrometric technique was conceived as a simple and readily realizable alternative to existing concepts regarding blood vessel detection. It appears to have a high clinical potential similar to LDF, which has already been tested clinically for tissue discrimination and blood perfusion mapping during deep brain stimulation. Based on the presented results, it provides a sensitivity comparable to Doppler sonography (minimum blood

vessel diameter: 100 μm /maximum distance: 1 mm) [18], ICG (600 $\mu\text{m}/1\text{ mm}$) [20] or iOT (300 $\mu\text{m}/1\text{--}2\text{ mm}$) [22].

In addition, the proposed technique offers several practical advantages: Firstly, due to its integration into the biopsy needle, the fiber probe does not have to be removed from the biopsy channel for tissue sampling, which benefits the clinical workflow and assures a maximal congruence of optically and mechanically sampled volumes. In opposition to LDF, no laser with high coherence length [42, 43], but only a less expensive LED is required. Furthermore, data acquisition is possible within 1 s, in opposition to LDF and iOT where several seconds [19] and several minutes [22] are required, respectively. Furthermore, compared to iOT, a much simpler probe design is possible as only two instead of 24 fibers are needed [21, 22]. Finally, in contrast to the ICG technique, no drug injection is necessary, which would bear further risks and most importantly would limit the time period during which blood vessel detection is possible to only a few minutes as the retention time of ICG in the blood circulation is limited [44].

The experimental details of the measurement technique can of course still be modified if desired. For instance, evaluation wavelengths other than 578 nm and 650 nm are conceivable: Using the isobestic points in the hemoglobin absorption spectra where the extinction coefficients of oxygenated and deoxygenated hemoglobin are identical, i.e. approximately 580 nm and 800 nm (cf. Figure 1b), would make the remission ratio independent of the oxygen saturation of the blood vessel. Thereby, arteries and veins could be detected with identical sensitivity and statistical analyses of in-vivo data regarding parameters like e.g. the vessel diameter could be simplified. In any case, medical approval is still required before the proposed technique can be brought to clinical practice.

5. Conclusion

We suggest dual-wavelength remission spectrometry by means of a two-fiber probe to detect blood vessels during stereotactic biopsy and thus minimize the risk of hemorrhages. Based on the presented results, blood vessels of $\geq 100\text{--}500\text{ }\mu\text{m}$ diameter should be well discernible, independently of their orientation, up to a distance of about 800 μm , i.e. within the suction window of a conventional biopsy needle where the risk of a rupture is present. For this sensing direction, side-view fibers are needed. Beyond that, blood vessels ahead of the biopsy needle might be detected with an additional bare-fiber probe integrated into the needle. Blood vessels more than

1500 μm away from the probe do not reduce the remission ratio and will thus not lead to false-positive results.

This simple and easily implementable method shows the potential to significantly increase the safety of stereotactic biopsy. Beyond this scope of application, the measurement principle could also be used for other surgical procedures. First experiments on *ex-vivo* tissue have confirmed its functionality, but further research (ideally *in vivo*) is still required to optimize the technique.

Acknowledgements Funding support by the German Ministry of Education and Research (BMBF) and the Russian Foundation for Assistance to Small Innovative Enterprises (FASIE) under grant numbers 01DJ14012A and 01DJ14012B (GLIOTAX) is gratefully acknowledged. The authors want to thank Werner Preisser, Armin Hadzimujic and Thomas Pongratz for valuable technical support.

Author biographies Please see Supporting Information online.

References

- [1] H. Malone, J. Yang, D. L. Hershman, J. D. Wright, J. N. Bruce, and A. I. Neugut, *World neurosurgery* **84**(4), 1084–1089 (2015).
- [2] M. L. Goodenberger and R. B. Jenkins, *Cancer Genet* **205**(12), 613–621 (2012).
- [3] Q. T. Ostrom, L. Bauchet, F. G. Davis, I. Deltour, J. L. Fisher, C. E. Langer, M. Pekmezci, J. A. Schwartzbaum, M. C. Turner, K. M. Walsh, M. R. Wrensch, and J. S. Barnholtz-Sloan, *Neuro Oncol* **16**(7), 896–913 (2014).
- [4] H. Ohgaki, *Methods Mol Biol* **472**, 323–342 (2009).
- [5] M. Weller, R. Stupp, G. Reifenberger, A. A. Brandes, M. J. van den Bent, W. Wick, and M. E. Hegi, *Nat Rev Neurol* **6**(1), 39–51 (2010).
- [6] S. Eigenbrod, R. Trabold, D. Brucker, C. Erös, R. Egensperger, C. La Fougere, W. Göbel, A. Rühm, H. A. Kretzschmar, J. C. Tonn, J. Herms, A. Giese, and F. W. Kreth, *Acta Neurochir (Wien)* **156**(8), 1427–1440 (2014).
- [7] C. W. Brennan, R. G. Verhaak, A. McKenna, B. Campos, H. Noushmehr, S. R. Salama, S. Zheng, D. Chakravarty, J. Z. Sanborn, S. H. Berman, R. Beroukhim, B. Bernard, C. J. Wu, G. Genovese, I. Shmulevich, J. Barnholtz-Sloan, L. Zou, R. Vegesna, S. A. Shukla, G. Ciriello, W. K. Yung, W. Zhang, C. Sougnez, T. Mikkelson, K. Aldape, D. D. Bigner, E. G. Van Meir, M. Prados, A. Sloan, K. L. Black, J. Eschbacher, G. Finocchiaro, W. Friedman, D. W. Andrews, A. Guha, M. Iacocca, B. P. O'Neill, G. Foltz, J. Myers, D. J. Weisenberger, R. Penny, R. Kucherlapati, C. M. Perou, D. N. Hayes, R. Gibbs, M. Marra, G. B. Mills, E. Lander, P. Spellman, R. Wilson, C. Sander, J. Weinstein, M. Meyerson, S. Gabriel, P. W. Laird, D. Haussler, G. Getz, and L. Chin, *Cell* **155**(2), 462–477 (2013).

- [8] J. S. Smith, A. Perry, T. J. Borell, H. K. Lee, J. O'Fallon, S. M. Hosek, D. Kimmel, A. Yates, P. C. Burger, B. W. Scheithauer, and R. B. Jenkins, *J Clin Oncol* **18**(3), 636–645 (2000).
- [9] N. A. Markwardt, N. Haj-Hosseini, B. Hollnburger, H. Stepp, P. Zelenkov, and A. Rühm, *J Biophotonics*, doi: 10.1002/jbio.201500195 (2015).
- [10] S. A. Prahl, Optical Absorption of Hemoglobin, tabulated data compiled from various sources (1999), <http://omlc.ogi.edu/spectra/hemoglobin>.
- [11] A. V. Kulkarni, A. Guha, A. Lozano, and M. Bernstein, *J Neurosurg* **89**(1), 31–35 (1998).
- [12] M. J. McGirt, G. F. Woodworth, A. L. Coon, J. M. Frazier, E. Amundson, I. Garonzik, A. Olivi, and J. D. Weingart, *J Neurosurg* **102**(5), 897–901 (2005).
- [13] R. Dammers, I. K. Haitsma, J. W. Schouten, J. M. Kros, C. J. Avezaat, and A. J. Vincent, *Acta Neurochir (Wien)* **150**(1), 23–29 (2008).
- [14] M. Nishihara, T. Sasayama, H. Kudo, and E. Kohmura, *The Kobe journal of medical sciences* **56**(4), E148–E153 (2011).
- [15] A. A. Shakal and E. A. Mokbel, *J Neurol Surg A Cent Eur Neurosurg* **75**(3), 177–182 (2014).
- [16] D. Kondziolka, A. D. Firlik, and L. D. Lunsford, *Neurol Clin* **16**(1), 35–54 (1998).
- [17] R. Grossman, S. Sadetzki, R. Spiegelmann, and Z. Ram, *Acta Neurochir (Wien)* **147**(6), 627–631 (2005).
- [18] J. Gilsbach, M. Mohadjer, and F. Munding, *Acta Neurochir (Wien)* **89**(1–2), 77–79 (1987).
- [19] K. Wardell, S. Hemm-Ode, P. Rejmstad, and P. Zsigmond, *Stereotact Funct Neurosurg* **94**(1), 1–9 (2016).
- [20] W. Göbel, D. Brucker, Y. Kienast, A. Johansson, G. Kniebühler, A. Rühm, S. Eigenbrod, S. Fischer, M. Goetz, F. W. Kreth, A. Ehrhardt, H. Stepp, K. M. Irión, and J. Herms, *Opt Express* **20**(24), 26117–26126 (2012).
- [21] A. Goyette, J. Pichette, M. A. Tremblay, A. Laurence, M. Jermyn, K. Mok, K. D. Paulsen, D. W. Roberts, K. Petrecca, B. C. Wilson, and F. Leblond, *Opt Lett* **40**(2), 170–173 (2015).
- [22] J. Pichette, A. Goyette, F. Picot, M. A. Tremblay, G. Soulez, B. C. Wilson, and F. Leblond, *Biomed Opt Express* **6**(11), 4238–4254 (2015).
- [23] K. Wardell, P. Blomstedt, J. Richter, J. Antonsson, O. Eriksson, P. Zsigmond, A. T. Bergenheim, and M. I. Hariz, *Stereotact Funct Neurosurg* **85**(6), 279–286 (2007).
- [24] K. Wardell, P. Zsigmond, J. Richter, and S. Hemm, *Neurosurgery* **72**(2 Suppl Operative), 127–140; discussion 140 (2013).
- [25] Directive 2006/25/EC of the European Parliament and of the Council of 5 April 2006 on the minimum health and safety requirements regarding the exposure of workers to risks arising from physical agents (artificial optical radiation) (19th individual Directive within the meaning of Article 16(1) of Directive 89/391/EEC) <<http://eur-lex.europa.eu/legal-content/EN/TXT/PDF/?uri=CELEX:02006L0025-20140101&from=EN>>
- [26] S. C. Gebhart, W. C. Lin, and A. Mahadevan-Jansen, *Phys Med Biol* **51**(8), 2011–2027 (2006).
- [27] A. N. Yaroslavsky, P. C. Schulze, I. V. Yaroslavsky, R. Schober, F. Ulrich, and H. J. Schwarzaier, *Phys Med Biol* **47**(12), 2059–2073 (2002).
- [28] T. J. Beck, W. Beyer, T. Pongratz, W. Stummer, R. Waidelich, H. Stepp, S. Wagner, and R. Baumgartner, in: *Proc. SPIE, Photon Migration and Diffuse-Light Imaging*, 2003.
- [29] R. Michels, F. Foschini, and A. Kienle, *Opt Express* **16**(8), 5907–5925 (2008).
- [30] N. Bosschaart, G. J. Edelman, M. C. Aalders, T. G. van Leeuwen, and D. J. Faber, *Lasers Med Sci* **29**(2), 453–479 (2014).
- [31] A. Rühm, W. Göbel, R. Sroka, and H. Stepp, *Photodiagnosis Photodyn Ther* **11**(3), 307–318 (2014).
- [32] V. Tuchin, *Tissue Optics – Light Scattering Methods and Instruments for Medical Diagnosis* (SPIE, Bellingham, Washington, USA, 2015), pp. 247–294.
- [33] I. J. Bigio and S. Fantini, *Quantitative Biomedical Optics* (Cambridge University Press, Cambridge, UK, 2016), pp. 229ff., esp. Fig. 8.2.
- [34] C. Mansouri and N. H. Kashou, *Conf Proc IEEE Eng Med Biol Soc* **2009**, 1457–1460 (2009).
- [35] L. Wang and H.-I. Wu, *Biomedical Optics: Principles and Imaging* (John Wiley & Sons, Inc., Hoboken, NJ, USA, 2007), pp. 98–99.
- [36] B. W. Pogue and M. S. Patterson, *J Biomed Opt* **11**(4), 041102 (2006).
- [37] M. Nitzan, A. Romem, and R. Koppel, *Medical devices* **7**, 231–239 (2014).
- [38] K. H. Shelley, *Anesthesia and analgesia* **105**(6 Suppl), S31–S36 (2007).
- [39] J. Allen, *Physiological measurement* **28**(3), R1–R39 (2007).
- [40] A. S. Echiadis, V. P. Crabtree, J. Bence, L. Hadjinikolaou, C. Alexiou, T. J. Spty, and S. Hu, *Physiological measurement* **28**(8), 897–911 (2007).
- [41] K. H. Shelley, D. Tamai, D. Jablonka, M. Gesquiere, R. G. Stout, and D. G. Silverman, *Anesthesia and analgesia* **100**(3), 743–747 (2005).
- [42] G. E. Nilsson, E. G. Salerud, N. O. T. Strömberg, and K. Wardell, *Laser Doppler perfusion monitoring and imaging. Biomedical Photonics Handbook* (editor: Tuan Vo-Dinh): Chapter 15 (CRC Press Boca Raton, Florida, USA, 2003), pp. 15.1–15.24
- [43] I. Fredriksson, C. Fors, and J. Johansson, *Laser Doppler Flowmetry – a Theoretical Framework*, Department of Biomedical Engineering, Linköping University (2007), www.imt.liu.se/bit/ldf/ldfmain.html.
- [44] A. Hagen, D. Grosenick, R. Macdonald, H. Rinneberg, S. Burock, P. Warnick, A. Poellinger, and P. M. Schlag, *Opt Express* **17**(19), 17016–17033 (2009).

LITERATURVERZEICHNIS

- [1] N. A. Markwardt, N. Haj-Hosseini, B. Hollnburger, H. Stepp, P. Zelenkov, and A. Rühm, *J Biophotonics* 9(9), 901–912 (2016)
- [2] N. A. Markwardt, H. Stepp, G. Franz, R. Sroka, M. Goetz, P. Zelenkov, and A. Rühm, *J Biophotonics*, doi: 10.1002/jbio.201600193 (2016)
- [3] A. Rühm, N. A. Markwardt, N. Dominik, C. Polzer, R. Sroka, and H. Stepp, prepared for submission to *J Biophotonics* (2017)
- [4] H. Malone, J. Yang, D. L. Hershman, J. D. Wright, J. N. Bruce, and A. I. Neugut, *World neurosurgery* 84(4), 1084-1089 (2015)
- [5] T. Schneider, C. Mawrin, C. Scherlach, M. Skalej, and R. Firsching, *Deutsches Ärzteblatt international* 107(45), 799-807; quiz 808 (2010)
- [6] Q. T. Ostrom, L. Bauchet, F. G. Davis, I. Deltour, J. L. Fisher, C. E. Langer, M. Pekmezci, J. A. Schwartzbaum, M. C. Turner, K. M. Walsh, M. R. Wrensch, and J. S. Barnholtz-Sloan, *Neuro Oncol* 16(7), 896-913 (2014)
- [7] R. Stupp, W. P. Mason, M. J. van den Bent, M. Weller, B. Fisher, M. J. Taphoorn, K. Belanger, A. A. Brandes, C. Marosi, U. Bogdahn, J. Curschmann, R. C. Janzer, S. K. Ludwin, T. Gorlia, A. Allgeier, D. Lacombe, J. G. Cairncross, E. Eisenhauer, R. O. Mirimanoff, R. European Organisation for, T. Treatment of Cancer Brain, G. Radiotherapy, and G. National Cancer Institute of Canada Clinical Trials, *N Engl J Med* 352(10), 987-996 (2005)
- [8] R. Stupp, M. E. Hegi, W. P. Mason, M. J. van den Bent, M. J. Taphoorn, R. C. Janzer, S. K. Ludwin, A. Allgeier, B. Fisher, K. Belanger, P. Hau, A. A. Brandes, J. Gijtenbeek, C. Marosi, C. J. Vecht, K. Mokhtari, P. Wesseling, S. Villa, E. Eisenhauer, T. Gorlia, M. Weller, D. Lacombe, J. G. Cairncross, R. O. Mirimanoff, R. European Organisation for, T. Treatment of Cancer Brain, G. Radiation Oncology, and G. National Cancer Institute of Canada Clinical Trials, *Lancet Oncol* 10(5), 459-466 (2009)
- [9] Q. T. Ostrom, H. Gittleman, P. Farah, A. Ondracek, Y. Chen, Y. Wolinsky, N. E. Stroup, C. Kruchko, and J. S. Barnholtz-Sloan, *Neuro Oncol* 15 Suppl 2, ii1-56 (2013)
- [10] H. Ohgaki, *Methods Mol Biol* 472, 323-342 (2009)
- [11] M. Sant, P. Minicozzi, S. Lagorio, T. Borge Johannesen, R. Marcos-Gragera, S. Francisci, and E. W. Group, *Int J Cancer* 131(1), 173-185 (2012)
- [12] M. L. Siker, M. Wang, K. Porter, D. F. Nelson, W. J. Curran, J. M. Michalski, L. Souhami, A. Chakravarti, W. K. Yung, J. Delrowe, C. T. Coughlin, and M. P. Mehta, *J Neurooncol* 104(1), 351-356 (2011)
- [13] Y. T. Oh, H. J. Cho, J. Kim, J. H. Lee, K. Rho, Y. J. Seo, Y. S. Choi, H. J. Jung, H. S. Song, D. S. Kong, H. J. Seol, J. I. Lee, Y. Yoon, S. Kim, D. H. Nam, and K. M. Joo, *PLoS One* 9(8), e103327 (2014)
- [14] J. H. Chiang, W. S. Cheng, L. Hood, and Q. Tian, *OMICS* 18(5), 310-323 (2014)
- [15] S. Eigenbrod, R. Trabold, D. Brucker, C. Erös, R. Egensperger, C. La Fougere, W. Göbel, A. Rühm, H. A. Kretschmar, J. C. Tonn, J. Herms, A. Giese, and F. W. Kreth, *Acta Neurochir (Wien)* 156(8), 1427-1440 (2014)
- [16] M. Weller, R. Stupp, G. Reifenberger, A. A. Brandes, M. J. van den Bent, W. Wick, and M. E. Hegi, *Nat Rev Neurol* 6(1), 39-51 (2010)
- [17] D. Jain, M. C. Sharma, C. Sarkar, P. Deb, D. Gupta, and A. K. Mahapatra, *Brain Tumor Pathol* 23(2), 71-75 (2006)
- [18] G. F. Woodworth, M. J. McGirt, A. Samdani, I. Garonzik, A. Olivi, and J. D. Weingart, *J Neurosurg* 104(2), 233-237 (2006)
- [19] I. U. Heinemann, M. Jahn, and D. Jahn, *Archives of biochemistry and biophysics* 474(2), 238-251 (2008)
- [20] S. R. Ennis, A. Novotny, J. Xiang, P. Shakui, T. Masada, W. Stummer, D. E. Smith, and R. F. Keep, *Brain Res* 959(2), 226-234 (2003)
- [21] A. Obwegeser, R. Jakober, and H. Kostron, *British journal of cancer* 78(6), 733-738 (1998)
- [22] L. Teng, M. Nakada, S. G. Zhao, Y. Endo, N. Furuyama, E. Nambu, I. V. Pyko, Y. Hayashi, and J. I. Hamada, *British journal of cancer* 104(5), 798-807 (2011)
- [23] R. C. Krieg, S. Fickweiler, O. S. Wolfbeis, and R. Knuechel, *Photochem Photobiol* 72(2), 226-233 (2000)
- [24] A. Johansson, G. Palte, O. Schnell, J. C. Tonn, J. Herms, and H. Stepp, *Photochem Photobiol* 86(6), 1373-1378 (2010)
- [25] S. Eljamel, *International journal of molecular sciences* 16(5), 10443-10456 (2015)
- [26] X. Su, Q. F. Huang, H. L. Chen, and J. Chen, *Photodiagnosis Photodyn Ther* 11(4), 451-458 (2014)
- [27] S. Zhao, J. Wu, C. Wang, H. Liu, X. Dong, C. Shi, Y. Liu, L. Teng, D. Han, X. Chen, G. Yang, L. Wang, C. Shen, and H. Li, *PLoS One* 8(5), e63682 (2013)

- [28] W. Stummer, U. Pichlmeier, T. Meinel, O. D. Wiestler, F. Zanella, and H. J. Reulen, *Lancet Oncol* 7(5), 392-401 (2006)
- [29] W. Stummer, T. Beck, W. Beyer, J. H. Mehrkens, A. Obermeier, N. Etminan, H. Stepp, J. C. Tonn, R. Baumgartner, J. Herms, and F. W. Kreth, *J Neurooncol* 87(1), 103-109 (2008)
- [30] A. Johansson, F. Faber, G. Kniebühler, H. Stepp, R. Sroka, R. Egensperger, W. Beyer, and F. W. Kreth, *Lasers Surg Med* 45(4), 225-234 (2013)
- [31] M. D. Krieger, P. T. Chandrasoma, C. S. Zee, and M. L. Apuzzo, *Seminars in surgical oncology* 14(1), 13-25 (1998)
- [32] G. K. Zoeller, R. J. Benveniste, H. Landy, J. J. Morcos, and J. Jagid, *Stereotact Funct Neurosurg* 87(3), 174-181 (2009)
- [33] A. O. Heper, E. Erden, A. Savas, K. Ceyhan, I. Erden, S. Akyar, and Y. Kanpolat, *Surg Neurol* 64 Suppl 2, S82-88 (2005)
- [34] C. M. Owen and M. E. Linskey, *J Neurooncol* 93(1), 139-149 (2009)
- [35] R. Dammers, I. K. Haitzma, J. W. Schouten, J. M. Kros, C. J. Avezaat, and A. J. Vincent, *Acta Neurochir (Wien)* 150(1), 23-29 (2008)
- [36] G. Tsermoulas, N. Mukerji, A. J. Borah, P. Mitchell, and N. Ross, *Br J Neurosurg* 27(2), 207-211 (2013)
- [37] G. Widhalm, G. Minchev, A. Woehrer, M. Preusser, B. Kiesel, J. Furtner, A. Mert, A. Di Ieva, B. Tomanek, D. Prayer, C. Marosi, J. A. Hainfellner, E. Knosp, and S. Wolfsberger, *Neurosurg Rev* 35(3), 381-391 (2012)
- [38] G. von Campe, M. Moschopoulos, and M. Hefti, *Acta Neurochir (Wien)* 154(4), 585-588 (2012)
- [39] S. Moriuchi, K. Yamada, M. Dehara, Y. Teramoto, T. Soda, M. Imakita, and M. Taneda, *J Neurosurg* 115(2), 278-280 (2011)
- [40] D. Kondziolka, A. D. Firlik, and L. D. Lunsford, *Neurol Clin* 16(1), 35-54 (1998)
- [41] A. A. Shakal and E. A. Mokbel, *J Neurol Surg A Cent Eur Neurosurg* 75(3), 177-182 (2014)
- [42] M. Bernstein and A. G. Parrent, *J Neurosurg* 81(2), 165-168 (1994)
- [43] R. Grossman, S. Sadetzki, R. Spiegelmann, and Z. Ram, *Acta Neurochir (Wien)* 147(6), 627-631 (2005)
- [44] A. V. Kulkarni, A. Guha, A. Lozano, and M. Bernstein, *J Neurosurg* 89(1), 31-35 (1998)
- [45] M. Nishihara, T. Sasayama, H. Kudo, and E. Kohmura, *The Kobe journal of medical sciences* 56(4), E148-153 (2011)
- [46] M. J. McGirt, G. F. Woodworth, A. L. Coon, J. M. Frazier, E. Amundson, I. Garonzik, A. Olivi, and J. D. Weingart, *J Neurosurg* 102(5), 897-901 (2005)
- [47] J. Gilsbach, M. Mohadjer, and F. Munding, *Acta Neurochir (Wien)* 89(1-2), 77-79 (1987)
- [48] K. Wardell, S. Hemm-Ode, P. Rejmstad, and P. Zsigmond, *Stereotact Funct Neurosurg* 94(1), 1-9 (2016)
- [49] W. Göbel, D. Brucker, Y. Kienast, A. Johansson, G. Kniebühler, A. Rühm, S. Eigenbrod, S. Fischer, M. Goetz, F. W. Kreth, A. Ehrhardt, H. Stepp, K. M. Irion, and J. Herms, *Opt Express* 20(24), 26117-26126 (2012)
- [50] A. Goyette, J. Pichette, M. A. Tremblay, A. Laurence, M. Jermyn, K. Mok, K. D. Paulsen, D. W. Roberts, K. Petrecca, B. C. Wilson, and F. Leblond, *Opt Lett* 40(2), 170-173 (2015)
- [51] J. Pichette, A. Goyette, F. Picot, M. A. Tremblay, G. Soulez, B. C. Wilson, and F. Leblond, *Biomed Opt Express* 6(11), 4238-4254 (2015)
- [52] S. Marbacher, E. Klinger, L. Schwyzer, I. Fischer, E. Nevzati, M. Diepers, U. Roelcke, A. R. Fathi, D. Coluccia, and J. Fandino, *Neurosurg Focus* 36(2), E10 (2014)
- [53] G. Hennig, H. Stepp, and A. Johansson, *Photodiagnosis Photodyn Ther* 8(3), 275-281 (2011)
- [54] S. C. Gebhart, W. C. Lin, and A. Mahadevan-Jansen, *Phys Med Biol* 51(8), 2011-2027 (2006)
- [55] A. N. Yaroslavsky, P. C. Schulze, I. V. Yaroslavsky, R. Schober, F. Ulrich, and H. J. Schwarzmaier, *Phys Med Biol* 47(12), 2059-2073 (2002)
- [56] M. Loshchenov, P. Zelenkov, A. Potapov, S. Goryajnov, and A. Borodkin, *Photonics and Lasers in Medicine* 3(2), 159-170 (2013)
- [57] H. Stepp, W. Beyer, D. Brucker, A. Ehrhardt, S. Fischer, W. Göbel, M. Goetz, B. Günther, G. Hennig, J. Herms, K.-M. Irion, A. Johansson, Y. Kienast, G. Kniebühler, P. Li, A. Rühm, and S. Sandner, in: *Proc. SPIE, Photonic Therapeutics and Diagnostics VIII* (2012).
- [58] P. A. Valdes, Z. B. Moses, A. Kim, C. J. Belden, B. C. Wilson, K. D. Paulsen, D. W. Roberts, and B. T. Harris, *Journal of neuropathology and experimental neurology* 71(9), 806-813 (2012)
- [59] P. A. Valdes, F. Leblond, A. Kim, B. T. Harris, B. C. Wilson, X. Fan, T. D. Tosteson, A. Hartov, S. Ji, K. Erkmen, N. E. Simmons, K. D. Paulsen, and D. W. Roberts, *J Neurosurg* 115(1), 11-17 (2011)
- [60] N. Bosschaart, G. J. Edelman, M. C. Aalders, T. G. van Leeuwen, and D. J. Faber, *Lasers Med Sci* 29(2), 453-479 (2014)
- [61] Z. J. Chen, G. T. Gillies, W. C. Broaddus, S. S. Prabhu, H. Fillmore, R. M. Mitchell, F. D. Corwin, and P. P. Fatouros, *J Neurosurg* 101(2), 314-322 (2004)
- [62] H. H. Ginary, K. Wong, and K. Lai, Cornell University (2007).

- [63] N. Haj-Hosseini, B. Kistler, and K. Wårdell, in: Proc. SPIE, Design and Performance Validation of Phantoms Used in Conjunction with Optical Measurement of Tissue VI (2014).
- [64] N. Markwardt, M. Götz, N. Haj-Hosseini, B. Hollnburger, R. Sroka, H. Stepp, P. Zelenkov, and A. Rühm, in: Biophotonics: Photonic Solutions for Better Health Care (2016).
- [65] Gelbe Liste Pharmindex (2015), https://www.gelbe-liste.de/produkte/icg-pulsion-5-mg-ml-nach-rekonstitution-pulver-zur-herstellung-einer-injektionsloesung-50mg_496555/fachinformation.
- [66] A. Raabe, J. Beck, R. Gerlach, M. Zimmermann, and V. Seifert, Neurosurgery 52(1), 132-139; discussion 139 (2003)
- [67] K. Roessler, M. Krawagna, A. Dorfler, M. Buchfelder, and O. Ganslandt, Neurosurg Focus 36(2), E7 (2014)
- [68] M. L. Landsman, G. Kwant, G. A. Mook, and W. G. Zijlstra, Journal of applied physiology 40(4), 575-583 (1976)
- [69] A. G. Hofstetter, Lasergestützte Operationsverfahren in der Urologie (Georg Thieme Verlag, Stuttgart, 2003), p. 25f.
- [70] A. Hagen, D. Grosenick, R. Macdonald, H. Rinneberg, S. Burock, P. Warnick, A. Poellinger, and P. M. Schlag, Opt Express 17(19), 17016-17033 (2009)

DANKSAGUNG

Viele Personen haben mich bei dieser Arbeit tatkräftig unterstützt. Besonders möchte ich folgenden Menschen danken:

- **PD Dr. Ronald Sroka** zuallererst für die Möglichkeit, im Laser-Forschungslabor zu promovieren sowie für die Betreuung meiner Arbeit, außerdem für viele hilfreiche Tipps und kritische Anmerkungen, aber auch für das Interesse an meiner persönlichen Entwicklung, für die tolle Stimmung im Labor und das Beibringen einer (zumindest für mich) neuen Ball“sportart“.
- **Dr. Herbert Stepp** für seine sowohl fachlich als auch menschlich hervorragende Betreuung, für zahlreiche unverzichtbare Ideen und Hilfestellungen zu Experimenten und Simulationen, für unermüdliches Korrekturlesen, mehrere Skiwochenenden in Bramberg und eine äußerst kollegiale Zimmernachbarschaft. Herbert, auf dich ist immer Verlass!
- **Dr. Adrian Rühm** für seine stets vorhandene, absolut selbstlose Hilfsbereitschaft, nicht nur bei EDV-Problemen, sondern auch bei diffizilen mathematischen oder theoretisch-physikalischen Fragestellungen, für zahllose Nachtschichten sowie für sein Beharren auf der korrekten Aussprache gewisser französischer und russischer Wörter.
- **Thomas Pongratz** für die immer freundliche Hilfsbereitschaft bei allen technischen, elektronischen und feinmechanischen Problemen, insbesondere was die Fertigung der Seitblickfasern betraf.
- **Kornelia Eberle** für ihre Hilfe bei diversen Bestellungen und sonstigen bürokratischen Ärgernissen.
- den von mir betreuten Studenten **Nikolas Dominik** und **Keerthanan Ulaganathan** für ihre wertvolle Unterstützung bei ihren zahlreichen Arbeiten für das Projekt Gliotax.
- unseren Gliotax-Kollaborationspartnern **Dr. Marcus Götz**, **Dr. Pjotr Zelenkov** und **Pavel Grachev** für die kollegiale und erfolgreiche Zusammenarbeit (und **Prof. Dr. Victor Loshenov** für die freundliche Bewirtung in Moskau!), außerdem **Dr. Neda Haj-Hosseini** für viele hilfreiche Tipps und **Prof. Dr. Gerhard Franz** und seinem Laborteam (besonders **Werner Preisser** und **Armin Hadzimujic**) für die Unterstützung bei der Faserverspiegelung.

Außerdem möchte ich mich ganz herzlich bei allen weiteren Labormitgliedern für ihre Hilfsbereitschaft, die vielen interessanten Gespräche, z.B. beim Mittagessen, und die lockere Arbeitsatmosphäre bedanken: **Prof. Dr. Wolfgang „WoZi“ Zimmermann**, **Dr. Christian Homann**, **Dr. Georg Hennig**, **Max Eisel**, **Alex Lang**, **Patricia Müller**, **Susanne Bour** und vielen kurzfristig anwesenden Studenten und Praktikanten, die hier leider nicht alle genannt werden können.

Ein ganz besonderer Dank gilt meiner Familie, besonders meinen Eltern, die mich in den vergangenen Jahren in so vielen Dingen unterstützt und immer zu mir gestanden haben.

LEBENS LAUF

PERSÖNLICHE DATEN

Name	<u>Niklas</u> Alexander Markwardt
Geburtsdatum	08.05.1989
Geburtsort	München
Staatsangehörigkeit	deutsch

AUSBILDUNG

seit Mär 2014	Doktorarbeit am Laser-Forschungslabor, LIFE-Zentrum, Urologische Klinik und Poliklinik, Klinikum der Universität München
Okt 2011 – Dez 2013	Masterstudium Physik (M. Sc.), Schwerpunkt Biophysik, an der Ludwig-Maximilians-Universität München, Gesamtnote: sehr gut
Okt 2008 – Jul 2011	Bachelorstudium Physik plus Astronomie (B. Sc.) an der Ludwig-Maximilians-Universität München, Gesamtnote: sehr gut
Sep 1999 – Jun 2008	Viscardi-Gymnasium Fürstenfeldbruck Abschluss: Abitur, Gesamtnote: 1,0

PRAKTIKA

Aug 2011 – Okt 2011, Mär 2012 – Apr 2012	Rinecker Proton Therapy Center München, Abteilung Medizinphysik
Feb 2014	Patentanwaltskanzlei Fritzsche Patent München

WISSENSCHAFTLICHE LEHRE

Apr 2015 – Jul 2015	Betreuung der Physik-Bachelorarbeit von Nikolas Dominik, Thema: Untersuchungen zur Detektion von Blutgefäßen mittels ICG-Fluoreszenz, Ludwig-Maximilians-Universität München
Apr 2016 – Aug 2016	Betreuung des Physik-Praxissemesters von Keerthanan Ulaganathan, Thema: Optischer Aufbau zur Tumor- und Blutgefäßdetektion bei der stereotaktischen Biopsie von Hirntumoren, Hochschule für Angewandte Wissenschaften München
seit Okt 2016	Betreuung der Physik-Masterarbeit von Nikolas Dominik, Ludwig-Maximilians-Universität München
seit Okt 2016	Betreuung der Physik-Bachelorarbeit von Keerthanan Ulaganathan, Hochschule für Angewandte Wissenschaften München

EIDESSTATTLICHE VERSICHERUNG

Ich erkläre hiermit an Eides statt,

dass ich die vorliegende Dissertation mit dem Thema

Optische Tumor- und Blutgefäßdetektion zur Erhöhung von Präzision und Sicherheit bei der stereotaktischen Biopsie von Hirntumoren

selbständig verfasst, mich außer der angegebenen keiner weiteren Hilfsmittel bedient und alle Erkenntnisse, die aus dem Schrifttum ganz oder annähernd übernommen sind, als solche kenntlich gemacht und nach ihrer Herkunft unter Bezeichnung der Fundstelle einzeln nachgewiesen habe.

Ich erkläre des Weiteren, dass die hier vorgelegte Dissertation nicht in gleicher oder in ähnlicher Form bei einer anderen Stelle zur Erlangung eines akademischen Grades eingereicht wurde.

München, 13.04.2018

Ort, Datum

Niklas Markwardt

Unterschrift Doktorand